The University of Nottingham

# Continuous hydrothermal synthesis of Inorganic Nanoparticles

Edward Evans MSci

Originally submitted to the University of Nottingham for the degree of Doctor of Philosophy, October 2005

Revised version submitted January 2006

# Declaration

I, Edward Evans, hereby certify that this Thesis has been composed by myself and that it is a record of my own work over the period September 2001 to December 2004.

Where work was carried out in collaboration, the relevant researcher or researchers have been acknowledged.

This Thesis has not been accepted in partial or complete fulfilment of any other degree or professional qualification.

Signed

Edward Evans

# Contents

# Abstract

In Chapter 1, the special properties of nanoparticles are discussed, followed by different methods of nanoparticle synthesis, particularly the hydrothermal flow synthesis. Finally, factors thought to affect particle size are identified, and the aims of the Thesis are stated.

In Chapter 2, hydrothermal flow reactors used by different research groups are discussed. Modelling of the reactor mixing point leads to a new nozzle design, to improve mixing and avoid blockages, which is incorporated into the Nottingham reactor.

In Chapter 3, it is explained how initial problems of reactor blocking are solved, and that formation of CuO is seen to be affected by reaction temperature and which precursor is used.

Chapter 4 details how $RuO_2$ and anatase $TiO_2$ are made separately, and unsuccessful attempts are made to produce rutile $TiO_2$ and a single-phase mixed-metal (Ru-Ti) oxide compound.

Chapter 5 describes how an efficient method of separating $Ce_xZr_{1-x}O_2$ particles from suspension was found. This allowed the identification of a dependence of particle size upon reaction temperature.

In Chapter 6, the effect of increasing temperature upon formation of $\alpha$-$Fe_2O_3$ particles was investigated, and found to give larger particles and greater yields. Particles with different size distributions were then used as catalyst for the growth of carbon nanofibres, leading to the formation of different nanofibre structures.

Chapter 7 reports how successful preliminary experiments were made to form Ag and CdS nanoparticles using the hydrothermal flow method.

Finally, in Chapter 8, the achievements of this Thesis are summarised and ideas are put forward for future work.

# Acknowledgements

I am greatly indebted to many people for their help and support throughout my time working on my PhD and, indeed, before.

Within the School of Chemistry, I would, first and foremost, like to thank my supervisor, Prof. Martyn Poliakoff. Dr. Paul Hamley has given frequent assistance, particularly in respect of the flow reactor and its frequent breakdowns. Dr. Albertina Cabañas was extremely helpful in the early stages of my work. Prof. Mike George and Rakesh Modi advised me in my work with CdS, and Prof. Steve Howdle helped me make corrections after my 2nd-year examination Those working in B11 have also given both aid and encouragement: Dr. Eduardo Garcia-Verdugo, Dr. Lucinda Dudd, Dr. Eleni Venardou, Dr. Adam O'Neil, Wang Jia-Wei and Chong Yan. From SChEME, I would like to thank Dr Paul Blood for a great deal of assistance and collaboration and my second supervisor, Dr. Edward Lester.

From Johnson Matthey, I am grateful for the help of Dr Janet Fisher and Dr Dave Thompsett, my industrial supervisors, and also Dr. Lucy Otley for carrying out electron microscopy studies. Thanks go to the EPSRC for the funding of my PhD, and to Johnson Matthey, for additional funding through a CASE award.

I am most grateful to my friends from the Gilbert and Sullivan society who have kept me amused throughout my time at university, particularly James, Carl, Michael, Claire, Miranda, Kat, Pete, Lesley, Gemma and Sid. A great big չնորհակալություն must also go to Karina for her encouragement throughout my PhD, through thick and thin. Lastly, I would like to thank my parents for their support, both moral and financial, for the duration of my studies.

# Frontispiece

Science fiction has imagined many potential uses for nanosized robots, which science is striving to fulfil. The "nanogenes" from *Doctor Who* (in the episode, "The Doctor Dances" by Steven Moffat) are microscopic robots whose ability to repair people's bodies brings the world to the brink of disaster.

# Chapter 1: Introduction

## *Summary*

This chapter initially discusses the special properties of nanoparticles, including their optical, electronic and chemical properties. Next, several of the alternative methods of nanoparticle synthesis are discussed, such as sol-gel synthesis. We go on to consider hydrothermal synthesis in particular, both in batch form, and using continuous-flow apparatus. The advantages of this latter technique are highlighted, and previous work on flow synthesis, in Nottingham and in other research groups around the world, is detailed. The factors that might affect the particle size of the nanoparticles produced are then discussed and, finally, we identify the aims to be addressed in this Thesis.

## *Nanotechnology*

Nanotechnology has become one of the scientific buzzwords of the early 21st Century. Lord Sainsbury, the UK Science Minister, has often been quoted as saying, "nanotechnology is going to be huge", which exemplifies the excitement many have about the field. This excitement has led to the U.S. National Science Foundation launching a National Nanotechnology Initiative in 2002, with an accompanying website[1], aimed at a general audience, including children. Richard Feynmann put forward the idea of the use of nanotechnology to make miniature robots in his 1959 talk, *There's Plenty of Room at the Bottom* (transcript available on the internet[2]). However, whilst the idea caught many people's imagination, science has a long way to go to catch up with science fiction (see Frontispiece).

Nanotechnology resides somewhere between two established scientific disciplines. One of these is chemistry, which is concerned with the study of atoms and molecules, dimensions of which are typically less than 1 nm. At the other end of the scale is solid-state physics, which deals with solids, consisting of essentially infinite arrays of atoms or molecules, with dimensions greater than 100 nm.

Nanotechnology is intended to fill the gap between these two mature fields. Nanoparticles is a term generally considered to describe particles whose size lies in the range 1-100 nm, which would mean a range of 10-10 000 atoms or molecules per particle[3]. In the nanoscale regime, neither quantum chemistry nor classical laws hold[4]. In certain materials, where there is strong bonding between atoms (metals, semiconductors or insulators), there can be extensive delocalisation of valence electrons. The extent of this delocalisation is highly dependent on particle size which, coupled with structural changes, can lead to different chemical and physical properties. These properties include magnetic, optical, melting points, specific heats and surface reactivity. In addition, when these particles are consolidated into macroscale solids, these bulk materials sometimes themselves show new properties.

Control of the synthesis of these nanoparticles is vital to being able to harness their power, and it is towards this goal that the research in this thesis has been working.

## *Properties of nanoparticles*

Nanoparticles can be expected to possess different properties from those typical of a bulk material. This is due to two main factors: firstly, as particles

get smaller, there is a transition from electronic bands to molecular orbitals; secondly, as particles decrease in size, the percentage of atoms that are at a particle surface, as opposed to within the bulk, becomes greater and greater: often several tens of percent[5].

## Metallic behaviour

The nature of a metal is dependent on the delocalisation of electrons between atoms[6]. It is therefore clear that a single metal atom could not act as a metal. A transition from non-metallic to metallic behaviour occurs as the size of cluster increases from ca. 100 to 10 000 atoms. The gap between adjacent energy levels, $\Delta$, for a particle containing $N$ atoms, will be of the order $E_F/N$ where $E_F$ is the Fermi energy. Whether particles can exhibit metallic behaviour depends upon whether the energy of thermal and incident radiation is of a comparable size to $\Delta$.

## Magnetic behaviour

Magnetic domains are small regions, with sizes of around 22 nm within bulk iron metal, which are spontaneously magnetised to saturation at temperatures below the Curie temperature, but which are oriented in such a way to give the entire sample reduced magnetisation[7].

It was predicted[8] that a particle of ferromagnetic material below a certain size would behave as a single magnetic domain. Such ultrafine materials can show a high magnetic coercivity ($H_c$ - the field strength required to demagnetise a sample), and have thus found applications in information storage. It has been reported[9] that for iron particles with a diameter of 25 nm, a maximum $H_c$ was observed, but for smaller sizes, superparamagnetism sets in[10, 11]. Chemical

synthesis of magnetic nanoparticles is discussed in the review by Willard et al.[12].

## Melting points

As the size of a particle increases, so too does its melting point. This phenomenon has been reported for, amongst other materials, sodium[13] and gold[14] clusters, and also in inert gases and molecular crystals[15-22]. A particularly striking dependence of melting point upon particle size was observed for cadmium sulfide[23].

## Optical and electronic properties

The fact that nanoparticles of any material have unique optical properties has long been known, and was first noted in Faraday's description of colloidal gold solutions that exhibit various colours[24]. A theory of "plasmon resonance" has been developed to explain the visible absorption bands observed for these small metallic particles[25, 26]. In essence, when a metal particle becomes small enough, its atoms begin to develop something akin to molecular orbitals within which absorption of visible light can occur. For larger and larger particles, the absorption band is observed to shift towards longer wavelengths, and eventually gives way to broad bulk-metal absorption. This phenomenon can therefore be used to estimate the size of nanoparticles.

More recent work has dealt with the absorption properties of semiconductor nanoparticles[27], particularly Si, CdS and CdSe. The optical absorption bands of semiconductors will vary with size. In bulk silicon, the gap that needs to be crossed by electrons in the valence band to the empty conduction band is fairly small, since the bands are broad. Incident light can therefore cause electrons to

cross into the conduction band, so bulk silicon is a photoconductor. However, when very small Si particles are considered, sets of molecular orbitals with discrete levels develop, and the gap to be crossed for conduction becomes wider until it reaches a maximum for clusters containing only two Si atoms. A similar effect is observed for other semiconductors.

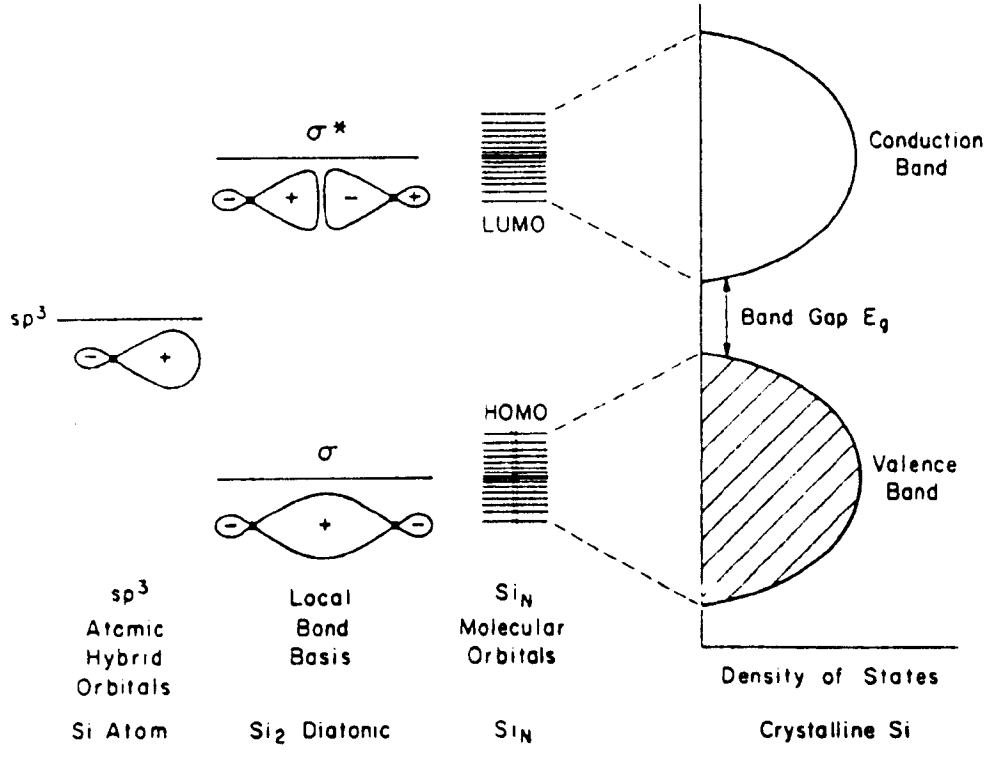


**Figure 1.1: diagram showing molecular orbitals for silicon showing, from left to right, Si atoms, $Si_2$ cluster, larger $Si_N$ clusters and bulk crystalline Si (reproduced from Steigerwald et al.[27])**

Semiconductor nanoparticles, when doped into organic polymers or glass, have also been observed to exhibit non-linear optical properties. The refractive index of such materials changes, depending on the intensity of the incident light[28].

## Chemical properties

If nanoparticles are small enough, the proportion of atoms on the surface of a particle, compared to the total number of atoms, will become significant: the surface atoms on a 3-nm particle, for instance, constitute roughly half of the total number of atoms. In addition to an enormous increase in surface-to-volume ratio, effects are sometimes observed, which are related to different surface chemistry. This may be caused by unusual morphologies, unusual surface defects (perhaps in unusually high concentrations) and unusual electronic states.

The binding energy of silver, as clusters increase in size, becomes greater and greater until it reaches the value for bulk silver. Thus, small silver nanoparticles become very strong reducing agents[29]. Photochemical oxidation of silver clusters is also size dependent[30]. Reactivity changes most sharply at the metal-insulator transition, suggesting that a combination of reducing potential and coordinatively unsaturated metal atom availability (providing molecular orbitals for the complexation of $O_2$) is important.

The optical properties of semiconductor particles are significantly affected by the adsorbed solvent molecules[31]. The large proportion of atoms in a particle residing on the surface mean that peturbation of energy levels or chromophores of the surface atoms can affect the whole particle.

The lifetime of electron-hole pairs in a semiconductor (the time between an electron being promoted from the valence band to the conduction band, and its returning to the valence band) is crucial for their role in photochemically driven redox reactions[32]. For instance, CdS nanoparticles can be used to

photocatalyse the reaction of hydrogen peroxide with organic molecules, whereas large CdS particles cannot[33].

## General areas of nanoparticle application

The high surface area and high surface reactivity of metal oxide nanoparticles could lead to their use as destructive adsorbents to which the substances would be able to chemisorb strongly, often in a dissociative fashion. This could lead to their use in air-purification cartridges, or in the destruction of toxic organic waste, at much lower temperatures than required for incineration[34].

Metal nanoparticles of, for example, iron, zinc or tin, have been shown to be highly reactive with chlorocarbons in water[35]. These might lead to membranes or flow-through channels for treating groundwater contamination.

The field of heterogeneous catalysis is perhaps the most obvious use for nanoparticles. Research on nanoparticle catalysis has effectively been going on for decades, and they are extremely commercially important. One application is their use in catalytic converters for the removal of polluting gases from car exhausts. In particular, cerium-zirconium mixed-oxide nanoparticles have found use as catalytic supports[36-40].

Nanoparticles have also already found their way into the commercially-important field of information storage[41, 42]. Modern audio and video tapes employ the magnetic properties of fine particles. New research is discovering ways to produce ever smaller and more highly magnetic particles, which will allow even greater storage capacity.

The use of magnetic nanoparticles could lead to refrigeration units that do not require refrigeration fluids. This is due to the magnetocaloric effect, which is a

drop in temperature caused by the application of a magnetic field to magnetic particles, and a consequent change in entropy[43].

Solar cells of both the photovoltaic (for producing electricity) and water-splitting (for producing hydrogen) types can employ semiconductor nanoparticles for greater efficiency[44]. They might also be used for the decontamination of water through photo-oxidation or photo-reduction of contaminants[45].

The non-linear optical properties of quantum-confined semiconductor systems may eventually lead to their use in "optical computers"[46].

Nanoparticles can be compressed at fairly mild conditions into solids that are more flexible and malleable than regular ceramics[4]. It is conceivable that it might one day be possible to replace metal as a construction material with ceramics. These materials often have low densities, can be translucent or transparent, and have low thermal conductivities.

Ultrafine particles could prove useful for cosmetics, where lightness, texture and cover are important, and might also be useful for sun screen, as some nanoparticulate substances are able to block ultraviolet rays[47].

## *Alternative synthesis methods*

This section will deal with several of the established methods for the synthesis of nanoparticles.

### Sol-gel methods (aerogels and xerogels)

If aqueous metal ions are precipitated by addition of hydroxide, gels may be formed, and hence ultrafine particles. Water forms concave menisci within the

network of particles at the liquid-vapour interface. As the material is dried, and the water is evaporated, the menisci reduce, and shrinkage occurs, owing to the build-up of surface-tension forces on the walls of the channels and pores. In order to preserve the texture of the wet gel, the vapour interface must be avoided during the drying process. One approach is to replace the water with solvents of higher vapour pressure and lower surface tension, such as alcohols and aromatic compounds. Another is to heat the wet gel under pressure in order to obtain supercritical conditions, and then to vent the supercritical fluid rapidly as a vapour, giving an aerogel (a process known as hypercritical drying)[48-51]. A sol-gel method for producing MgO particles is outlined below[48, 52].

| | | | |
|---|---|---|---|
| 1. | $Mg\ (s) + CH_3OH$ | $\xrightarrow[CH_3OH]{reflux}$ | $Mg(OCH_3)_2 + H_2$ |
| 2. | Addition of toluene to give 20:80 volume mix of methanol:toluene | | |
| 3. | $Mg(OCH_3)_2 + H_2O$ | $\xrightarrow[toluene]{CH_3OH}$ | $Mg(OH)_2 + 2CH_3OH$ |
| 4. | $Mg(OH)_2$ (gel) | $\xrightarrow[CH_3OH,\ toluene,\ \text{hypercritical drying}]{265°C}$ | $Mg(OH)_2$ (ultrafine particles) |
| 5. | $Mg(OH)_2$ | $\xrightarrow{25\text{-}500°C}$ | MgO (nanocrystals) + $H_2O$ |

This approach has been used to prepare nanoparticles of MgO, CaO, $Al_2O_3$, $ZrO_2$, $TiO_2$ and $SiO_2$ amongst others. Supercritical $CO_2$ has also been used instead as the replacement solvent, in place of volatile organic chemicals[49, 50].

## Precipitation and digestion

Traditional precipitation methods can lead to nanoparticles by careful control of conditions, such as pH, or some kind of treatment after precipitation, such as heat treatment in aqueous solution (digestion). Small particles can thus be prepared with broad size range but uniform composition, crystallinity and morphology[53, 54]. For example, $MnFe_2O_4$ nanoparticles (5-180 nm) were prepared from $Fe^{3+}$, $Fe^{2+}$ and $Mn^{2+}$ aqueous solutions. The size was controlled by adjusting the total metal-ion concentration and the hydroxide concentration, whilst the digestion process provided further control. Particle size was found to be at a maximum with a metal:hydroxide ratio of 0.32. This kind of reaction has been reviewed by Matijevic[55].

## Aerosol spray pyrolysis

Droplets of salt solution are formed by nebulisation and are then entrained in a flowing, hot gas (usually nitrogen at 800°C or higher, but oxygen is sometimes used if an oxidising atmosphere is required). As the droplets get hotter and hotter, first evaporation and then chemical reaction occur. Changing the salt concentration and nebulisation procedure allows control of the particle size[3, 56].

## Reactive evaporation

In this process, a metal is evaporated in the presence of a small amount of oxidising gas. Clusters form and are oxidised, and these oxidised clusters collect on a cold finger, or the reactor walls[57].

## Heating of organic and organometallic compounds

Lanthanide, boride and nitride nanoparticles can be obtained by pyrolysis of inorganic or organometallic compounds, as in the following example[58]:

$$(CH_3CN)_xYb(BH_4)_2 \xrightarrow[-CH_3CN,\ -H_2,\ -Yb]{100°C,\ vacuum} YbB_4\ (nanoparticles)$$

Carbide particles have also been formed by first preparing reactive nickel particles by atom clustering in low-temperature alkanes[59]. During this process, some carbon is incorporated into the particles, by reaction with the alkane, forming "active nickel" and "active carbon". On heating to ca. 200°C, the composite particles are converted to Ni and $Ni_3C$ according to the scheme below. Similar results were obtained with palladium.

$$Ni\ (vapour) + pentane \xrightarrow{77\ K,\ 300\ K} Ni_xC_yH_z \xrightarrow{180\ K,\ octane} Ni_3C$$

## *Batch hydrothermal experiments*

This route involves the use of water at high temperature and pressure. In its near-critical region, the ionic product of water is high, and hence hydrolysis might be expected to occur. It is this property of near-critical water that has led to its use as a reagent for the synthesis of inorganic nanoparticles.

The properties of water at different temperatures and pressures have been extensively researched by Franck[60-62]. At temperatures and pressures approaching and beyond the critical point of water, its properties become very different from those at ambient conditions. Whilst near-critical and supercritical water possess many interesting and unusual properties, only the key properties are discussed below.

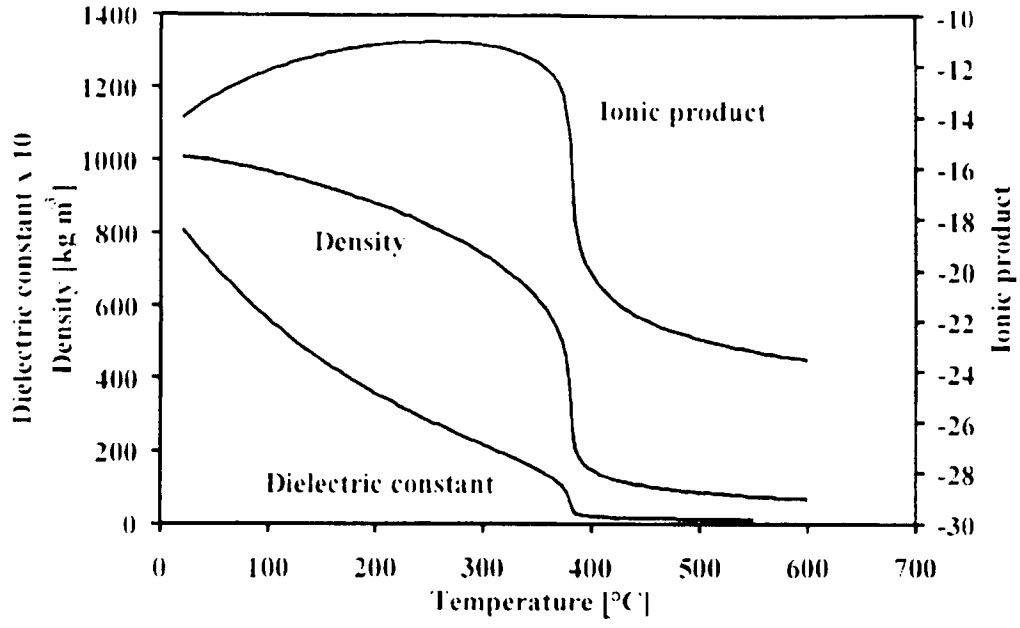


**Figure 1.2: how the ionic product, density and dielectric constant of water change with temperature at a constant pressure of 24 MPa. Figure reproduced from Kritzer et al.[63].**

Figure 1.2 shows that at a given pressure, density and dielectric constant decrease as temperature increases. The ionic product is the product of $H^+$ and $OH^-$ concentrations, and hence it is an indication of the extent to which $H_2O$ molecules have dissociated. This dissociation is an endothermic process, and so, as the temperature increases, the ionic product also increases up to 300°C, where it reaches a maximum. At the critical point (374°C), all three parameters drop to low values (ionic product is bound to decrease sharply, as it depends on concentrations, which themselves depend heavily on density, which is seen to fall dramatically above the critical point). Supercritical water therefore acts as a non-polar solvent with good solvent power for organic compounds, total miscibility with gases, but from which salts will precipitate.

The vast majority of hydrothermal reactions are performed in batch apparatus, which usually consists of a heated autoclave, with reactions taking place under autogenous pressure. This technique has been known for some time, and was reviewed several years ago by Matijevic[64]. Examples include the hydrothermal formation of $TiO_2$ from $TiCl_4$ solution[65, 66], $ZnGa_2O_4$ spinel from $ZnSO_4$ and $Ga(SO_4)_3$ with ammonia[67], $CeO_2$ from various soluble cerium salts[68, 69], $BaFe_2O_4$[70] and copper oxides[71].

## *Continuous hydrothermal flow reactors*

Whilst the use of hydrothermal techniques for the synthesis of ceramic materials dates back to the 19th Century, this had always been by means of batch experiments. However, synthesis in batch has several problems associated with it. A batch hydrothermal synthesis can require the heating of a large volume of water, which must be maintained at a high pressure and temperature for many hours. Also, by the very nature of the process, each batch will yield a finite amount of product.

On a laboratory scale this may not present a problem, as the volume of water may be only a few hundred millilitres and the mass of product required for analysis might be very small. The engineering requirements would not, therefore, be difficult to meet, and repeated runs would not be required to obtain enough material. However, on an industrial scale, the need for large, high-temperature, high-pressure reactors make their construction more difficult and expensive. The amount of energy required to heat the water for long periods also becomes huge on an industrial scale. Additionally, to provide

large amounts of product, the batch process has to be performed many times, which is expensive and time-consuming.

As well as these considerations connected with scaling up the process, the long reaction time of a batch process can encourage particle growth by Ostwald ripening[72], whereby smaller particles redissolve and allow larger particles to grow even larger. This is clearly not conducive to the production of small particles.

As a result of the many shortcomings with the batch synthesis approach, several groups around the world have attempted continuous hydrothermal syntheses of particles. A continuous process has several advantages over a batch process. Firstly, only the small volume of water in the reactor itself needs to be hot at any one time, meaning that engineering the reactor appears to be much simpler (the use of flow reactors brings with it new engineering complexities, involving flow dynamics, which will be discussed in Chapter 2). A small heated volume also leads to the expenditure of less energy in heating the reactor.

A continuous process also has the advantage of being much faster than a batch process: not only is the residence time often only a few seconds but the reactor can be kept running until enough product is made without the need for shutting down and reloading between batches. Lastly, as a consequence of the short residence time, there is the possibility of forming very small particles, without their having time to grow.

The different designs of flow reactor used by various research groups are discussed in Chapter 2. In this introductory chapter, the chemical discoveries made by those groups will be highlighted.

Some of the first hydrothermal flow-reactor syntheses of inorganic nanoparticles were performed by Adschiri, Arai et al. at Tohoku University, Japan. Their initial work[73] involved the reaction of ten different metal salt solutions at a temperature of 400°C and pressure of 35 MPa, with an approximate residence time of 2 min. For all of the precursors except $Al(NO_3)_3$, metal oxides were made, with sizes of ca. 20-200 nm. Reaction of $Al(NO_3)_3$ yielded AlOOH with significantly larger particle size, as shown in Table 1.1.

**Table 1.1: precursors and product composition and particle size from Adschiri et al.'s initial experiments with the hydrothermal flow reactor[74]. Oxide nanoparticles were made in all experiments except for those using $Al(NO_3)_3$, which yield rather larger AlOOH particles.**

| Precursor | Product | Approximate particle size /nm |
|---|---|---|
| $Al(NO_3)_3$ | AlOOH | 600 |
| $Fe(NO_3)_3$ | $\alpha$-$Fe_2O_3$ | 50 |
| $Fe_2(SO_4)_3$ | $\alpha$-$Fe_2O_3$ | 50 |
| $FeCl_2$ | $\alpha$-$Fe_2O_3$ | 50 |
| $Fe(NH_4)_2H(C_6H_5O_7)_2$ | $Fe_3O_4$ | 50 |
| $Co(NO_3)_2$ | $Co_3O_4$ | 100 |
| $Ni(NO_3)_2$ | NiO | 200 |
| $ZrOCl_2$ | $ZrO_2$ (cubic) | 10 |
| $TiSO_4$ | $TiO_2$ | 20 |
| $TiCl_4$ | $TiO_2$ (anatase) | 20 |

Following these experiments, a two-step reaction mechanism for the synthesis of metal oxides from metal salts was proposed, consisting of (1) hydrolysis of the metal ions and (2) dehydration of the metal hydroxide:

Step (1): $M(NO_3)_x + xH_2O \longrightarrow M(OH)_x + xHNO_3$

Step (2): $M(OH)_x \longrightarrow MO_{x/2} + x/2\ H_2O$

Since the dehydration proceeds from the outer surface of the hydrous oxide particles, smaller hydrous oxide particles might be expected to lead to higher dehydration rates. In the sol-gel process, or in a hydrothermal method involving slow heating, dehydration occurs after the growth of relatively large hydroxide particles. However, in the hydrothermal flow synthesis, dehydration can take place before hydrolysis is complete, so a greater reaction rate is expected, and smaller particles are formed.

Adschiri et al. then went on to investigate the effect of temperature and precursor concentration upon morphology of boehmite (AlOOH) crystals, synthesised from $Al(NO_3)_3$[74, 75]. At lower temperatures and low concentration, rhombic plates were obtained, whilst at high temperature or high concentration, hexagonal plates were formed. Just above water's critical temperature, sword-like particles were obtained. When the reactants were mixed at 373 K and then heated to 573 K, particles with a prolate spheroid (rugby ball) shape with laminar plates were formed. These results are summarised in Figure 1.3.

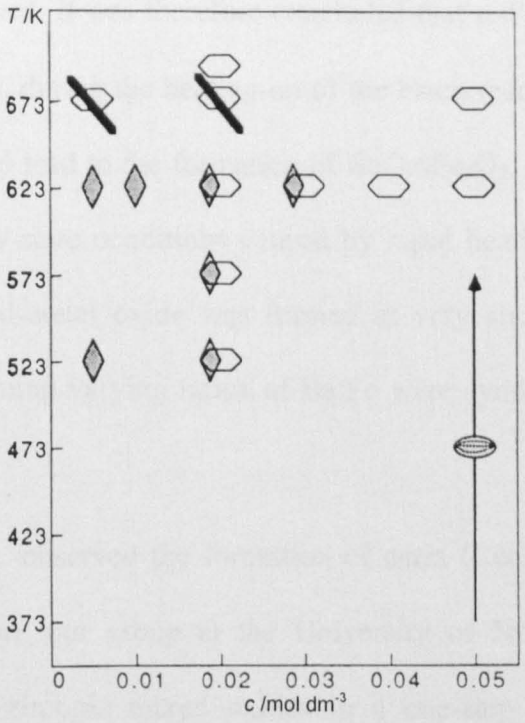


**Figure 1.3: morphologies of boehmite formed with different reaction temperatures and precursor concentrations: ◊ rhombic; ⬭ hexagonal, \ swordlike, 🏉 rugby ball with laminar plates. Figure reproduced from Adschiri et al.[74]**

Formation of ZnO[76-80] nanoparticles has also been reported by the Tohoku University group. Meanwhile, Matson et al. developed a similar method, to which they gave the abbreviation RTDS[81] (Rapid Thermal Decomposition of precursors in Solution). Their published work concentrates on formation of iron oxides in a hydrothermal flow reactor[82, 83].

It was thought that the hydrothermal flow method might be particularly suited to the formation of single-phase, mixed-metal oxides. This led to successful attempts by Hakuta, Adschiri et al. to form $BaO.6Fe_2O_3$ nanoparticles [84]. In batch experiments with short residence times, it had been noticed that $\alpha$-$Fe_2O_3$ (hematite) was formed, whilst in longer experiments, only the mixed-metal

oxides were observed. It was therefore concluded that $\alpha$-$Fe_2O_3$ was formed at lower temperatures, during the heating-up of the batch reactor, and reaction of this hematite would lead to the formation of $BaO.6Fe_2O_3$. In the flow reactor, with its non steady-state conditions caused by rapid heating, hematite is not formed. The mixed-metal oxide was formed at very short residence times. Compounds containing varying ratios of Ba:Fe were synthesised by Rho and Park[85].

After Hakuta et al. observed the formation of ceria ($CeO_2$) nanoparticles[84], Cabañas et al. from our group at the University of Nottingham produced single-phase ceria-zirconia mixed oxides in a one-step hydrothermal flow reactor[39, 40]. Variation of the proportion of cerium to zirconium was observed to lead to mixed oxides with approximately the same Ce:Zr ratio. The samples were homogeneous, with extremely small particle sizes, leading to surface areas of up to 190 $m^2 g^{-1}$.

Several groups went on to make more mixed-metal compounds. Hakuta et al. formed a single-phase material consisting of aluminium yttrium garnet (known as YAG, with formula $Al_5Y_3O_{12}$) doped with terbium[75, 86]. The synthesis was performed in a single step using $Al(NO_3)_3$, $Y(NO_3)_3$ and $TbCl_3$ precursors. Adschiri, Kanamura et al. made single-phase $LiCoO_2$ particles from LiOH and $Co(NO_3)_2$[87, 88].

Galkin et al. synthesised $La_2CuO_4$ nanoparticles using a two-stage process[89]: first, a colloidal suspension of $La(OH)_3$ and CuO was made in the hydrothermal flow reactor; to form the single-phase oxide, this suspension was

dried and annealed at 600°C. The group later produced particles of several other mixed oxides, including zirconium/indium and zirconium/yttrium[90].

Cabañas et al. succeeded in forming the mixed-valence compound $Fe_3O_4$ (magnetite), and the ferrites, $CoFe_2O_4$, $NiFe_2O_4$ and $Ni_xCo_{1-x}Fe_2O_4$ particles[91], whilst Cote and Teja made single-phase $CoFe_2O_4$ compounds[92, 93]. Both groups used Fe(II) compounds as precursors, with partial oxidation of the compounds taking place within the reactor. This oxidation is thought to be due to residual $O_2$ dissolved in the precursor streams, which remains totally miscible with the near-critical and supercritical water in the rig. Some of this dissolved oxygen was removed by bubbling nitrogen through the water before using it as feedstock. If the water is not treated in this way, oxidation of Fe(II) to Fe(III) can occur (as is observed in experiments described in Chapter 6).

## *Factors thought to affect particle size*

The generally recognised mechanism for particle formation was that of LaMer[94, 95]. According to his scheme, particle-forming species are first formed (these might consist of a single metal ion surrounded by as many oxide ions as its valency allows). Once a critical supersaturation of this species is reached, there is a short burst of nucleation. This is then followed by diffusion of constituent complexes on to these primary particles until the supply is exhausted.

However, this mechanism did not account for the high crystallinity of the particles obtained. It now appears that these are obtained by an aggregation mechanism[96], whereby nanoparticles formed by the LaMer scheme aggregate into final larger units.

Lee and Teja[97] provide formulae to describe these processes. The rate of heterogeneous nucleation ($B^0$) is given by Equation 1.1[98].

$$B^0 = A \exp \varphi \left[ - \frac{16 \pi \gamma^3 \nu^2}{3 k^3 T^3 (\ln S)^2} \right]$$

$k$ = Boltzmann constant

$\gamma$ = interfacial tension

$\nu$ = moles of ions formed from one mole of solute

$S$ = degree of supersaturation

$\phi$ = factor related to Gibbs energy of critical nucleus formation

$T$ = temperature

**Equation 1.1**

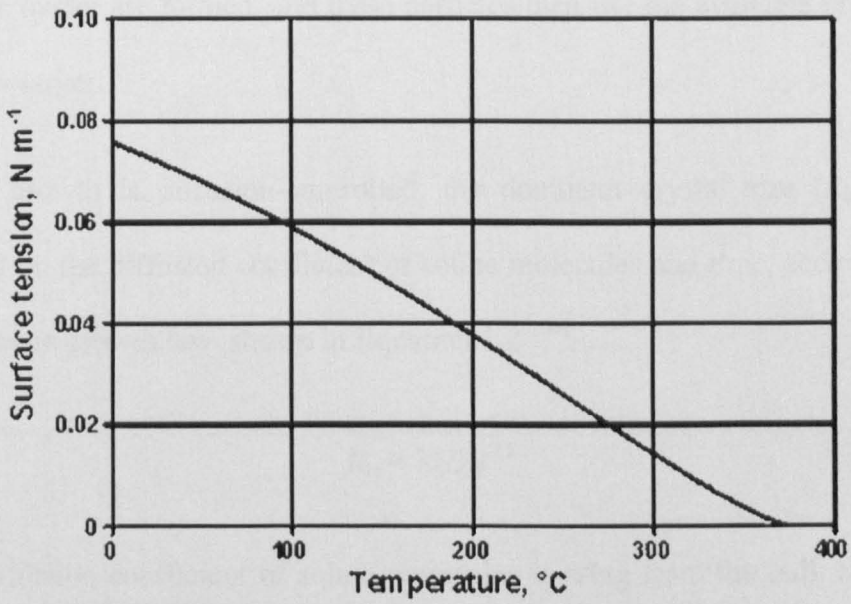


**Figure 1.4: As can be seen from the graph showing the surface tension of water vs. temperature, the surface tension approaches zero as the critical temperature is approached.**

The surface tension of water decreases with temperature and is zero at the critical temperature[99], as can be seen from Figure 1.1. This results in weak interfacial tension between solid particle and water. The solubility of the metal

salt decreases very rapidly with temperature near the critical point, resulting in high supersaturation. Higher nucleation rates are therefore expected at the sub-critical conditions used in this Thesis.

Reactant concentration affects the degree of supersaturation $S$ and the rate of nucleation. When the reactant concentration is low, the degree of supersaturation is likely to be low and the rate of nucleation will also be low. As a result, the ratio of crystal-growth rate to nucleation rate should be larger at low reactant concentrations than at high reactant concentrations. Larger particles should therefore be obtained at lower reactant concentrations, as few particle nuclei are formed, and these particles then use the available precursor to grow larger.

If the growth is diffusion-controlled, the dominant crystal size ($R_m$), will depend on the diffusion coefficient of solute molecules and time, according to a parabolic growth law, shown in Equation 1.2[100].

$$R_m = \lambda(Dt)^{0.5}$$

$D$ = diffusion coefficient of solute molecules moving from the bulk liquid to the crystal surface

$t$ = time

$\lambda$ = a rate constant, that increases with increasing supersaturation

**Equation 1.2**

The diffusivity of the solute becomes greater as temperature increases. Therefore, this equation implies that the particle size will be greater at higher temperatures. This counters the effect seen above, where higher nucleation rate at higher temperatures would be expected to lead to smaller particles. Results

from experiments will help to decide which effect is the stronger. Lee and Teja's results were for the formation of $LiFePO_4$ particles in a batch reactor, at supercritical conditions. These appeared to show that the increase in nucleation rate outweighed the increase in rate of diffusion, as they observed smaller particles at supercritical conditions.

An increase in residence time would be expected to allow larger particles to grow, according the above equation.

Agglomeration of the primary particles is also greatly influenced by temperature via the interfacial tension between the particle and the liquid. Volmer[101] derived Equation 1.3 for the size distribution of particles in a self-dispersing system.

$$n_r = n_0 \exp\left(-\frac{4\pi r^2 \sigma}{kT}\right)$$

The distribution is a Boltzmann distribution. By setting $d^2n_r/dr^2 = 0$, an expression for the approximate maximum particle radius, $r^2_{n\,max}$, found at the inflection point of the graph, is reached:

$$r^2_{n\,max} = \frac{kT}{8\pi\sigma}$$

$r$ = particle radius
$n_r$ = concentration of particles of radius $r$ in the disperse system
$\sigma$ = interfacial tension
$T$ = temperature
$k$ = Boltzmann constant

**Equation 1.3**

$r^2_{n\,max}$ increases with increasing temperature. Interfacial tension ($\sigma$) decreases with temperature, which would serve to further increase $r^2_{n\,max}$. Larger particle

sizes are expected at higher temperatures due to greater agglomeration. Longer residence time might be expected to allow greater time for agglomeration, and therefore larger particles.

In summary, a rise in temperature may lead to an increase or decrease in particle size, depending on the relative effects of nucleation rate, diffusivity and agglomeration. An increase in solute concentration might be expected to decrease the particle size. Pressure is unlikely to have an effect below the critical point of water: the compressibility of water is low below the critical point. At supercritical conditions, changes in pressure would lead to changes in concentration that might affect particle size. However, the experiments in this thesis are performed at sub-critical conditions. An increase in residence time would be expected to lead to larger particles, as there would be more time for primary particle growth, and also for agglomeration to form secondary particles.

Experimental results will be judged against these expectations to investigate whether they still hold for a continuous-flow system.

## Problems to be considered in this Thesis

The work in this thesis follows on from that of Cabañas et al.[39, 40, 91], using the hydrothermal flow reactor that they constructed to form inorganic nanoparticles. Their work achieved the formation of nanoparticles of several different mixed oxides, and showed how, for certain combinations of metals, the proportions of each could be varied over a wide range. However, the important issue of the control of particle size was only briefly investigated.

One of the advantages of flow synthesis is the facile control of temperature, pressure and flow rate, and the effect of these variables will be examined, in relation to the previously-discussed formulae.

In addition, deficiencies in the design of the reactor will be considered. A solution to chronic problems with blockages, encountered particularly by Ilkenhans[102] when making copper oxides, will be sought.

The synthesis of compounds not previously made by the hydrothermal flow method will also be discussed, including new combinations of metals in mixed oxides, and the formation of other chalcogenides and also metal particles.

## References


[1] www.nano.gov.

[2] www.zyvex.com/nanotech/feynman.html.

[3] K. J. Klabunde, C. Mohs, in *Chemistry of Advanced Materials* (Eds.: L. V. Interrante, M. J. Hampden-Smith), Wiley, New York, **1998**, p. 592.

[4] R. P. Andres, R. S. Averback, W. L. Brown, L. E. Brus, W. A. Goddard, A. Kaldor, S. G. Louie, M. Moscovits, P. S. Peercy, S. J. Riley, R. W. Siegel, F. Spaepen, Y. Wang, *J. Mater. Res.* **1989**, *4*, 704.

[5] R. A. Andrievskii, *Rus. Chem. Rev.* **1994**, *63*, 411.

[6] M. R. Harrison, P. P. Edwards, *The Metallic and Nanometallic States of Matter*, Taylor and Francis, London, **1985**.

[7] P. Weiss, *Compt. Rend.* **1906**, *143*, 1136.

[8] J. Frenkel, J. Dorfman, *Nature* **1930**, *126*, 274.

[9] E. E. Carmen, *Powder Met.* **1959**, *4*, 1.

[10] F. E. Luborsky, T. O. Paine, *J. Appl. Phys.* **1960**, *31*, 66.

[11] L. Neel, *C. R. Acad. Sci.* **1949**, *228*, 664.

[12] M. A. Willard, L. K. Kurihara, E. E. Carpenter, S. Calvin, V. G. Harris, *Int. Mater. Rev.* **2004**, *49*, 125.

[13] T. P. Martin, U. Naher, H. Schaber, U. Zimmerman, *J. Chem. Phys.* **1994**, *100*, 2322.

[14] P. Buffat, J. P. Borel, *Phys. Rev.* **1976**, *13*, 2287.

[15] S. J. Peppiat, J. R. Sambles, *Proc. R. Soc. London A* **1975**, *345*, 387.

[16] M. Y. Hahn, R. L. Whetten, *Phys. Rev. Lett.* **1988**, *61*, 1190.

[17] C. Solliard, *Surf. Sci.* **1981**, *106*, 58.

[18] C. L. Briant, J. J. Burton, *J. Chem. Phys.* **1975**, *63*, 2045.

[19] W. D. Kristensen, E. J. Jensen, R. M. J. Cotterill, *J. Chem. Phys.* **1974**, *60*, 4161.

[20] J. D. Honeycutt, H. C. Anderson, *J. Phys. Chem.* **1987**, *91*, 4950.

[21] J. Waltersdorf, A. S. Nepijko, E. Pippel, *Surf. Sci.* **1981**, *106*, 64.

[22] C. Solliard, M. Flueli, *Surf. Sci.* **1985**, *156*, 487.

[23] A. N. Goldstein, C. M. Echer, A. P. Alivisatos, *Science* **1992**, *256*, 1425.

[24] M. Faraday, *Philos. Trans. R. Soc. London Ser.* **1857**, *147*, 145.

[25] C. Mie, *Ann. Phys.* **1908**, *25*, 377.

[26] T. L. Ferrell, *Am. Sci.* **1985**, *73*, 344.

[27] M. L. Steigerwald, L. E. Brus, *Acc. Chem. Res.* **1990**, *23*, 183.

[28] Y. Wang, *Acc. Chem. Res.* **1991**, *24*, 133.

[29] A. Henglein, *Ber. Bunsenges. Phys Chem.* **1990**, *94*, 600.

[30] T. Linnert, P. Mulvaney, A. Henglein, *Ber. Bunsenges. Phys Chem.* **1991**, *95*, 838.

[31] Y. Wang, N. Herron, *J. Phys. Chem.* **1987**, *91*, 5005.

[32] A. Henglein, *Top. Curr. Chem.* **1988**, *143*, 115.

[33] A. J. Hoffmann, E. R. Carraway, M. R. Hoffmann, *Environ. Sci. Technol.* **1994**, *28*, 776.

[34] Y. X. Li, K. J. Klabunde, *Langmuir* **1991**, *7*, 1388.

[35] T. Boronia, K. J. Klabunde, G. B. Sergeev, *Environ. Sci. Technol.* **1995**, *29*, 1511.

[36] J. Kaspar, P. Fornasiero, M. Graziani, *Catal. Today* **1999**, *50*, 285.

[37] A. Trovarelli, *Catal. Rev.-Sci. Eng.* **1996**, *38*, 439.
[38] R. M. Heck, R. J. Farrauto, *Catalytic Air Pollution Control - Commercial Technology*, John Wiley & Sons Inc, **1994**.
[39] A. Cabanas, J. A. Darr, E. Lester, M. Poliakoff, *Chem. Commun.* **2000**, 901.
[40] A. Cabanas, J. A. Darr, E. Lester, M. Poliakoff, *J. Mater. Chem.* **2001**, *11*, 561.
[41] E. Matijevic, *Annu. Rev. Mater, Sci.* **1985**, *15*, 483.
[42] E. Matijevic, *MRS Bull.* **Dec 1989**, 18.
[43] R. D. McMichael, R. D. Shull, L. J. Swartzendruber, L. H. Bennet, *J. Magn. Mater.* **1992**, *111*, 29.
[44] N. A. Anderson, T. Q. Lian, *Annu. Rev. Phys. Chem.* **2005**, *56*, 491.
[45] S. O. Obare, G. J. Meyer, *J. Environ. Sci. Health Part A-Toxic/Hazard. Subst. Environ. Eng.* **2004**, *39*, 2549.
[46] N. Herron, *Chem. Technol.* **1989**, 542.
[47] J. W. Choi, J. Y. Kim, W. Lee, W. H. Lee, H. D. Jang, S. B. Lee, *J. Ind. Eng. Chem.* **2004**, *10*, 428.
[48] S. Utamapanya, K. J. Klabunde, J. R. Schlup, *Chem. Mat.* **1991**, *3*, 175.
[49] H. D. Gesser, P. C. Goswami, *Chem. Rev.* **1989**, *89*, 765.
[50] S. J. Teichner, G. A. Nicolaon, M. A. Vicarini, G. E. E. Gardes, *Adv. Colloid Interface Sci.* **1976**, *5*, 245.
[51] S. S. Kistler, *J. Phys. Chem.* **1932**, *36*, 52.
[52] H. Itoh, S. Utamapanya, J. V. Stark, K. J. Klabunde, J. R. Schlup, *Chem. Mat.* **1993**, *5*, 71.
[53] Z. X. Tang, C. M. Sorensen, K. J. Klabunde, G. C. Hadjipanayis, *J. Colloid Interface Sci.* **1991**, *146*, 38.
[54] T. Sugimoto, E. Matijevic, *J. Colloid Interface Sci.* **1980**, *74*, 227.
[55] E. Matijevic, *Acc. Chem. Res.* **1981**, *14*, 22.
[56] Z. X. Tang, S. Nafis, C. M. Sorensen, G. C. Hadjipanayis, K. J. Klabunde, *IEEE Trans. Magn.* **1989**, *25*, 4236.
[57] G. Lassaletta, A. Fernandez, J. P. Espinos, A. R. Gonzalezelipe, *J. Phys. Chem.* **1995**, *99*, 1484.
[58] J. P. White, H. B. Deng, S. G. Shore, *Inorg. Chem.* **1991**, *30*, 2337.
[59] P. Hooker, J. T. Beng, K. J. Klabunde, S. Suib, *Chem. Mat.* **1991**, *3*, 947.
[60] E. U. Franck, *J. Chem. Thermodyn.* **1987**, *19*, 225.
[61] E. U. Franck, *Ber. Bunsen-Ges. Phys. Chem. Chem. Phys.* **1984**, *88*, 820.
[62] E. U. Franck, *Angew. Chem.-Int. Edit.* **1961**, *73*, 309.
[63] P. Kritzer, N. Boukis, E. Dinjus, *J. Supercrit. Fluids* **1999**, *15*, 205.
[64] E. Matijevic, *Chem. Mat.* **1993**, *5*, 412.
[65] Y. Q. Zheng, E. R. Shi, Z. Z. Chen, W. J. Li, X. F. Hu, *J. Mater. Chem.* **2001**, *11*, 1547.
[66] H. B. Yin, Y. Wada, T. Kitamura, T. Sumida, Y. Hasegawa, S. Yanagida, *J. Mater. Chem.* **2002**, *12*, 378.
[67] M. Hirano, *J. Mater. Chem.* **2000**, *10*, 469.
[68] M. Hirano, E. Kato, *J. Mater. Sci. Lett.* **1996**, *15*, 1249.
[69] M. Hirano, E. Kato, *J. Am. Ceram. Soc.* **1996**, *79*, 777.
[70] E. Matijevic, *J. Colloid Interface Sci.* **1987**, *117*, 593.
[71] P. McFayden, E. Matijevic, *J. Coll. Interfac. Sci.* **1973**, *44*, 95.

[72] R. Boistelle, J. P. Astier, *J. Cryst. Growth* **1988**, *90*, 14.
[73] T. Adschiri, K. Kanazawa, K. Arai, *J. Am. Ceram. Soc.* **1992**, *75*, 1019.
[74] T. Adschiri, K. Kanazawa, K. Arai, *J. Am. Ceram. Soc.* **1992**, *75*, 2615.
[75] Y. Hakuta, T. Adschiri, H. Hirakoso, K. Arai, *Fluid Phase Equilib.* **1999**, *160*, 733.
[76] S. Ohara, T. Mousavand, M. Umetsu, S. Takami, T. Adschiri, Y. Kuroki, M. Takata, *Solid State Ion.* **2004**, *172*, 261.
[77] K. Sue, K. Kimura, K. Murata, K. Arai, *J. Supercrit. Fluids* **2004**, *30*, 325.
[78] K. Sue, K. Murata, K. Kimura, K. Arai, *Green Chem.* **2003**, *5*, 659.
[79] K. W. Sue, K. Kimura, M. Yamamoto, K. Arai, *Mater. Lett.* **2004**, *58*, 3350.
[80] K. Sue, K. Kimura, K. Arai, *Mater. Lett.* **2004**, *58*, 3229.
[81] D. W. Matson, J. C. Linehan, J. G. Darab, M. F. Buehler, M. R. Phelps, G. G. Neuenschwander, *Abstr. Pap. Am. Chem. Soc.* **1995**, *209*, 63.
[82] D. W. Matson, J. C. Linehan, R. M. Bean, *Mater. Lett.* **1992**, *14*, 222.
[83] D. W. Matson, J. C. Linehan, J. G. Darab, M. F. Buehler, *Energy Fuels* **1994**, *8*, 10.
[84] Y. Hakuta, T. Adschiri, T. Suzuki, T. Chida, K. Seino, K. Arai, *J. Am. Ceram. Soc.* **1998**, *81*, 2461.
[85] S. Rho, S. Park, *Korean J. Chem. Eng.* **2002**, *19*, 120.
[86] Y. Hakuta, T. Haganuma, K. Sue, T. Adschiri, K. Arai, *Mater. Res. Bull.* **2003**, *38*, 1257.
[87] K. Kanamura, T. Umegaki, K. Toyoshima, K. I. Okada, Y. Hakuta, T. Adschiri, K. Arai, in *Electroceramics in Japan III, Vol. 181-1*, **2000**, pp. 147.
[88] T. Adschiri, Y. Hakuta, K. Kanamura, K. Arai, *High Pressure Res.* **2001**, *20*, 373.
[89] A. A. Galkin, B. G. Kostyuk, V. V. Lunin, M. Poliakoff, *Angew. Chem.-Int. Edit.* **2000**, *39*, 2738.
[90] A. A. Galkin, B. G. Kostyuk, N. N. Kuznetsova, A. O. Turakulova, V. V. Lunin, M. Polyakov, *Kinet. Catal.* **2001**, *42*, 154.
[91] A. Cabanas, M. Poliakoff, *J. Mater. Chem.* **2001**, *11*, 1408.
[92] L. J. Cote, A. S. Teja, A. P. Wilkinson, Z. J. Zhang, *J. Mater. Res.* **2002**, *17*, 2410.
[93] L. J. Cote, A. S. Teja, A. P. Wilkinson, Z. J. Zhang, *Fluid Phase Equilib.* **2003**, *210*, 307.
[94] V. K. LaMer, *Ind. Eng. Chem.* **1952**, *44*, 1270.
[95] V. K. LaMer, R. H. Dinegar, *J. Am. Chem. Soc.* **1950**, *72*, 4847.
[96] W. P. Hsu, L. Rönnquist, E. Matijevic, M. C. Chon, *Langmuir* **1988**, *4*, 38.
[97] J. Lee, A. D. Teja, *J. Supercrit. Fluids* **2005**, *35*, 83.
[98] O. Söhnel, J. W. Mullin, *J. Cryst. Growth* **1978**, *44*, 377.
[99] D. C. Agrawal, V. J. Menon, *Phys. Rev.* **1992**, *A46*, 2166.
[100] R. W. Cahn, P. Haasen, E. J. Cremer, in *Materials Science Technology, Vol. 5*, WCH Press, Weiheim, **1991**.
[101] Y. G. Frolov, *Colloid J. USSR* **1987**, *49*, 72.
[102] T. Ilkenhans, J. A. Darr, P. A. Hamley, M. Poliakoff, *Unpublished Work* **2001**.

# Chapter 2: the flow reactor

## *Summary*

The hydrothermal flow reactor, as inherited from my predecessors (Rig 1), suffered from several problems. Firstly, it was not possible to reach supercritical temperatures using the preheater. More importantly, total blockages of the reactor were very common, which made experiments very difficult to perform. The problem was thought to lie with the design of the portion of the reactor where the hot and cold liquid streams met. In this initial rig design, this portion consisted of a simple T-piece, but this design allowed precursor to react upstream of the mixing point, in the metal-salt inlet.

Dr. Paul Blood and co-workers, chemical engineers from the University of Nottingham, modelled the T-piece using a Perspex pseudo-reactor and dyed liquids of different densities[1]. It was discovered that buoyancy forces were very important in determining how the streams would mix, and that therefore orientation of the T-piece could be significant. However, it appeared that no orientation of the simple T-piece led to ideal mixing conditions so other designs were considered.

Almost all of the alternative designs for hydrothermal flow reactors used in different research groups used a simple T-piece, so an entirely novel reactor was designed and modelled by Blood et al.[2, 3], which consisted of two concentric tubes. The central tube acted as a nozzle for the hot water, and the outer tube carried cold metal-salt solution in the opposite direction. This design led to very good mixing and no contamination by hot water in the metal-salt inlet, upstream of the nozzle.

A new rig (Rig 2) was designed and built incorporating the new mixing-point design and also a new heater and cooling system. Blockages then very seldom occurred, and a higher reaction temperature was attainable, preventing further unnecessary delays to experiments.

## The initial rig design and minor improvements

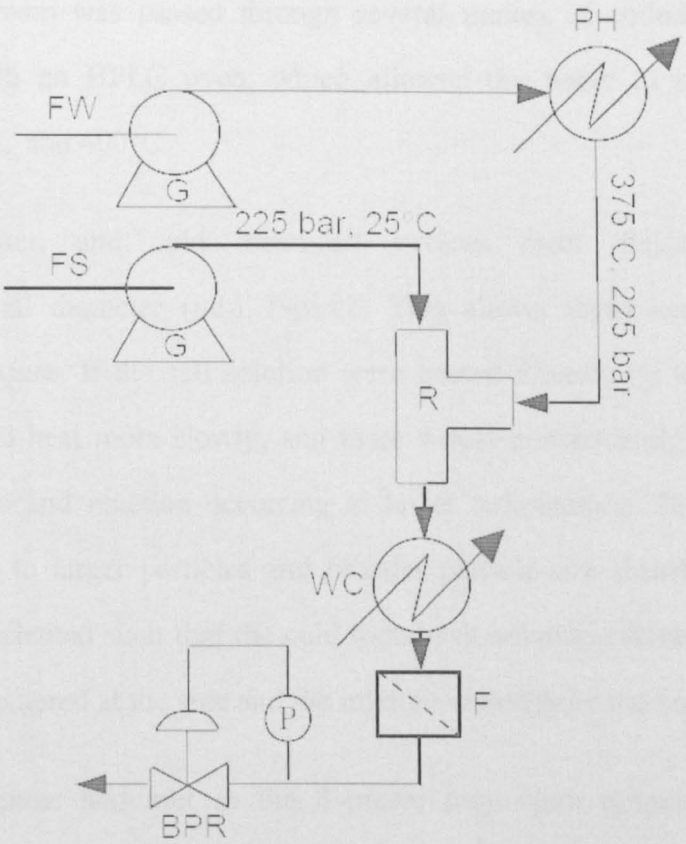


**Figure 2.1: Design of Rig 1. The water feed (FW) and metal-salt feed (FS) are pumped into the reactor using Gilson pumps (G). Water is heated in the preheater (PH, an HPLC oven) and the flows meet in the reactor (R) which is a simple T-piece. The reaction mixture is then quickly cooled with a water jacket (WC), filtered in a Nupro filter (F), and then emerges through the back-pressure regulator (BPR), which maintains the pressure.**

The apparatus with which the initial experiments were performed (Rig 1) was not significantly changed from that used in Nottingham by Cabañas and Galkin et al.[4-8] and is shown in Figure 2.1. The high-pressure system was constructed from Swagelok components.

Two Gilson pumps were used: one pump worked at up to 5 ml $min^{-1}$, and was used to pump metal salt solutions; the other worked at up to 25 ml $min^{-1}$, and

pumped deionised water and, when required, dilute hydrogen peroxide or base. The water stream was passed through several metres of coiled tubing that passed through an HPLC oven, which allowed the water to be heated to between 300°C and 400°C.

The hot water, and cold metal-salt streams meet inside a simple 3/8-inch internal diameter (i.d.) T-piece. This allows rapid heating of the metal-salt mixture. If the salt solution were heated directly by the oven, the solution would heat more slowly, and there would consequently be a longer residence time and reaction occurring at lower temperature. This would be likely to lead to larger particles and broader particle-size distributions. The T-piece was oriented such that the cold metal-salt solution entered at the top, the hot water entered at the side and the mixture exited from the bottom.

Once the streams had met in the T-piece, they were quickly cooled to ca. 100°C using a heat exchanger, consisting of coiled tubing, carrying running cold water, wound around the reactor pipe, and finally cooled to room temperature inside a large cooling coil, once more carrying running cold water.

A pressure of up to 250 bar within the rig is maintained by a Tescom manually-operated back-pressure regulator (BPR). The BPR can be adversely affected by large particle aggregates passing through it, as it is not designed to carry streams containing particles. The stream is therefore passed through a Nu-Pro filter, with pore diameter of 0.5 μm, before the BPR. Even despite this filter, smaller particles, particularly those harder than the stainless steel from which the BPR is made, can lead to scratching inside the BPR, and subsequent loss of ability to hold pressure. The particles are collected in a beaker as a suspension that emerges from the BPR.

The pressure of the rig is monitored on a digital display, programmed to stop the pumps if the pressure exceeds 320 bar. This might happen in the event of blockages of the rig, and stopping the pumps will prevent the pressure from rising any further, and may allow the pressure to decrease slowly, depending on whether the blockage is partial or total. The temperature of the rig outflow, which should be room temperature, is also monitored and the pumps are stopped if it goes beyond 50°C – this usually happens in the event of the cooling water failing.

Using the HPLC oven alone for heating proved to be inadequate to reach the required temperatures – the hot water, before mixing with the cold metal-salt solution, was only reaching 300°C. After replacing the aging oven with a similar newer one, it was decided to add a small tube furnace just upstream of the mixing point. This would allow the water to be heated further, and also provide more responsive, and more accurate, control of heating: the heater would be controlled by a thermocouple within the T-piece, which would be set by the user. This development was an improvement, but did not completely overcome the problem of not reaching particularly high temperatures. A more effective solution was built into the new rig design (Rig 2) discussed later.

It was observed, particularly when producing copper oxide, that blockages were occurring in the metal-salt inlet of the T-piece (see Figure 2.2). This was assumed to be a consequence of the region upstream of the T-piece becoming hot, and allowing reaction to occur and, because of the low metal-salt flow rate through that region, leading to accumulation of particles. Each time, removal of the blockage involved partially dismantling the rig, drilling out the particles, and then cleaning the T-piece ultrasonically.

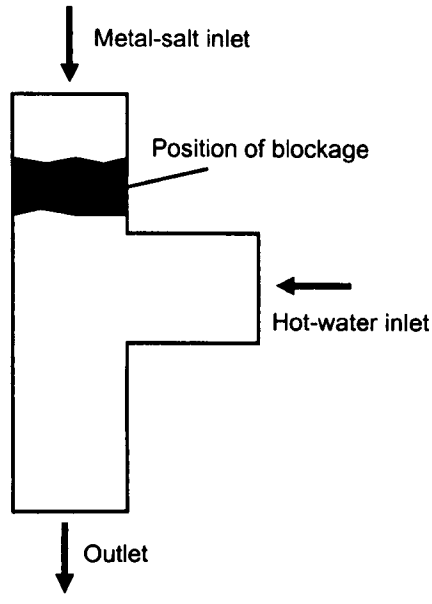


**Figure 2.2: Blockages often occurred within the metal-salt inlet of the T-piece in Rig 1, just upstream of the nominal mixing point, as shown in the diagram.**

Therefore, during this work on copper oxide, an extra cooling coil, identical to the one immediately downstream of the T-piece, was fitted upstream, just before the metal-salt inlet of the T-piece. However, this did not lead to a significant decrease in frequency of blockages and eventually led to a complete redesign of Rig 1 (see below).

## Modelling the new mixing piece

### Technique

It was decided by Blood, Denyer et al., chemical engineers from the University of Nottingham, that knowledge of how the hot and cold fluids mixed within the reactor could shed light upon the causes of the frequent blockages in the reactor. This did eventually lead not only to an explanation[1], but also to an alternative design to solve the problem[3].

Adschiri et al.[9] attempted the modelling of their hydrothermal flow reactor using computational fluid dynamics (CFD). However, the use of this technique is notoriously problematic for supercritical and near-critical systems, so the Nottingham group decided to use a physical model to simulate the mixing. The modelling would lead to the identification of the best orientation for the T-piece, and would also allow the testing of different mixing-piece designs.

Each mixing piece was modelled in a large bock of clear Perspex, with an internal diameter of 3.8 cm. It would clearly be highly impractical to use fluids at similar temperatures and pressures to those in the real reactor within this model, so fluids were carefully selected so that, at ambient conditions, they would reflect the ratio of the Reynolds Numbers of the hot and cold streams (the Reynolds Number, Re, is the ratio of viscous to inertial forces in a fluid).

Methanol was chosen to represent the hot-water stream, whereas the much denser 40% w/w aqueous sucrose solution was used to represent the metal-salt solution. Methylene blue dye was used to colour the sucrose solution. These solutions were fed into the Perspex T-piece, which was lit from behind and filmed with a digital video camera from the front. Observation of how the dyed and non-dyed fluids mixed showed the path taken by the pseudo metal salt, and highlighted the zones of strong mixing and turbulence within the reactor. This modelling technique could not, however, take into account any heating effects or phase changes that might occur – for example, as the hot water cools, on contact with the cold, it would become much denser.

The digital images of the pseudo-reactor were compared by computer with calibration images of the same pseudo-reactor containing known concentrations of dye. This allowed the elimination of errors due to differing light intensity over the image, and also due to the different chord length across

the reactor (whose tubes had a circular cross section). The analysis technique is described in more detail in the published report[1].

## Findings

### *Geometry A: as already used in Rig 1*

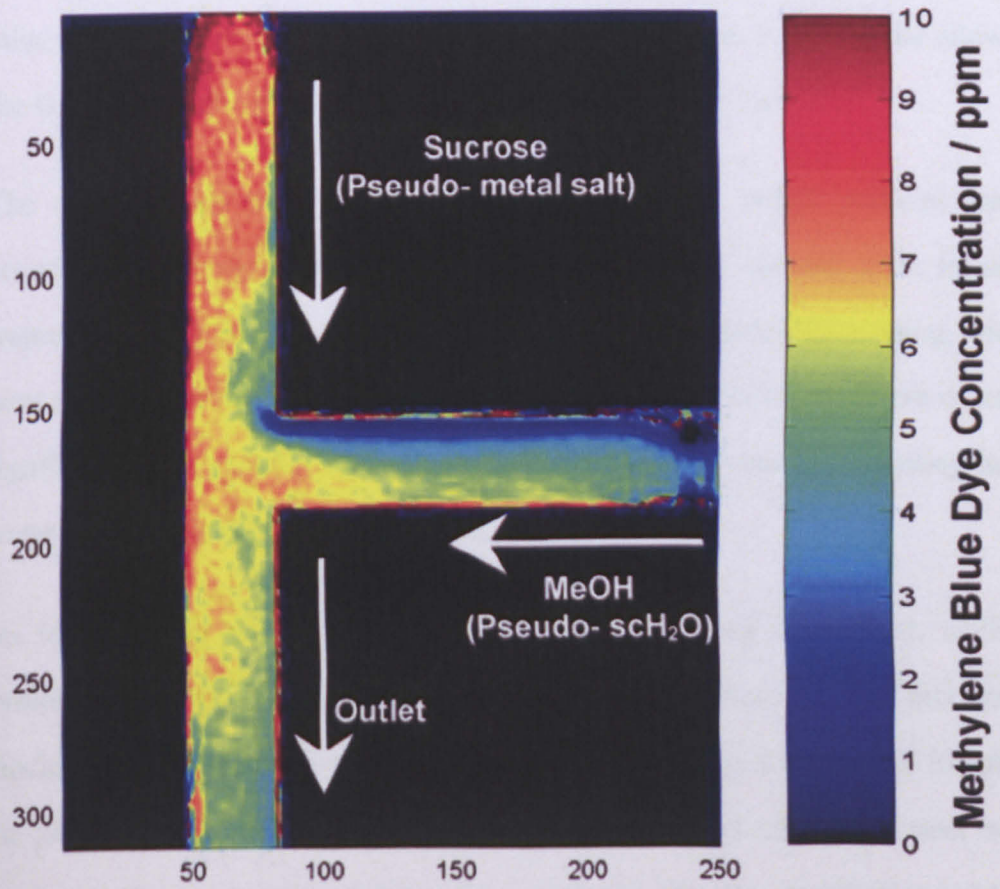


**Figure 2.3: the steady-state concentration map for the T-piece pseudo-reactor with geometry A shows that fast mixing is occurring, which is desirable, but that it is occurring within the reactor inlet, which is undesirable. The partitioning of the two liquids can also be observed within the side-bar. These effects are due to the lower density of the pseudo-scH$_2$O stream compared to the pseudo-metal-salt. For this experiment, the sucrose solution (representing the metal-salt solution) was dyed blue.**

The first geometry to be tested was that already used in Rig 1; metal-salt solution being pumped in from the top-arm of the T-piece, and hot water from the side-arm. The steady-state concentration map is presented in Figure 2.3.

When the less-dense blue methanol and denser sucrose streams meet, buoyancy effects caused the formation of macromixing eddies within the top inlet arm of the reactor. This macro-mixing phenomenon may be what allows the fast nucleation mechanism that leads to nano-particle formation.

The concentration maps can also be used to identify where particles may accumulate and cause blockages. The mixing in the sucrose inlet stream (representing the metal-salt solution) leads to stagnant zones developing, with poor net flow, to which are attributed the formation of blockages. There is also significant flow partitioning within the methanol inlet arm (representing hot water), where the two fluids are not mixing.

An ideal mixing geometry would allow uniform mixing throughout, whilst avoiding inlet mixing, stagnant zones and flow partitioning. The fact that blockages were observed in the real reactor in the metal salt inlet, in exactly the place in the pseudo-reactor where the region of good mixing but poor net flow was observed, suggested that the pseudo-reactor was an effective model for the real reactor.

### *Geometry B: water and metal-salt streams interchanged*

The second example used the same model T-piece, in the same orientation, whilst pumping the methanol (representing $scH_2O$) into the top arm of the T-piece, whilst the dyed sucrose solution (representing the metal-salt solution) was pumped into the side-arm of the T-piece. The steady-state concentration map is shown in Figure 2.4.

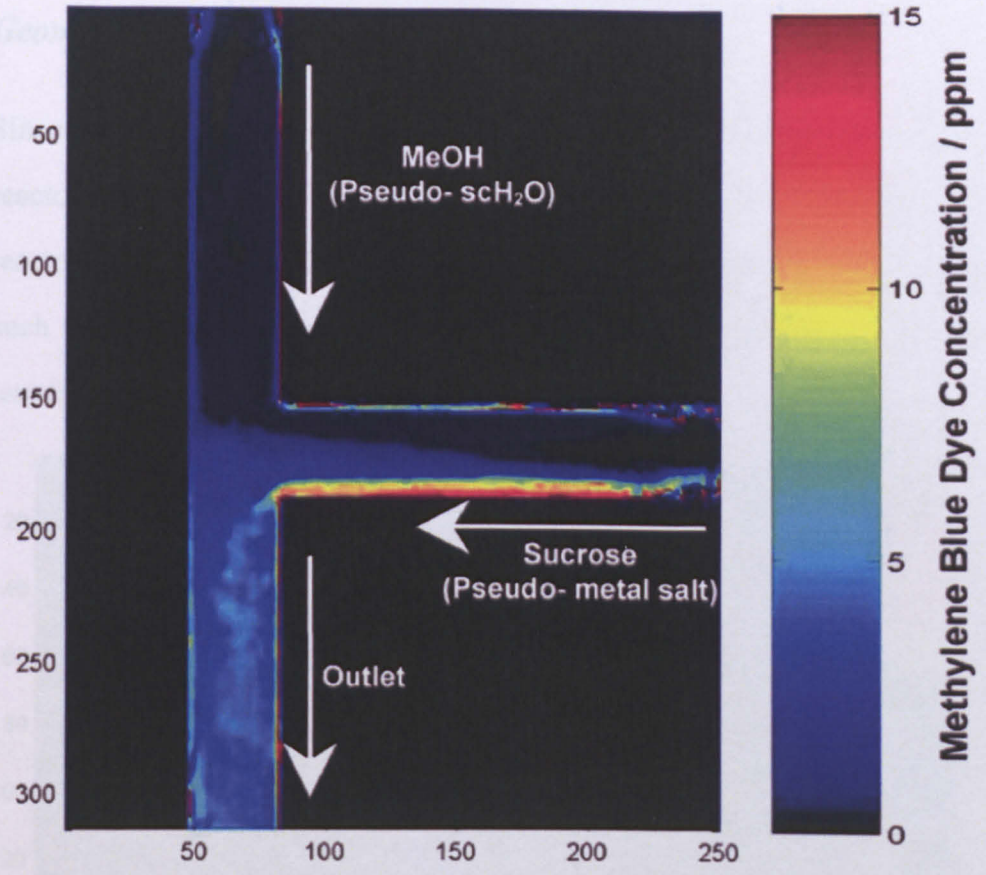


**Figure 2.4: the steady-state concentration map for the T-piece pseudo-reactor with geometry B shows how buoyancy forces are, once more, important. Fluid partitioning occurs within the side-bar, whilst some mixing is occurring within the reactor outlet.**

Comparison of Figure 2.3 and Figure 2.4 reveals that the mixing occurs in a very different way in the two geometries. In Geometry B, the fluid representing the metal salt flows along the bottom of the side arm, which results in the formation of obvious fluid partitioning. On reaching the junction in the T-piece, the sucrose solution cascades downwards, as it is denser relative to the fluid representing hot water. Mixing is therefore observed only in the outlet arm, which leaves the top-arm uncontaminated – both desirable in a reactor design. Conversely, the partitioning in the side-arm will lead to particle accumulation in that region.

### *Geometry C: Rotation of the T-piece*

Since buoyancy forces play such a major role in the fluid dynamics within the reactor, it was deemed interesting to investigate different orientations of the reactor. The steady-state concentration map for the T-shaped reactor, oriented such that the two inlet streams come from either side, and the outlet stream leaves downwards, is shown in Figure 2.5.

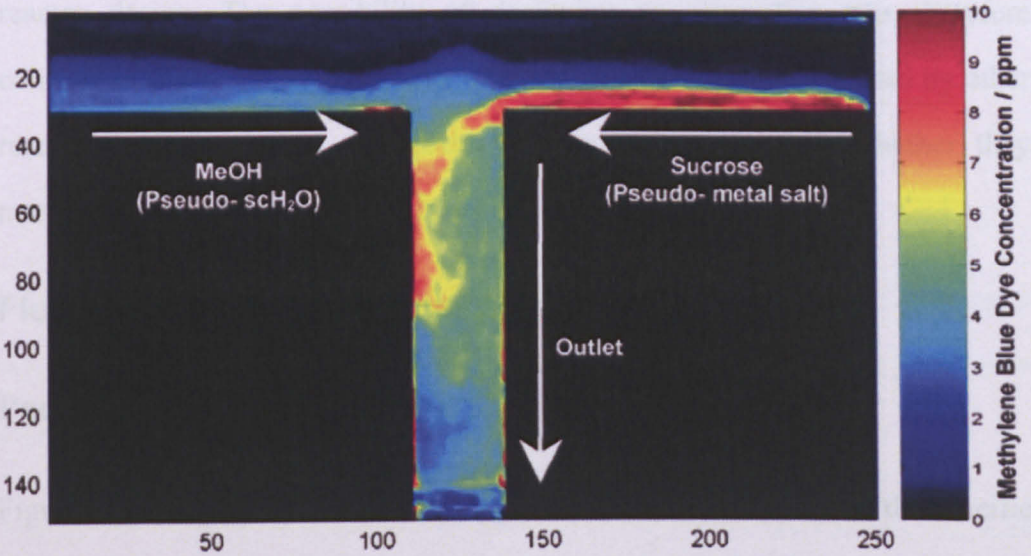


**Figure 2.5: the steady-state concentration map for the T-piece pseudo-reactor with geometry C shows how stream partitioning, which was observed in geometries A and B is observed here across the entire width of the reactor. Mixing is occurring in the outlet pipe, but more slowly than in geometry A.**

The stream partitioning can be seen to occur across the whole width of the reactor, and the orientation can therefore be seen to be rather poor (a conclusion similar to that reached by Adschiri et al. about the same geometry using a CFD/kinetic model[9]).

### *Conclusions of the study of geometries A, B and C*

Of the three geometries tested, geometry A, as used in Rig 1, was found to be the best, as it allowed the best mixing. However, it also suffered from contamination of the inlet stream (with consequent likelihood of particle formation "upstream" of the mixing point) and flow partitioning. It became clear that the T-piece, whichever orientation is used, is far from being an ideal reactor design. The possibility of designing an alternative was therefore considered. As a first step, the hydrothermal flow reactors being used by other research groups around the world were considered, to see whether they managed to overcome the problems suffered by our group.

## Flow reactors used by other groups

## Pacific Northwest Laboratory

Figure 2.6 shows the reactor used by Matson et al.[10, 11] at the Pacific Northwest Laboratory, USA, which differed in two principal ways from the Nottingham design. Firstly, there was no meeting of separate hot-water and metal-salt streams in the reactor: a dilute metal-salt stream was heated to the reaction temperature in a single tube. Secondly, the BPR was connected not to the reactor outlet, but rather along the inlet pipe and, in the event of an over pressure, would vent precursor solution back into the feedstock container. The product was depressurised and cooled by passing it through a tiny pressure nozzle into a water-cooled chamber.

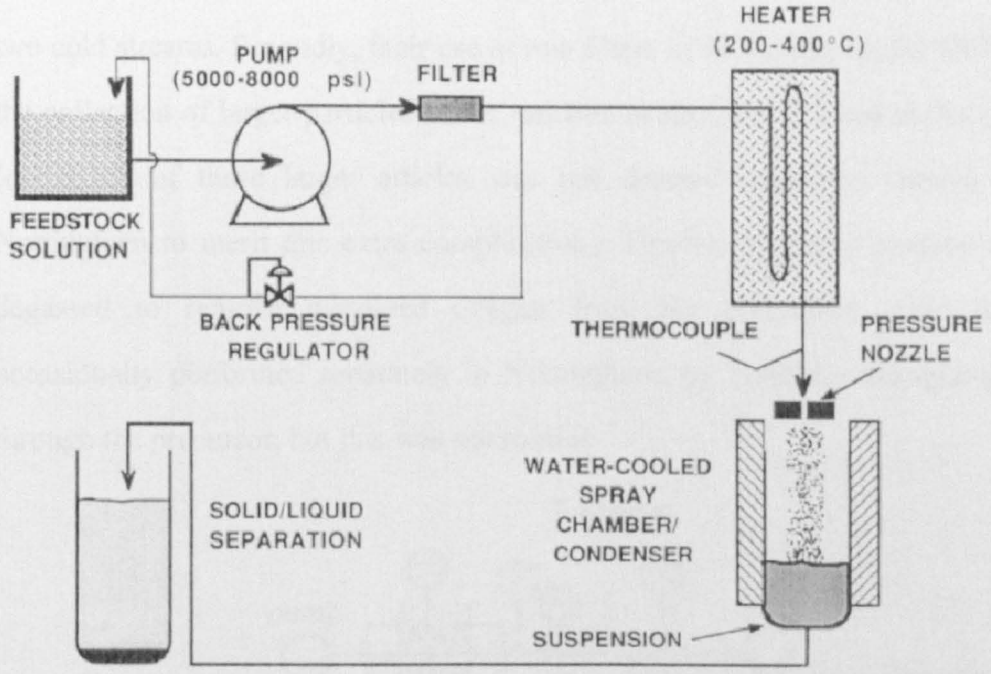


**Figure 2.6: the Pacific Northwest Laboratory reactor design, involving a single dilute metal-salt stream flowing through an oven, and depressurisation through a nozzle (reproduced from Matson et al.[10])**

Whilst this arrangement seems simple, it is not entirely satisfactory because there is no rapid heating of the reaction mixture and therefore reaction might occur over a long period and at different temperatures, which might lead to larger particles, and a broader distribution of sizes.

## Tohoku University

Adschiri, Arai and co-workers from Tohoku University, Japan, have performed many experiments using a hydrothermal flow reactor[12-24]. Their equipment is not dissimilar to that used in Nottingham, which itself was based upon the original Japanese design. Both designs involve hot water being mixed with cold metal-salt solution to enable rapid heating. Their reactor does, however, differ in several ways (see Figure 2.7). Firstly, their technique involves the addition of base into the metal-salt stream, to initiate precipitation of metal hydroxides. This necessitates an additional pump, and a T-piece for mixing the

two cold streams. Secondly, their use of two filters in the reactor output allows the collection of larger particles as the reaction occurs, and not just at the end (collection of these larger articles was not deemed important enough in Nottingham to merit this extra complication). Thirdly, the input streams are degassed to remove dissolved oxygen from the precursors. This was occasionally performed separately in Nottingham, by bubbling nitrogen gas through the precursor, but this was not routine.

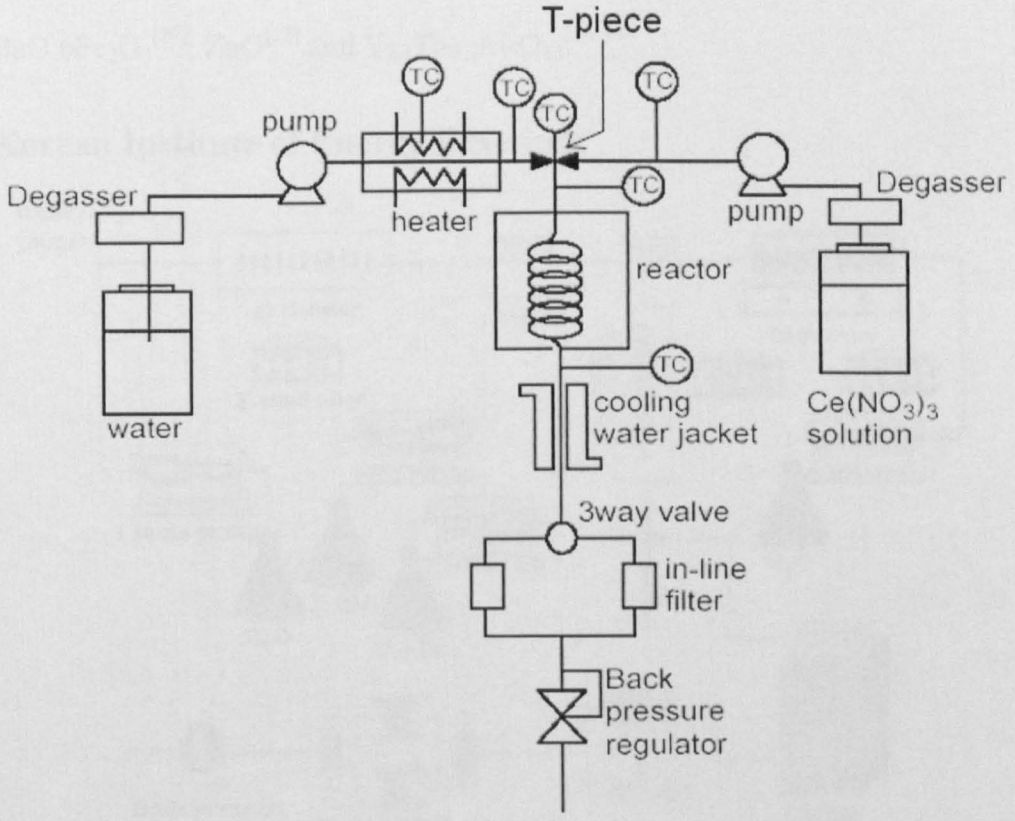


**Figure 2.7: The Tohoku University reactor – upon which the Nottingham design was based (TC – thermocouple). Note particularly the orientation of the T-piece, with inlets at either side, and outlet downwards (reproduced from Hakuta et al.[21]).**

Lastly, and perhaps most importantly, the T-piece is oriented such that the hot water and cold metal-salt solution meet from either side and leave downwards (as in geometry C in the Nottingham reactor simulations). This configuration,

which, like the original Nottingham configuration, is likely to have been arrived at by chance, and not by design, was shown to be less than ideal in reactor simulations. However, the Tohoku group were using much larger flow rates than in Nottingham, so were less likely to encounter stagnant zones and the consequent blocking.

Syntheses of nanoparticles of many different compounds were performed, including $LiCoO_2$[15, 18], $LiMn_2O_4$[18], $CeO_2$[21], $AlO(OH)$[16, 20, 23], $BaO.6Fe_2O_3$[22], $ZnO$[12] and $Y_{2.7}Tb_{0.3}Al_5O_{12}$[14, 19].

## Korean Institute of Energy Research

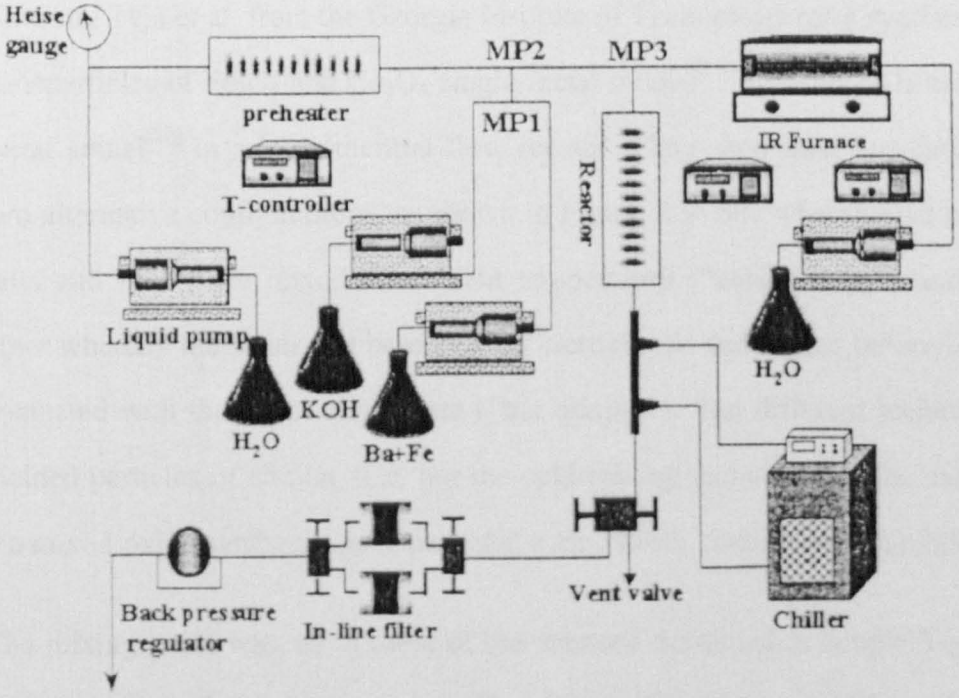


**Figure 2.8: Hydrothermal flow reactor used at the Korean Institute of Energy Research – the reactants are heated in two stages and meet at a simple T-piece before being further heated in a 6 m-long coil reactor (diagram reproduced from Rho and Park[25]).**

A group at the Korean Institute of Energy Research have a flow reactor that they have used to make barium hexaferrite[25, 26]. Their reactor, pictured in

Figure 2.8, differs somewhat from the Tohoku University reactor. The metal-salt stream is mixed cold with KOH base before being heated to 200°C by mixing with a first hot-water stream and then to 400°C by a second hot-water stream. The reaction stream was then passed through a heated reactor coil, 6 m in length. The mixing-point geometry is not specifically mentioned, but appears to consist of a T-piece in the same orientation as used by Tohoku University (with inlets at either side, and outlet downwards). They also collect particles in switchable in-line filters.

## Georgia Institute of Technology, Atlanta, USA

Cote and Teja et al. from the Georgia Institute of Technology have synthesised nanoparticles of $Fe_2O_3$ and $Co_3O_4$ single-metal oxides[27] and $CoFe_2O_4$ mixed-metal spinel[28] in a hydrothermal flow reactor. They used their apparatus in two alternative configurations, as shown in Figure 2.9: one whereby the metal salts and base were mixed at ambient temperature ("cold mixing") and the other whereby the water and base streams were mixed and heated before being contacted with the metal-salt stream ("hot mixing"). The different techniques yielded particles of similar size, but the cold-mixing technique, in the case of the mixed-oxide synthesis, gave particles with a lower content of iron oxide.

The mixing point was, as in most of the reactors examined, a simple T-piece and appears to have been used in the same orientation as in the original experiments at Nottingham: metal salt enters at the top, hot water at the side, with the output at the bottom.

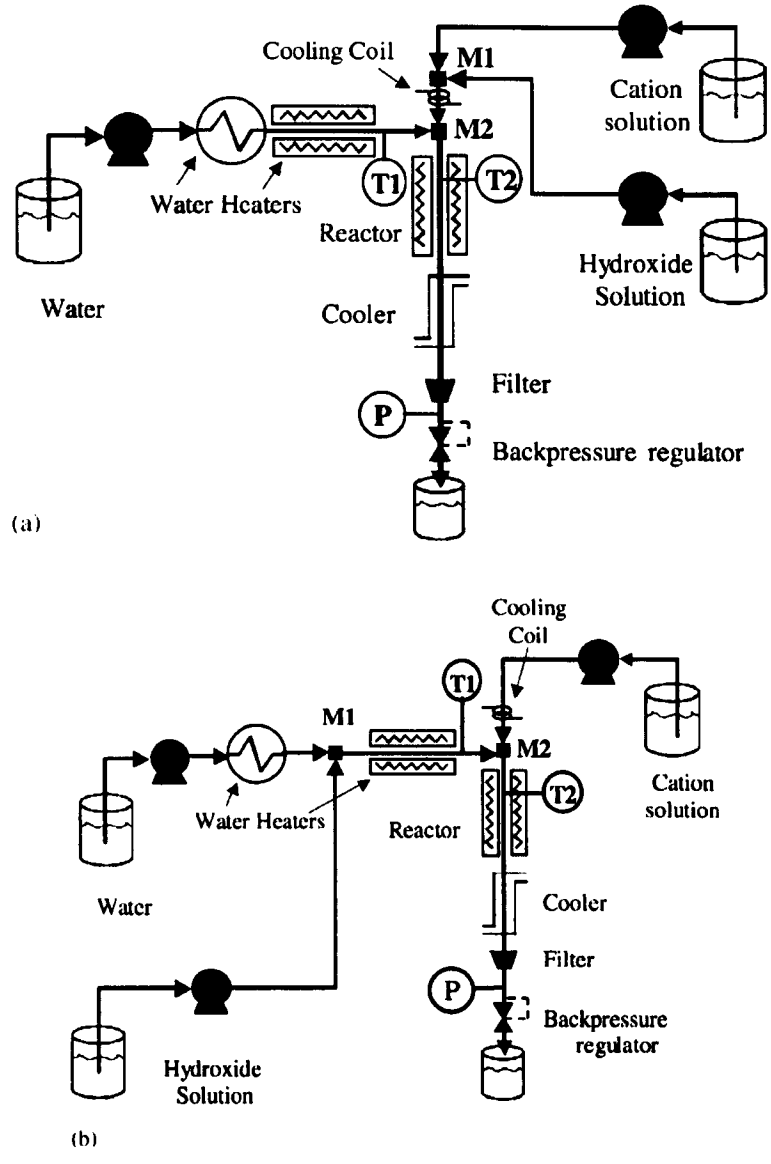


**Figure 2.9: The two alternative configurations of the hydrothermal flow apparatus at the Georgia Institute of Technology. The "cold mixing" regime (a) has the metal-salt and base solutions being mixed before heating takes place, whilst in the "hot mixing" regime (b), the metal-salt stream is mixed with hot hydroxide solution. Both regimes differ little from the other reactors examined here, and use a simple T-piece for mixing.**

## Summary

To the best of my knowledge, all of the hydrothermal flow reactors that involve mixing hot water with metal-salt solution have used a simple T-piece (this excludes the Pacific Northwest group whose reactor involved heating a single stream and therefore did not require any mixing). Whilst different orientations were used, the reactor modelling, performed by Blood et al.[1], has shown that no orientation of a T-piece is particularly well suited for use in this kind of mixing. This therefore necessitated the design of an entirely new reactor geometry.

### *A new nozzle design*

A new nozzle design was proposed by Blood, Lester et al.[3] to overcome the problems of using a simple T-piece. The design consisted of two concentric tubes, one within the other, in a vertical orientation. The larger tube would serve as the inlet for the cold metal-salt solution, which would flow upwards through the mixing point. The smaller tube would inject the hot water downwards into the wider tube. Buoyancy forces would lead to the hot water rising, causing turbulent mixing downstream of the hot-water nozzle, and, since the hot water passes down the middle of the reactor outflow, no heating of the aqueous metal salt occurs upstream of the reactor. The reactor design is shown in Figure 2.10. The additional cone was added to the hot-water nozzle with the intention that it would act as a thin-film reactor, with centrifugal forces being replaced by convection forces.

The nozzle was modelled in Perspex and tested using sucrose solution and methanol as before. However, this time the methanol was dyed blue instead of the sucrose solution, to aid observation of the mixing. A steady-state concentration map of the reactor is shown in Figure 2.10.

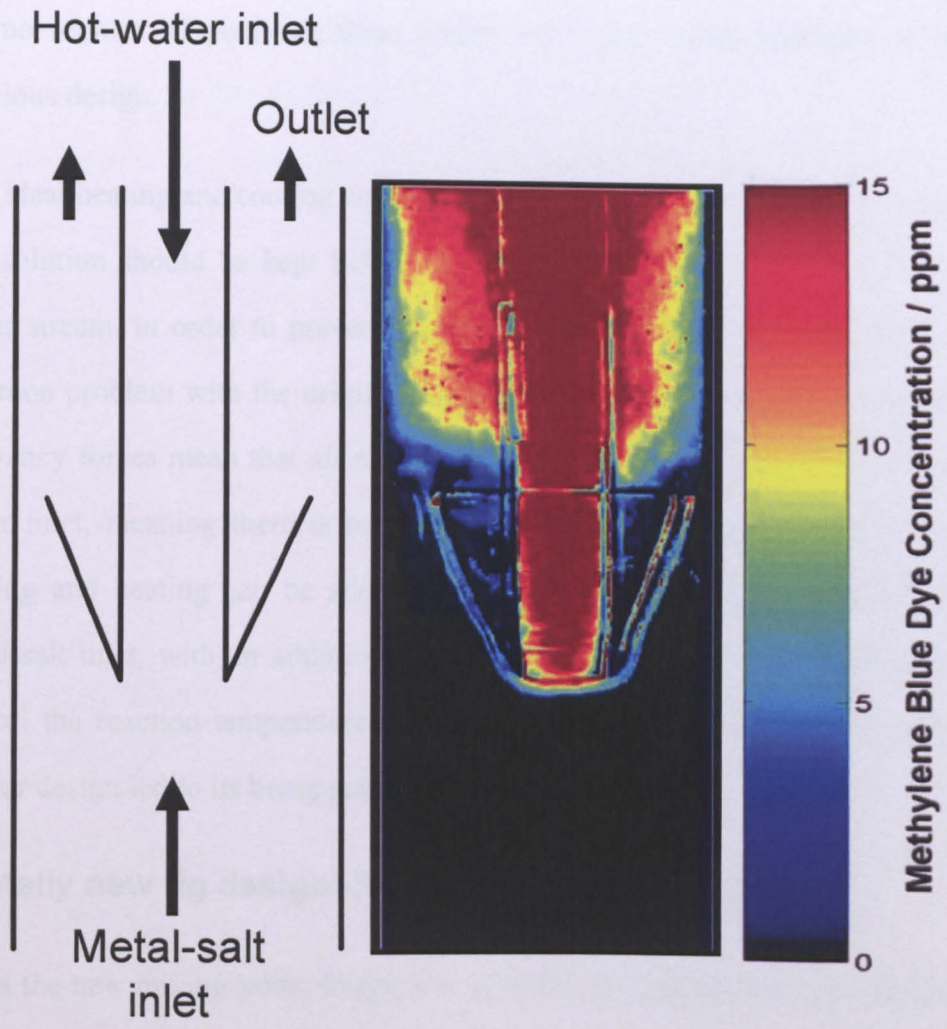


**Figure 2.10: schematic diagram of the new nozzle design, with a steady-state concentration map of the pseudo reactor. Turbulent mixing can be seen to occur downstream of the reactor with no penetration of the hot water into the metal-salt inlet. This is approaching an ideal scenario for the reactor. This time, in contrast to the previous experiments, the methanol solution was dyed blue, in order to better observe the mixing process.**

The mixing was observed to be instantaneous and strong, with the resultant turbulent macromixing eddies being streamlined downstream towards the reactor outlet. These eddies will aid in the transport of particles formed downstream. No contamination is occurring within the reactor inlets, and there

are no regions of poor net flow, which were both major problems in the previous design.

The ideal heating and cooling scenario was also considered. Ideally, the metal-salt solution should be kept below 50°C until it makes contact with the hot water stream, in order to prevent particle precipitation prior to the reactor, a common problem with the original T-piece design. In the new reactor design, buoyancy forces mean that all mixing will take place downstream of the hot-water inlet, meaning there is no premature reaction of the metal salt. Extra cooling and heating can be added: a cooling jacket can be attached to the metal-salt inlet, with an additional heater around the nozzle to maintain and control the reaction temperature. The successful testing of the model of the reactor design led to its being patented[2].

## A totally new rig design: Rig 2

When the new mixing-point design was adopted, the opportunity was taken to set up an entirely new rig, Rig 2, incorporating other new features to address various problems with the old rig.

The nozzle reactor, as modelled by Blood et al., was constructed from Swagelok components, as shown in Figure 2.11. A 3/8-inch tube was used as the outermost wall of the reactor, with an 1/8-inch tube as the inner nozzle, carrying the hot water. A crosspiece allowed for the small tube to sit inside the large tube, and also provided room for a thermocouple, and the reactor outlet. The 3/8-inch reactor outlet left from one side of the cross-piece, but was bent downwards in a curve. This was to avoid too many horizontal surfaces upon which particles might settle, particularly in the wider tubes in the reactor. A further improvement, that might be made if the rig were rebuilt once more, would be to move the cooling coil nearer to the reactor outlet so that the hot

reactor zone would be smaller, and more well-defined. ¼-inch brass tubing was wound around the metal salt inlet below the reactor; the outlet was fitted with a similar cooler. The upper part of the reactor, containing the nozzle, was encased in a cylindrical aluminium block around which a Watlow band heater was fitted. The entire reactor was surrounded by glass wool encased in aluminium foil.

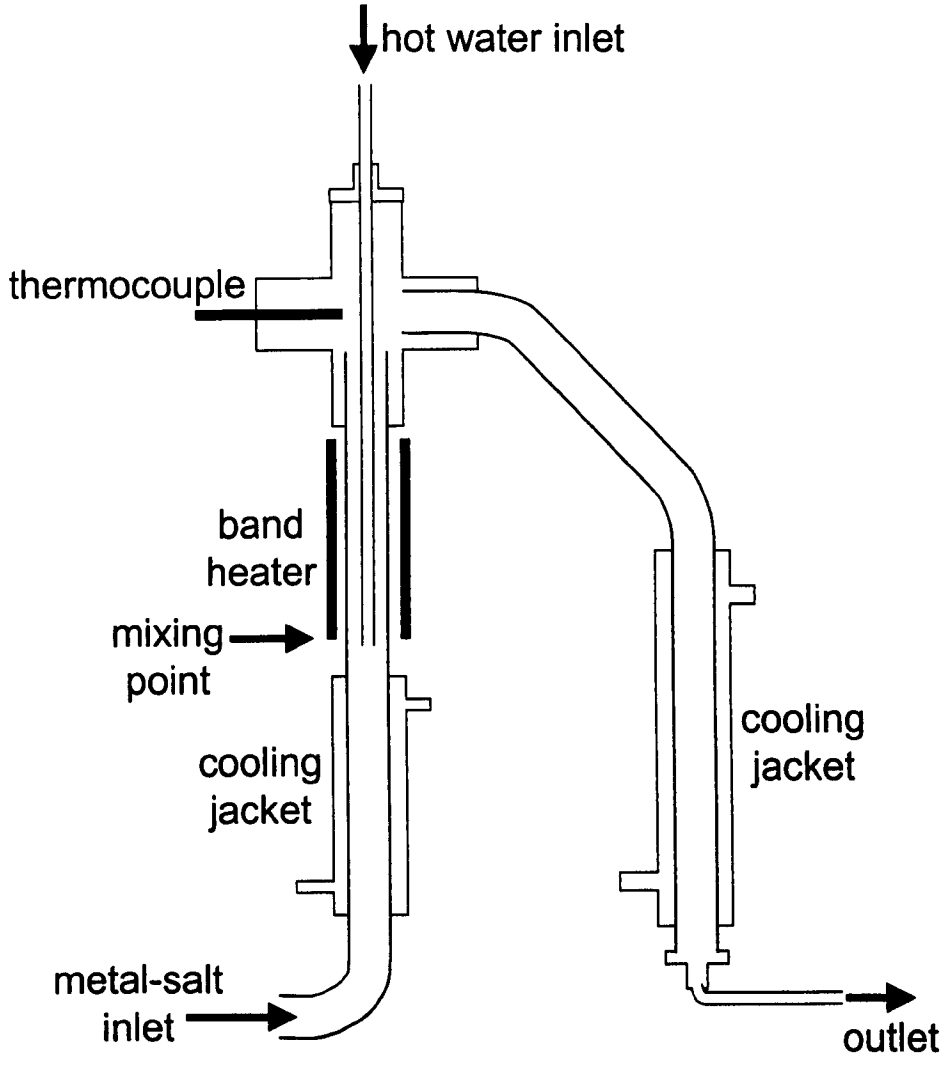


**Figure 2.11: The new reactor design for Rig 2, as built from Swagelok components. The nozzle has been incorporated using two concentric tubes; the outlet tube from the crosspiece is curved to discourage the deposition of particles that might occur on horizontal surfaces, which had previously been encountered.**

The reactor was mounted within a steel box, in which was also fitted a new heater, which was more efficient than the old HPLC oven, and also more easily controllable. The new heater consisted of a cast aluminium block containing coiled 1/2-inch steel tubing, with length of ca. 1 m, through which the water to be heated passed, and a Watlow cartridge heater, with controlling thermocouple. Whilst a cone, consisting of a ferrule, was initially fitted to the internal nozzle, it caused problems with blocking, as it left very little gap for the mixture to flow through, and this feature was eventually removed form the rig.

A new heat exchanger for the final cooling of the reaction mixture was constructed, rather like a Liebig condenser, but in stainless steel, with a 1/8-inch pipe, carrying the mixture, running through the middle of a 3/8-inch pipe carrying flowing cold water.

Despite a vast difference in appearance, the general scheme of Rig 2 remained the same as in Rig 1.

## Outcome

Rig 2 functioned much more reliably than Rig 1. The new preheater allowed a higher temperature to be maintained, and made controlling the temperature much easier. The new, straight heat exchanger harboured fewer particles than the old, coiled version.

Most importantly, the problem of blockages was entirely solved by the new reactor design, even when making compounds that had previously proved the most problematic, such as copper oxide.

### An additional reactor: Rig 3

A further reactor, Rig 3, was built by Dr. Paul Blood, which had a similar design to Rig 2. Rig 3 had a computer controlled Tescom back-pressure regulator, as opposed to the manual regulator in Rig 2. Also, the heater for Rig 3 was able to achieve even higher temperatures than Rig 2. Some results in this Thesis were obtained from experiments performed in Rig 3, as indicated.

## *Conclusions*

The design of Rig 2 has proven to be most satisfactory, and a vast improvement over Rig 1, allowing higher temperatures to be maintained and, crucially, avoiding blockages. In addition, thanks to the modelling of the rig, we now know a great deal more about the fluid dynamics within the reactor, which was invaluable for the redesign of the reactor, and will be equally useful if further modifications are carried out.

## References


[1] P. J. Blood, J. P. Denyer, B. J. Azzopardi, M. Poliakoff, E. Lester, *Chem. Eng. Sci.* **2004**, *59*, 2853.

[2] E. Lester, B. J. Azzopardi, UK, **2004**.

[3] E. Lester, P. J. Blood, B. J. Azzopardi, M. Poliakoff, *J. Supercrit. Fluids* **2005**, *to be published.*

[4] A. Cabanas, J. A. Darr, E. Lester, M. Poliakoff, *Chem. Commun.* **2000**, 901.

[5] A. Cabanas, J. A. Darr, E. Lester, M. Poliakoff, *J. Mater. Chem.* **2001**, *11*, 561.

[6] A. Cabanas, M. Poliakoff, *J. Mater. Chem.* **2001**, *11*, 1408.

[7] A. A. Galkin, B. G. Kostyuk, N. N. Kuznetsova, A. O. Turakulova, V. V. Lunin, M. Polyakov, *Kinet. Catal.* **2001**, *42*, 154.

[8] A. A. Galkin, B. G. Kostyuk, V. V. Lunin, M. Poliakoff, *Angew. Chem.-Int. Edit.* **2000**, *39*, 2738.

[9] T. Adschiri, S. Takami, M. Umetsu, T. Tsukada, in *Sixth International Symposium on Supercritical Fluids, Vol. 2* (Eds.: G. Brunner, I. Kikic, M. Perrut), Versailles, France, **2003**, p. 1237.

[10] D. W. Matson, J. C. Linehan, J. G. Darab, M. F. Buehler, *Energy Fuels* **1994**, *8*, 10.

[11] D. W. Matson, J. C. Linehan, R. M. Bean, *Mater. Lett.* **1992**, *14*, 222.

[12] S. Ohara, T. Mousavand, M. Umetsu, S. Takami, T. Adschiri, Y. Kuroki, M. Takata, *Solid State Ion.* **2004**, *172*, 261.

[13] K. Sue, N. Kakinuma, T. Adschiri, K. Arai, *Ind. Eng. Chem. Res.* **2004**, *43*, 2073.

[14] Y. Hakuta, T. Haganuma, K. Sue, T. Adschiri, K. Arai, *Mater. Res. Bull.* **2003**, *38*, 1257.

[15] T. Adschiri, Y. Hakuta, K. Kanamura, K. Arai, *High Pressure Res.* **2001**, *20*, 373.

[16] T. Adschiri, Y. Hakuta, K. Sue, K. Arai, *J. Nanopart. Res.* **2001**, *3*, 227.

[17] T. Adschiri, Y. Hakuta, K. Arai, *Ind. Eng. Chem. Res.* **2000**, *39*, 4901.

[18] K. Kanamura, T. Umegaki, K. Toyoshima, K. I. Okada, Y. Hakuta, T. Adschiri, K. Arai, in *Electroceramics in Japan III, Vol. 181-2* (Eds.: N. Murata, K. Shinozaki, T. Kimura), **2000**, pp. 147.

[19] Y. Hakuta, K. Seino, H. Ura, T. Adschiri, H. Takizawa, K. Arai, *J. Mater. Chem.* **1999**, *9*, 2671.

[20] Y. Hakuta, T. Adschiri, H. Hirakoso, K. Arai, *Fluid Phase Equilib.* **1999**, *160*, 733.

[21] Y. Hakuta, S. Onai, H. Terayama, T. Adschiri, K. Arai, *J. Mater. Sci. Lett.* **1998**, *17*, 1211.

[22] Y. Hakuta, T. Adschiri, T. Suzuki, T. Chida, K. Seino, K. Arai, *J. Am. Ceram. Soc.* **1998**, *81*, 2461.

[23] T. Adschiri, K. Kanazawa, K. Arai, *J. Am. Ceram. Soc.* **1992**, *75*, 2615.

[24] T. Adschiri, K. Kanazawa, K. Arai, *J. Am. Ceram. Soc.* **1992**, *75*, 1019.

[25] S. Rho, S. Park, *Korean Journal Of Chemical Engineering* **2002**, *19*, 120.

[26] S. C. Nam, G. J. Kim, *Korean Journal Of Chemical Engineering* **2004**, *21*, 582.

[27] L. J. Cote, A. S. Teja, A. P. Wilkinson, Z. J. Zhang, *J. Mater. Res.* **2002**, *17*, 2410.
[28] L. J. Cote, A. S. Teja, A. P. Wilkinson, Z. J. Zhang, *Fluid Phase Equilib.* **2003**, *210*, 307.

# Chapter 3: Copper oxide

## *Summary*

Before the start of this Thesis, experiments on the synthesis of copper oxide nanoparticles had already been performed at Nottingham. These indicated that there might be a dependence of particle size upon the nature of copper precursor used. However, they did not reveal any effect on particle size from adjusting reactor temperature or reagent flow-rates. The research described here was successful in confirming these initial findings, but also revealed a problem with blockages within the reactor, which highlighted the need for redesigning the equipment (see Chapter 2). Initial products obtained were very impure, containing a great deal of copper-salt precursor. It was, however, found that the synthesised particles could be made to settle out from suspension by centrifugation, and that much purer oxide particles could then be obtained by decanting and drying.

The new reactor nozzle design in Rig 2 allowed experiments to be performed without blockages. Work performed after the end of my research revealed that the nature of copper species synthesised was dependent on the reaction temperature.

## Uses for copper oxide particles

Copper (II) oxide has a cooperite structure (analogous to PtS). This structure consists of a roughly simple-cubic array of oxide particles, with half of the faces of the cubes having a copper ion at the centre, as shown in Figure 3.1.

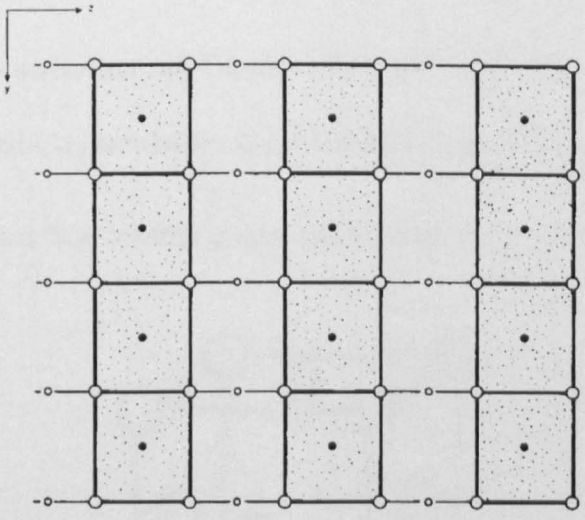

**Figure 3.1: a 2-d projection of the structure of CuO, showing ○ a roughly simple-cubic lattice of $O^{2-}$ ions, with ○● $Cu^{2+}$ ions occupying half of the cubic faces (diagram reproduced from. Hyde et al.[1]).**

Copper (I) oxide has a structure where oxide ions sit at the centre of corner-connected $Cu_4$ tetrahedra, as shown in Figure 3.2.

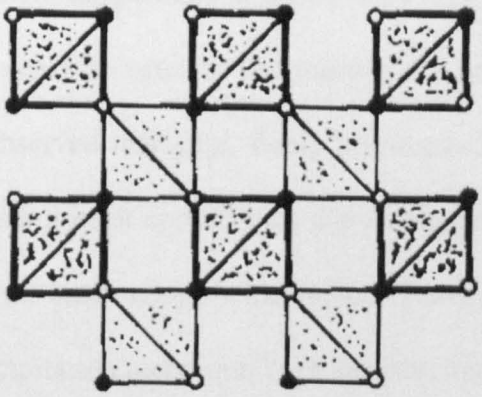

**Figure 3.2: the structure of $Cu_2O$, where $O^{2-}$ ions are at the centre of corner-connected $Cu_4$ terahedra (reproduced from Hyde et al.[1]).**

Copper metal has a face-centred cubic structure, as shown in Figure 3.3.

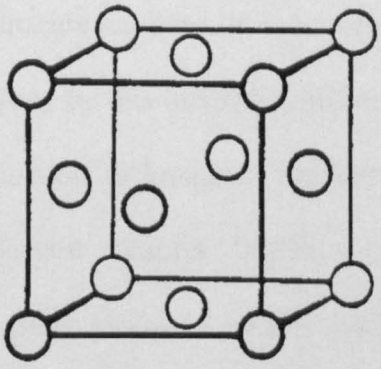

**Figure 3.3: the face-centred cubic structure of copper metal, reproduced from Mak et al.[2]**

Copper oxide nánoparticles have become very interesting in recent years owing to the possibility of using them as materials that remain superconducting at unusually high temperatures[3, 4]. Copper oxide nanoparticles have also found use in applications such as gas sensors[5], solar cells[6] and semiconductors[7]. Copper oxide has found many applications as a catalyst. Examples include its use in the hydrolysis of carbon dioxide to form methanol[8] and in the selective oxidation of carbon monoxide[9]. Catalytic oxidation of carbon monoxide to

carbon dioxide at ambient temperature and pressure is important for respiratory protection[10]. The process is used in the mining industry, and in deep sea diving. It has been observed that gold, finely dispersed on metal oxides, was active for this process but most applications use manganese hopcalite catalyst, $CuMn_2O_4$. Taylor et al. made copper-zinc mixed oxides, as an alternative to hopcalite, by a coprecipitation technique[11] (a surface area of ca. 35 $m^2g^{-1}$ was achieved).

## Other routes for the synthesis of copper oxide

Copper oxide can be made conveniently by thermal decomposition of copper-salt precursors in the solid state[12], for example by pyrolysis of directly-deposited nitrate and hydroxide particles. It is, however, difficult to control the particle size and morphology by this method. Uniform nanoparticles have been synthesised by microemulsion techniques, whereby dissolved reactants are injected into a hot surfactant solution. Whilst some other transition-metal oxides have been successfully produced by this method, problems have been encountered in making CuO because the particles obtained are capped with surfactant molecules which are difficult to remove completely[13].

Vorobyova et al.[14] prepared a stable colloidal solution of CuO particles, with size 6 nm, in octane. This was achieved by mixing a solution of copper oleate in octane with aqueous sodium hydroxide. Kumar et al.[15] employed a sonochemical method to prepare CuO nanoparticles of ca. 6 nm diameter in organic solvents, including dimethyl formamide (DMF). However, these methods are inappropriate for making nanoparticles in large amounts.

Wang et al.[16] performed an ambient-temperature solid-state synthesis of CuO nanowhiskers. Copper chloride and sodium hydroxide were ground together, using polyethylene glycol (PEG) 400 as a soft template. The synthesised nanowhiskers had diameter of ca. 8 nm and length ca. 100 nm.

CuO particles were made by a more convenient alco-thermal method by Hong et al.[17] using copper acetate as a starting material. Almost total conversion was achieved at 110°C, and control over particle sizes in the range 3 nm-9 nm was achieved by adjusting the reaction temperature. At high temperatures, however, the ethanol molecules present reduced the copper (II) oxide to copper metal.

Fan et al.[18] used a precipitation-pyrolysis method to prepare CuO particles of different morphologies. Spherical nanocrystals with diameter ca. 7 nm were synthesised by mixing ammonium carbonate with copper acetate solution and then heating the solid products at 200-500°C. Anisotropic nanorod agglomerations were synthesised by heating precipitated copper hydroxide in the absence of carbonate ions.

Copper and copper oxide particles have been formed with diameters of 17 nm in a supercritical-water batch process; smaller copper nanoparticles were also obtained by Ziegler et al. using a thiol capping ligand[19].

In summary, the reported methods of copper-oxide nanoparticle synthesis mostly rely on toxic or expensive chemicals or high temperatures. Such methods are either unsuitable for making large amounts of particles or suffer from problems of particle sintering, thus forming larger particles.

## Previous copper oxide research at Nottingham

Previous unpublished work was performed in Nottingham by Ilkenhans et al. on the decomposition of copper salts in the hydrothermal flow reactor, using Rig 1[20]. Aqueous solutions of copper nitrate, copper formate and copper acetate precursors were prepared. Copper carbonate was also dissolved in water, which required the addition of ca. 10 $cm^3$ concentrated aqueous ammonia. The individual metal salts were then mixed with hot water under near-critical conditions (ca. 200°C, ca. 200 bar) and then passed through a tube furnace and heated to between 200°C and 400°C.

Some useful conclusions were drawn from this unpublished work, indeed a draft paper was written. With copper acetate or formate as precursor, the anions are thought to react, with any oxygen present, as reducing agents in the supercritical environment. Therefore, according to Scheme 3.1(a-c) (formate) and (d-e) (acetate), copper (I) oxide and metallic copper can be formed, in addition to copper (II) oxide, as observed from analysis of PXD results.

| | | | |
|---|---|---|---|
| a) | $Cu^{2+} + 2\ HCOO^-$ | $\longrightarrow$ | $Cu + H_2 + 2\ CO_2$ |
| b) | $Cu^{2+} + 2HCOO^- + 0.5\ O_2$ | $\longrightarrow$ | $Cu + H_2O + 2\ CO_2$ |
| c) | $2\ Cu^{2+} + 4\ HCOO^- + 1.5\ O_2$ | $\longrightarrow$ | $Cu_2O + 4\ CO_2 + 2\ H_2O$ |
| d) | $Cu^{2+} + 2\ H_3CCOO^-$ | $\longrightarrow$ | $Cu + H_2 + CH_4 + CO_2$ |
| e) | $Cu^{2+} + 2\ H_3CCOO^- + 2.5\ O_2$ | $\longrightarrow$ | $Cu + 3\ H_2O + 2\ CO_2$ |

**Scheme 3.1: mechanism, providing a possible reason for the formation of copper (I) oxide and copper metal from copper salts of carboxylic acids, by which (a-c) formate and (d-e) acetate ions react with oxygen dissolved in water and reduce the copper species**

Before the work reported here was started, an attempt was made to glean more information from the earlier experimenter's results. Particle sizes, as estimated

by PXD, for copper (II) oxide particles (but not the other copper species formed) are plotted in Figure 3.4 against the density of water at the mixing point, the residence time, the concentration of metal at the mixing point and the reactor temperature.

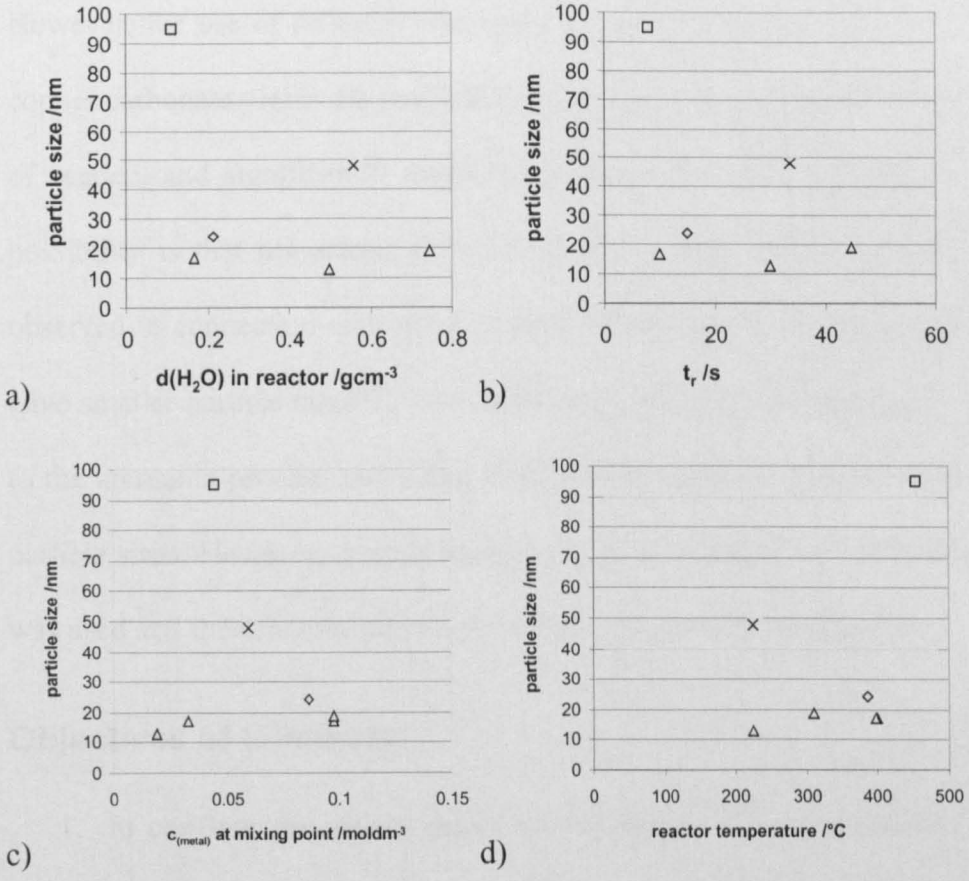


copper salt used as precursor: ◇ acetate; □ formate; △ carbonate; × nitrate

**Figure 3.4: The unpublished work of Ilkenhans et al. suggested that the effect on particle size of variations in reactor temperature and reactant flow rates is negligible compared to that of the nature of the precursor. This can be observed from my plots of CuO particle size, as estimated from PXD measurements vs. a) density of water at mixing point; b) residence time; c) concentration of metal at mixing point; d) reactor temperature with the shape of the data points indicating the copper precursor.**

From Figure 3.4, it would appear that the particle size does not have significant sensitivity to the density of water in the reactor, the residence time, the concentration of the metal salt or the reactor temperature, within the ranges tested.

However, the use of different precursors did give particles of different sizes: copper carbonate yields the smallest CuO particles, slightly smaller than those of acetate, and significantly smaller than those of nitrate and formate. One possibility is that pH affects the particle size, a phenomenon that has been observed in connection with the formation of zinc oxide, in which higher pH gave smaller particle sizes[21]. The carbonate solution is the most basic, owing to the ammonia present, and might therefore be expected to give the smallest particle sizes. However, records were not kept of exactly how much ammonia was used and therefore the actual pH in these reactions is not known.

## Objectives of this work

1. **to confirm the strong effect of the nature of the precursor.** Three different precursors were tested: copper carbonate (which required addition of aqueous ammonia to dissolve), copper formate and copper acetate. PXD analysis of particle sizes was then possible.

2. **to investigate further whether it was possible to control oxidation states of copper in the products.** Ilkenhans had observed the formation of $Cu_2O$ and Cu as well as CuO. The presence $Cu^+$ and $Cu^0$ in addition to the expected $Cu^{2+}$ was therefore investigated by PXD and also by visual observation.

3. **to ensure reliable and repeatable running of the experiments.** The experiments were repeated several times each, in the hope of obtaining similar results and therefore increasing the credibility of later results. The reaction tubing was examined for evidence of blocking that would impede the reliability of the reactor.

4. **to test the suggestions of Ilkenhans et al. regarding the lack of effect of changing reaction conditions.** Differing reaction conditions within the rig allowed some comparison of sizes of particles formed at different temperatures. As discussed in Chapter 1, increasing temperature would be expected to have some effect upon particle size (whether it be an increase or decrease).

## *Results and Discussion*

0.2 mol $dm^{-3}$ solutions of copper (II) carbonate, acetate and formate were prepared in deionised water. A large amount (ca. 100 $cm^3$) of aqueous ammonia was required to dissolve the carbonate to form a deep-blue solution. These solutions were run through Rig 1 (as described in Chapter 2) with a 3.5 ml $min^{-1}$ flow rate. Deionised water was passed through the oven at a rate of 5 ml $min^{-1}$. Each experiment was repeated three (and, in one case, four) times.

The target reaction temperature was ca. 250°C, but it was difficult to control the reactor to reach exactly this temperature for each run; therefore the recorded temperature for each reaction ranged between 200°C and 300°C, as indicated in Table 3.1. Similarly, the pressure fluctuated considerably around the intended 250 bar, and an average value for each experiment is shown in the Table. Accumulation of copper oxide particles within the reactor tubing led to

partial, and sometimes total, blocking of the reactor on numerous occasions. This often led to the premature termination of the experiment and the dismantling and ultrasonic cleaning of the tubing. This blocking is likely to be the cause of the variation in reactor conditions despite unchanging oven temperature, BPR setting and flow rates. Samples obtained were dried in an oven at ca. 70°C and analysed by PXD.

**Table 3.1: Reaction conditions for copper oxide synthesis reactions using different precursors and approximate conditions of 250°C and 250 bar – these conditions were not always attainable, owing to inconsistent performance of Rig 1.**

| Precursor | Reaction no. | | Mixing-point temperature /°C | Pressure /bar |
|---|---|---|---|---|
| $CuCO_3 + NH_3$ | 1 | A | 200 | 240 |
| | | B | 250 | 240 |
| | | C | 270 | 250 |
| | | D | 270 | 250 |
| $Cu(HCO_2)_2$ | 2 | A | 330 | 235 |
| | | B | 260 | 230 |
| | | C | 250 | 235 |
| $Cu(OAc)_2$ | 3 | A | 300 | 240 |
| | | B | 330 | 240 |
| | | C | 270 | 250 |

After finishing experiments 1-3 above, it became clear that a method for purifying copper oxide samples was required. The expected product, black

copper (II) oxide, was always observed in the reactor output, causing the output stream to become grey and translucent. However, the clear blue colour of the copper-salt solution precursor was also present. The particles did not settle of their own accord and were too small to collect by filtration. Evaporation of the water from these raw samples yielded large blue crystals of the copper precursor, amongst which were visible the black copper (II) oxide particles. Analysis of particle size by PXD was usually still possible but sometimes the copper (II) oxide reflections were less intense than those of the precursor impurities.

A further reaction was carried out at 300°C and 250 bar, using copper acetate as the precursor. Successful attempts were made to use a centrifuge to force the particles to settle. It was necessary to run the apparatus for ca. 3h for most of the particles to have settled. The supernatant liquid was then removed and the remaining particles dried in an oven at ca. 80°C. The resulting black powder was submitted to PXD analysis.

PXD results were obtained for every product made. The results for the four samples produced from reaction of copper carbonate are presented in Figure 3.5(a-d); the three produced from copper formate are shown in Figure 3.6(a-c); lastly, the three produced from copper acetate are shown in Figure 3.7(a-c).

Initial inspection of Figure 3.5shows a few narrow peaks and several broader peaks. Narrow peaks suggest large crystallite sizes – these can be attributed to the large particles of precursor that were visible in the dried product. The broader peaks suggest the presence of smaller particles which, by comparison with catalogued copper (II) oxide reflections in Figure 3.8 can be attributed to

CuO. The broad CuO reflections are even more difficult to discern in the remaining diffractograms, as they are partially obscured by the intense, narrow peaks from the left-over precursor.

Comparing PXD results from different samples made using the same precursor, peaks are found at the same 2θ angle in each of the traces. However, the relative intensity of the narrow precursor peaks, compared with that of the broad CuO peaks varies greatly. This is most likely due to a combination of two factors: firstly, the varying conditions (see Table 3.1) of the reactor leading to a different conversions for what were intended to be repeated experiments and secondly, a different amount of CuO becoming lodged within the reactor, which would depend on the reactor conditions and the amount of blocking already having occurred.

In order to compare the CuO particle sizes from different samples, either one or two peaks, corresponding to known, catalogued CuO peaks were chosen from Figure 3.8 for comparison in each of the diffractograms. The choice was made according to which peaks were visible, distinct and unmasked by peaks from unreacted precursor. It was possible to identify peak W (at ca. 35°) for all samples. Peak X (ca. 39°) was identified in the samples from carbonate precursor and peak Y (ca. 62°) was identified in the samples from the formate precursor.

The Scherrer equation was then applied to the selected peaks to obtain estimates of CuO particle size. These are tabulated in Table 3.2 and plotted against mixing-point temperature in Figure 3.9.

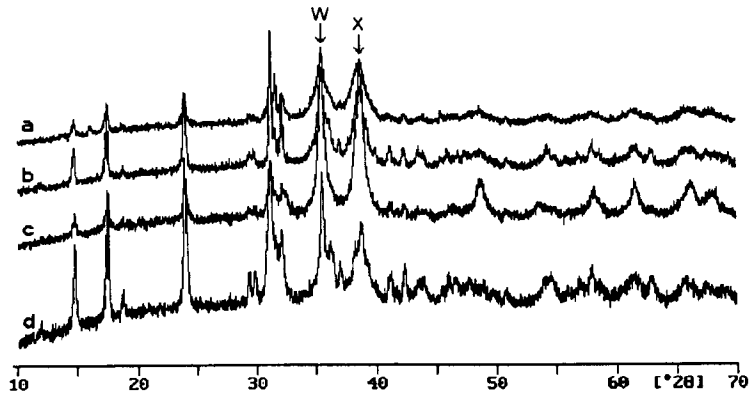


**Figure 3.5: PXD of products from four reactions of carbonate precursor**

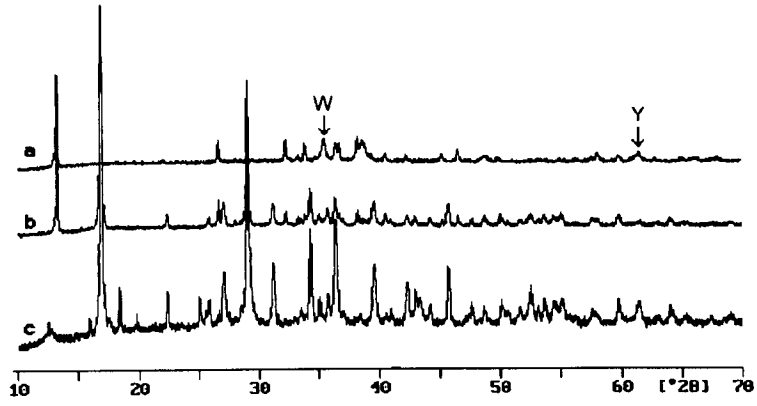


**Figure 3.6: PXD of products from three reactions of formate precursor**

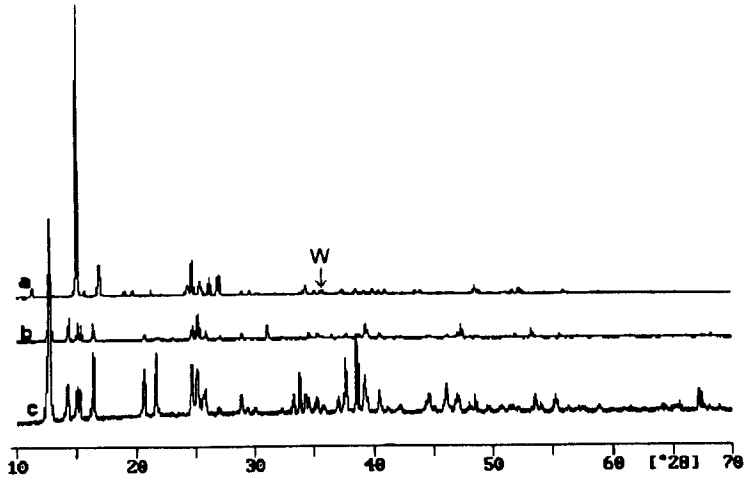


**Figure 3.7: PXD of products from three reactions of acetate precursor**

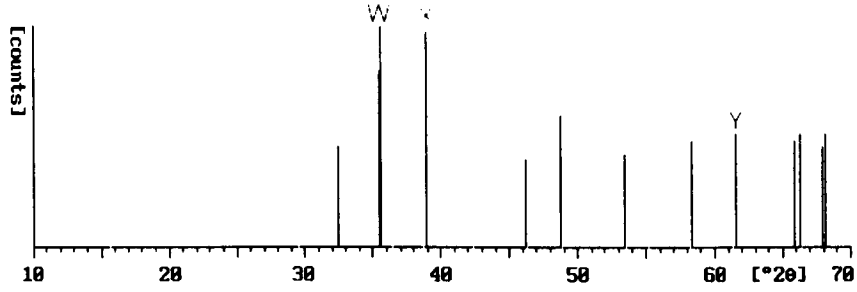


**Figure 3.8: catalogued reflections for CuO, showing which peaks (W, X and Y) were used to estimate particle sizes, as indicated in Table 3.2.**

**Table 3.2: Particle sizes of copper oxide samples as estimated by the Scherrer equation, using two peaks (or, in the case of experimental series 3, one) as labelled in Figure 3.5-Figure 3.7**

| Precursor | Reaction no. | | Particle size /nm | |
|---|---|---|---|---|
| | | | From peak W | From second peak (X or Y as indicated) |
| $CuCO_3 + NH_3$ | 1 | A | 8.5 | (X) 6.6 |
| | | B | 62.7 | (X) 8.6 |
| | | C | 19.3 | (X) 13.5 |
| | | D | 32.1 | (X) 9.5 |
| $Cu(HCO_2)_2$ | 2 | A | 32.3 | (Y) 20.0 |
| | | B | 245.5 | (Y) 8.7 |
| | | C | 203.6 | (Y) 36.5 |
| $Cu(OAc)_2$ | 3 | A | 130.4 | |
| | | B | 53.8 | |
| | | C | (too small to fit profile) | |

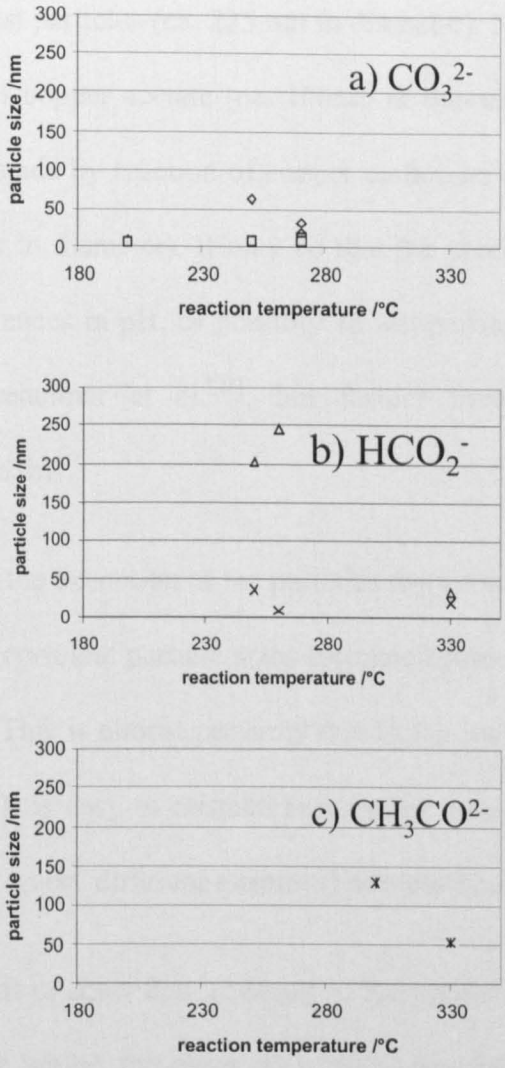


**Figure 3.9: There is a strong relationship between the nature of the precursor and particle size, but a less conclusive one between reaction temperature and particle size. This can be observed from the graphs of particle size vs. mixing-point temperature from (a) carbonate (b) formate and (c) acetate precursors. Data points correspond to estimated particle sizes from different reflections as shown in Table 3.2: ◇△∗ from peak W, □ from peak X, × from peak Y**

Figure 3.9 reveals a strong dependence of particle size upon the nature of the precursor. Comparison of the sizes estimated from the W reflections (at 2θ of ca. 35°) reveals that the copper formate precursor forms particles of copper (II)

oxide with the largest particles (ca. 225 nm in diameter). Next largest are those made by reaction of copper acetate (ca. 100nm in diameter) and the smallest particles are those made by reaction of copper carbonate dissolved in aqueous ammonia (ca. 50nm in diameter). It may be that the precursor affects particle size owing to differences in pH, or possibly an ion-pairing effect, as has been observed by Partneheimer et al.[22], but further investigation would be necessary to confirm this.

It appears that, with the exception of the particles from the carbonate precursor, it is not possible to correlate particle sizes estimated from different reflections on the same graph. This is almost certainly due to the indistinct CuO peaks in the diffractograms. It is easy to mistake two almost coincident peaks for one peak thus leading to a very different estimated particle size.

Figure 3.9 also seems to show that, contrary to the predictions made, changing reaction temperature within the range 200-330°C has little effect on particle size. However, the fluctuation in temperature in any one experiment was very great – several tens of degrees – so one might expect to not be able to correlate particle size with it.

The PXD results from the sample in which particles were made to settle by centrifuging, and then separated from unreacted, dissolved precursor by removing the supernatant liquid and drying the remaining particles, showed much less contamination from the precursor – indeed, the copper acetate reflections were almost undetectable.

## *Conclusions*

### Preliminary conclusions from this work

This new research suggests that, in agreement with previous work, changing reaction temperature, in spite of predictions, seems to have a negligible effect on the size of particles produced (although, since the temperature fluctuations were so large, any results were unlikely to be conclusive). However, precursor identity has a definite effect, showing that reaction of copper formate yields the largest particles, and carbonate the smallest. Ilkenhans et al. noticed the formation of mixtures of copper (II) oxide with copper (I) oxide and copper metal. Only copper (II) oxide was seen to form in this work.

A later experiment showed that centrifuging is a very effective way of forcing the copper oxide samples to settle. This allowed the majority of the unwanted precursor to be removed by removing the supernatant liquid.

Perhaps the most important conclusion from this copper work was the necessity for a new rig design. Blockages were occurring so often that research was becoming impractical. This prompted the total redesign of the mixing zone as described in Chapter 2. Rig 2 was used for the work described in Chapters 5 and 6 and it was then possible to return to the copper-oxide work for one more experiment. After the construction of Rig 2, copper oxide experiments could be performed with very infrequent blocking, and a very much more systematic approach was possible.

One final experiment was performed using copper acetate in Rig 2 (see Chapter 2) but the same reaction conditions as before (300°C, 250 bar). As was hoped,

no blockages occurred during the operation of the rig and about 1 g of particles was collected. This sample was submitted to BET surface-area analysis. BET analysis of the product produced within Rig 2 revealed that the copper oxide sample had surface area of 20 $m^2g^{-1}$.

Further experiments with copper compounds were performed, by Jun Li and Paul Blood, after my work at Nottingham had finished. Rig 2 was used, incorporating the new reactor geometry.

Experiments with a copper formate precursor were carried out at varying temperatures. It was observed that, at mixing temperatures greater than 200°C, gas was being formed in the reactor and bubbling occurred at the end of the reactor tubing. It is thought that this gas might have been hydrogen, or carbon monoxide gas, as suggested by Scheme 3.1. At mixing temperatures greater than 350°C, blockages formed quickly in the reactor, forcing the reaction to be aborted. On dismantling the reactor, it was discovered that the blockage consisted not of black CuO, but of red, lustrous copper metal.

In order to attempt to counteract the reduction process, hydrogen peroxide was added to the water feed and the same experiments run again. As had been hoped, this caused black CuO to form at a mixing temperature of 250°C. Experiments were also carried out using copper acetate solution as a precursor, for comparison with the experiments with formate. At a mixing-point temperature as low as 110°C, small amounts of black CuO were forming. At 200°C, much larger amounts of the same black CuO material were forming, in contrast to the copper metal formed from the copper formate precursor. As the most-oxidised copper (II) oxide product was already forming, it was found

that, as might be expected, the addition of peroxide to the heated water feed appeared to have no effect.

It would appear from these new experiments that formation of copper metal causes blockages much more quickly than formation of copper (II) oxide. During my earlier work, formation of copper metal was never observed; however blocking nonetheless occurred. Rig 1 was still being used at that time in which, unlike Rig 2, a simple T-shaped mixing piece was used. This would allow blocking to occur even if only CuO was formed. In addition, it is probable that the actual reaction was taking place in a cooler part of the reactor, in the cold metal-feed pipe, upstream of the nominal mixing point. As the higher temperatures obtainable in Rig 2 were not reached, it was therefore impossible to make copper metal Rig 1.

## Final conclusions

After having surmounted the problem of reactor blockages, it is now possible to make copper (II) oxide continuously. Good control is possible over the oxidation state of the copper species formed. Some control has been achieved over particle size by the use of different precursors.

## Possible future work

The next stage would be to attempt to achieve some form of continuous control over particle size; this is likely to involve finding out why different precursors have the effect they do, and perhaps investigating the use of precursor mixtures of different pH.

## References


[1] B. G. Hyde, S. Andersson, *Inorganic Crystal Structures*, John Wiley and Sons, New York, **1989**.

[2] T. C. W. Mak, G. Zhou, *Crystallography in Modern Chemistry*, John Wiley and Sons, New York, **1992**.

[3] J. B. Goodenough, *J. Phys.-Condes. Matter* **2003**, *15*, R257.

[4] P. C. Dai, H. A. Mook, G. Aeppli, S. M. Hayden, F. Dogan, *Nature* **2000**, *406*, 965.

[5] R. B. Vasiliev, L. I. Ryabova, M. N. Rumyantseva, A. M. Gaskov, *Uspekhi Khimii* **2004**, *73*, 1019.

[6] Y. Chang, J. J. Teo, H. C. Zeng, *Langmuir* **2005**, *21*, 1074.

[7] H. Wang, J. Z. Xu, J. J. Zhu, H. Y. Chen, *J. Cryst. Growth* **2002**, *244*, 88.

[8] J. F. Deng, Q. Sun, Y. L. Zhang, S. Y. Chen, D. Wu, *Appl. Catal. A-Gen.* **1996**, *139*, 75.

[9] G. Avgouropoulos, T. Ioannides, H. Matralis, *Appl. Catal. B-Environ.* **2005**, *56*, 87.

[10] B. Solsona, G. J. Hutchings, T. Garcia, S. H. Taylor, *New J. Chem.* **2004**, *28*, 708.

[11] S. H. Taylor, G. J. Hutchings, A. A. Mirzaei, *Chem. Commun.* **1999**, 1373.

[12] C. Carel, M. Mouallem-Bahout, J. Gaude, *Solid State Ion.* **1999**, *117*, 47.

[13] J. Rockenberger, E. C. Scher, A. P. Alivisatos, *J. Am. Chem. Soc.* **1999**, *121*, 11595.

[14] S. A. Vorobyova, A. I. Lesnikovich, V. V. Muchinskii, *Colloid Surf. A-Physicochem. Eng. Asp.* **1999**, *150*, 297.

[15] R. V. Kumar, Y. Mastai, Y. Diamant, A. Gedanken, *J. Mater. Chem.* **2001**, *11*, 1209.

[16] W. Z. Wang, Y. J. Zhan, X. S. Wang, Y. K. Liu, C. L. Zheng, G. H. Wang, *Mater. Res. Bull.* **2002**, *37*, 1093.

[17] Z. S. Hong, Y. Cao, J. F. Deng, *Mater. Lett.* **2002**, *52*, 34.

[18] H. M. Fan, L. T. Yang, W. S. Hua, X. F. Wu, Z. Y. Wu, S. S. Xie, B. S. Zuo, *Nanotechnology* **2004**, *15*, 37.

[19] K. J. Ziegler, R. C. Doty, K. P. Johnston, B. A. Korgel, *J. Am. Chem. Soc.* **2001**, *123*, 7797.

[20] T. Ilkenhans, J. A. Darr, P. A. Hamley, M. Poliakoff, *Unpublished Work* **2001**.

[21] S. Music, D. Dragcevic, M. Maljkovic, S. Popovic, *Mater. Chem. Phys.* **2003**, *77*, 521.

[22] Y. S. Chen, J. L. Fulton, W. Partenheimer, *J. Am. Chem. Soc.* **2005**, *127*, 14085.

# Chapter 4: Titania and titanium-ruthenium oxides

## *Summary*

The synthesis of rutile-phase $Ru_xTi_{1-x}O_2$ with $0 \leq x \leq 1$ was attempted using ruthenium nitrosyl nitrate and titanium oxynitrate. Further attempts were made to make rutile-$TiO_2$ and $Ru_xTi_{1-x}O_2$ using alternative precursors.

Although several valuable lessons were learned, the conclusion was that it is not possible to make rutile-phase titanium compounds by this process, except by calcination of the products at very high temperatures.

## *Introduction*

Titania ($TiO_2$) particles are useful as catalytic supports and to photocatalyse reactions. Titania acts as a photosensitiser for photovoltaic cells[1] and can be used as an electrode coating in photoelectrolysis cells[2] to enhance the efficiency of splitting water into its component elements.

In mildly reducing atmospheres, titania will become sub-stoichiometric by losing oxygen. The material then becomes a semiconductor with resistivity related to the oxygen content of the surrounding atmosphere. Titania can therefore be used in oxygen sensors[3].

Its photocatalytic activity allows thin coatings of titania to exhibit self-cleaning and disinfecting properties. This has led to its use in anti-microbial coatings[4].

Titania also has a high refractive index, second only to diamond, which leads to its use as the most common white pigment for paints, as a high paint opacity is achievable with only a small amount of pigment[5]. There are four naturally occurring morphologies of $TiO_2$[6], which will be discussed in the following sections.

The rutile $TiO_2$ structure is shown in Figure 4.1, below. Rutile $TiO_2$ is a common mineral found in igneous, metamorphic and sedimentary rocks. Each titanium atom is surrounded by six oxygen atoms approximately at the corners of a regular octahedron. Each oxygen atom is surrounded by three titanium atoms in an approximately equilateral triangle. Rutile has a tetragonal unit cell, meaning that two of the lattice parameters are equal to one another, $a \neq b = c$, and the angles between the unit-cell axes are all right angles.

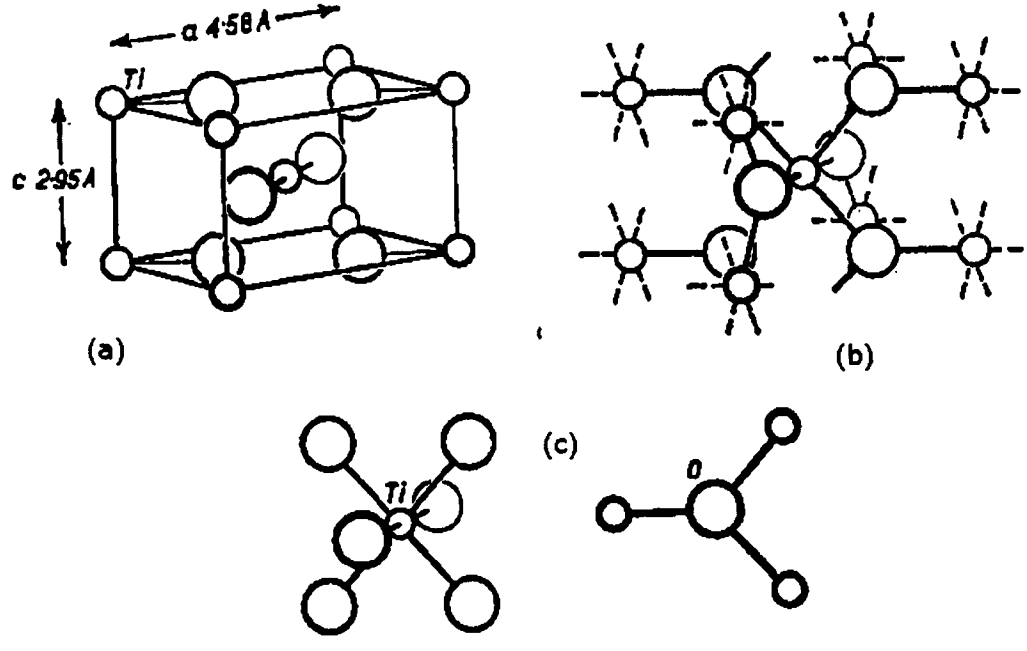


**Figure 4.1: The structure of rutile $TiO_2$ showing (a) the unit cell and lattice parameters (b) the bonds between Ti and O and (c) the environment of Ti and O atoms. Figure reproduced from "Crystal Structures of Minerals" by Bragg and Claringbull[7]**

Anatase is found mostly in sediments and hydrothermal veins[8]; the structure is presented in Figure 4.2, below. It also has a tetragonal unit cell. The coordination of titanium (each atom surrounded by six oxygen atoms) and oxygen (each atom surrounded by three titanium atoms) is the same as for rutile, but the $TiO_6$ octahedron is slightly more distorted. The rutile and antase structures are therefore alternative 6:3 coordinate structures.

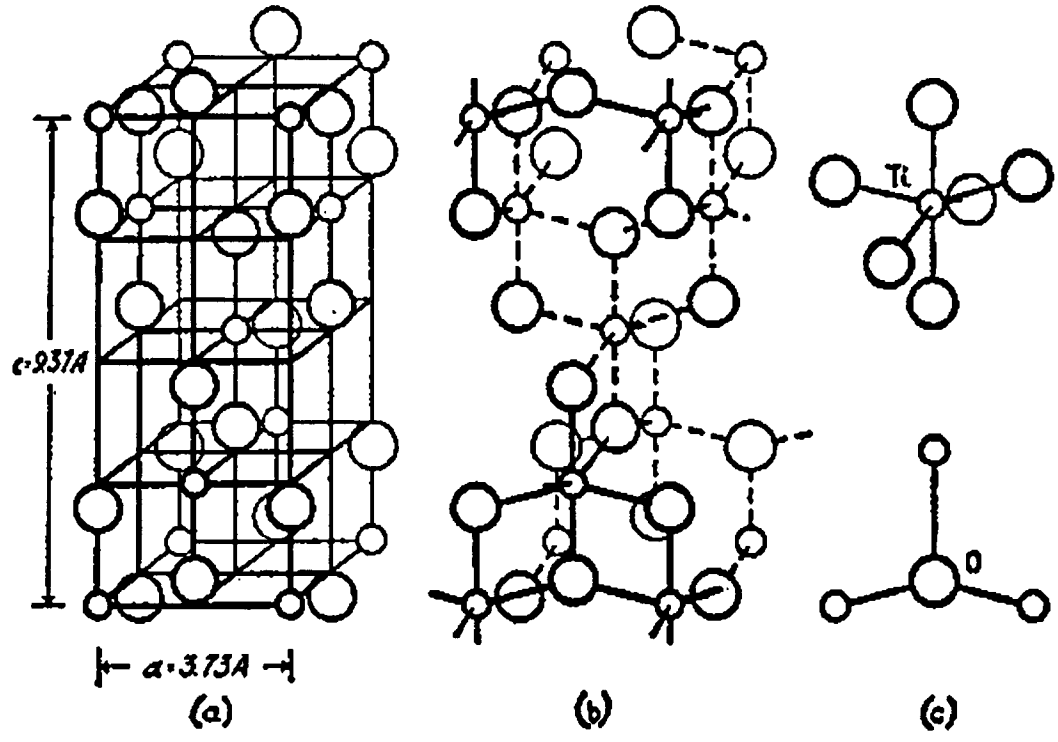


**Figure 4.2: The structure of anatase $TiO_2$ showing (a) the unit cell and lattice parameters (b) the bonds between Ti and O and (c) the Ti and O environments, closely similar to those in the rutile polymorph. Figure reproduced from "Crystal Structures of Minerals" by Bragg and Claringbull[7].**

The remaining naturally-occurring $TiO_2$ polymorphs, brookite and $TiO_2$ (B) are much rarer and are found in hydrothermal geological zones. Brookite has an orthorhombic unit cell (a cuboid with three different lattice parameters, $a \neq b \neq c$, and axes separated by right angles). The recently-discovered $TiO_2$ (B) is monoclinic (the unit cell is a rhomboid with two axes related by right angles, $\alpha = \gamma = 90° \neq \beta$, and three unequal lattice parameters, $a \neq b \neq c$). Like rutile and anatase, all are based upon $TiO_6$ octahedral units.

At temperatures above ca. 600°C (at 1 bar pressure), anatase crystals will convert to a rutile structure (see Figure 4.3). This temperature is much higher than the 300-400°C achievable within the reactor, so it is not possible to form a

rutile $TiO_2$ phase from anatase thermodynamically. However, its direct formation might be possible via kinetic factors.

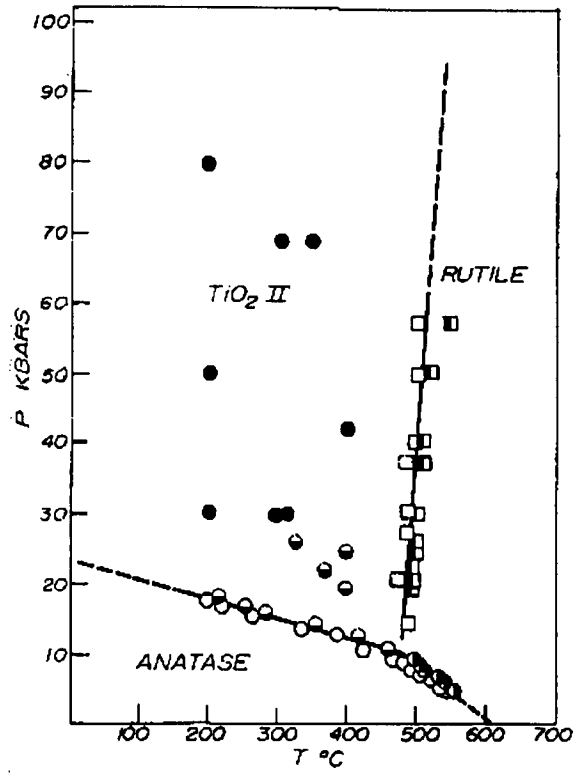


**Figure 4.3: phase diagram showing effects of temperature and pressure on anatase: anatase is converted to rutile at ca. 600°C and 1 bar. The conversions from anatase to other polymorphs are non-reversible. ($TiO_2$ II is a titania polymorph not found in nature, and only formed at much higher pressures than will be considered here) – reproduced from a paper by Dachille et al.[9]**

During the process of conversion from one phase to another, small particles will sinter, leading to the formation of larger particles and lower surface areas thus impairing the catalytic activity or damaging the catalytic support. Therefore, it would be very useful to be able to synthesise nanoparticulate rutile titania directly to avoid this problem. Alternatively, it might be possible to dope the titanium dioxide with another metal in order to form a single-phase rutile structure that would be stable to high temperatures.

It was hoped that using the hydrothermal formation of oxides in the flow reactor would lead to a simple one-step path to rutile titania or ruthenia-titania structures. Different preparation conditions and precursors can lead to different morphologies of product, so it was thought that it might be possible to make rutile titania. The flow reactor had already been used by Cabañas et al.[10] to make single-phase mixed oxides of cerium and zirconium by simply using a mixture of two different metal salts as precursor. It was considered possible that a mixture of ruthenium and titanium salts might be prepared in the same way as a precursor for mixed ruthenium-titanium oxides.

Previous experiments by Cabañas et al.[10] had successfully used nitrate and acetate salts as precursors. Different combinations of ruthenium (III) nitrosyl nitrate, ruthenium (IV) acetate, and titanium oxynitrate solutions were therefore used as precursors, as detailed in the experimental section below. Alternative precursors were also tried, including titanium oxysulfate. For a mixed-metal oxide phase to be made, it is necessary for the metal salts to have similar hydrothermal stability, otherwise the oxides are likely to form separately in different parts of the reactor. As the ruthenium salts were generally more stable to hydrothermal conditions than the corresponding titanium salts, it was decided to try to use some solutions of stable titanium complexes as precursors, where, unlike the simpler salts, the ligands remain bound to the metal atom when dissolved. These were obtained from Johnson Matthey. VERTEC VEXP0424 (a titanium-chelate complex dissolved in diethylene glycol) and ammonium titanium lactate complex were both tried as precursors.

Portions of the mixed-oxide samples were calcined in the hope of causing any separate ruthenia or titania phases to form a single phase. Calcination had led to conversion of separate phases of lanthanum hydroxide and copper oxide to

form a single lanthanum cuprate phase with little loss of surface area in the hydrothermal synthesis work of Galkin et al.[11].

Despite the use of a variety of precursors, it would appear that it is not straightforward to form rutile titania or titania-ruthenia structures using this hydrothermal technique.

## *Experimental*

Solutions of titanium oxynitrate and ruthenium nitrosyl nitrate, with total metal-ion concentration of 0.1 M, were reacted, in Rig 1, in combinations according to Table 4.1. Conditions used were 300°C and 250 bar, with flow rates of 10 ml $min^{-1}$ for water and 5 ml $min^{-1}$ for the metal salt solution. The experiments were given the index TITB*x* (titanium series B; TITA covered preliminary experiments not reported here).

Powders ranging from white, through grey, to black were collected. The particles were observed to settle of their own accord without the centrifugation required for the copper oxide work in Chapter 3. The supernatant liquid was removed by pipette and the remaining material was dried overnight in an oven at ca. 80°C. A portion of each sample was calcined at 500°C for 5h to investigate the effects of heating on crystal morphology. Sample, TITB4, was inadvertently heated to 1200°C for ca. 15 min.

**Table 4.1: different proportions of titanium oxynitrate and ruthenium oxynitrate (with total metal-ion concentration 0.1 mol $dm^{-3}$) used in the TITB series of experiments**

| Experiment code | Proportion Ti:Ru |
|---|---|
| TITB1 | 0:100 |
| TITB2 | 20:80 |
| TITB3 | 40:60 |
| TITB4 | 60:40 |
| TITB5 | 80:20 |
| TITB6 | 100:0 |

Further attempts were made to make rutile-phase titania or ruthenia-titania, as presented in Table 4.2. Different metal-salt precursors were tried, and, in one case, ethanol was used to make the precursor solution, as indicated. Titanium oxynitrate was prepared as required from titanium oxychloride by precipitating with aqueous ammonia and dissolving in 5 eq. nitric acid. Titania precipitates from this solution if it is left overnight. After the products had settled, the supernatant liquid was removed and the samples dried in an oven overnight at ca. 80°C.

**Table 4.2: precursors and conditions for further experiments to make titania and/or ruthenia using alternate reagents**

| Reagents and Ti:Ru ratio | Concentration | Conditions | Comments |
|---|---|---|---|
| Ruthenium acetate, titanium oxynitrate 1:1 | 0.05 $moldm^{-3}$ | 300°C, 250 atm | |
| Titanium oxysulfate only | 0.05 $moldm^{-3}$ | 300°C, 250 atm | |
| Titanium oxynitrate only | 0.05 $moldm^{-3}$ | 300°C, 250 atm | |
| Proprietary VERTEC VEXP0424 titanium chelate (in diethylene glycol) with ruthenium acetate 95:5 | 0.05 $moldm^{-3}$ | 300°C, 250 atm | VERTEC VEXP0424 supplied by Johnson Matthey<br><br>Experiment tried both with and without addition of aqueous ammonia; |
| Ammonium titanium lactate with ruthenium acetate | 0.1 $moldm^{-3}$ | | |
| Titanium oxysulfate and ruthenium nitrosyl nitrate 80:20 | 0.05 $moldm^{-3}$ | 300°C, 250 atm | Reaction was performed using precursor solution in ethanol (but reacting with hot water as in other experiments) |

## *Results and discussion*

Identification of phases present is possible by examination of the diffractograms, and comparison with catalogued data for powder X-ray reflections. The PXD of the uncalcined sample TITB6 is considered first (see Figure 4.3).

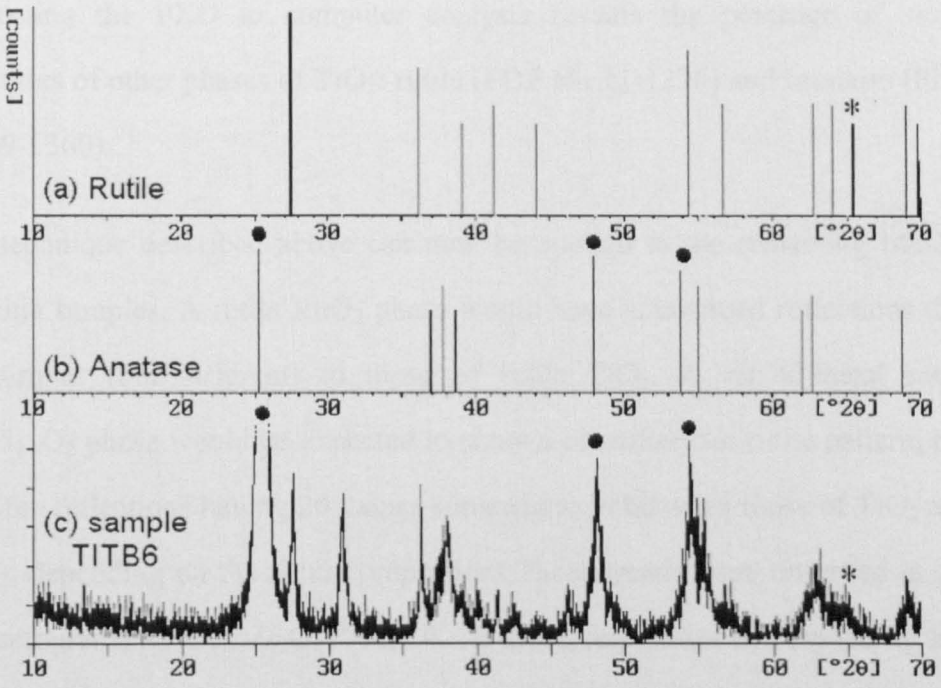


**Figure 4.3: Comparing (c) the PXD (with highest peak cropped) of the TITB6 (pure titania) sample with the characteristic reflections for (a) rutile $TiO_2$ and (b) anatase $TiO_2$, it can be seen that (c) exhibits all anatase reflections shown in (b) (for example, at $2\theta = 25°$, 48°, 54° etc., indicated by •) and does not show the expected peaks for rutile shown in (a) (for example, at $2\theta = 65°$ indicated by *). One can conclude that the major product present is anatase $TiO_2$. The peak-breadth gives an indication of particle size: the broad peaks present suggest small particles.**

The PXD diffractogram can be compared, either by eye, or using computer software, with catalogued PXD data for possible compounds.

It can be seen, even by cursory observation, that the reflections in the PXD for TITB6 (Figure 4.3(c)) correspond to the anatase polymorph (PDF No 21-1272) of $TiO_2$ (Figure 4.3(b)) and not to those of the rutile polymorph (Figure 4.3(a)). Subjecting the PXD to computer analysis reveals the presence of small quantities of other phases of $TiO_2$: rutile (PDF No 21-1276) and brookite (PDF No 29-1360).

The technique described above can now be applied to the remaining titania-ruthenia samples. A rutile $RuO_2$ phase would have catalogued reflections that are similar (but different) to those of rutile $TiO_2$. A mixed-metal rutile $Ru_xTi_{1-x}O_2$ phase would be expected to show a characteristic rutile pattern, but with the reflections having $2\theta$ values somewhere in between those of $TiO_2$ and $RuO_2$, depending on the actual proportions.These trends were observed in the diffractograms for $Ce_{x-1}Zr_xO_2$[10]: for $0 \leq x \leq 0.8$, reflections corresponding to a tetragonal structure were observed, but with larger $2\theta$ values owing to the smaller size of the $Zr^{4+}$ ions relative to the $Ce^{4+}$ ions.

PXDs were obtained for uncalcined (Figure 4.4) and calcined (Figure 4.5) samples of TITB1-6.

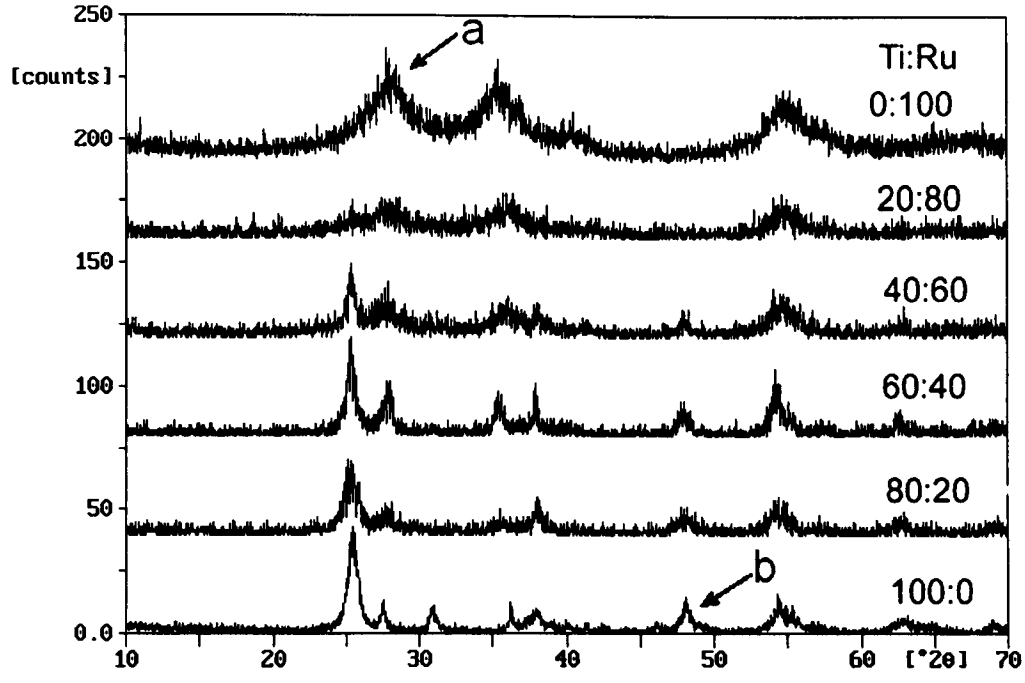


**Figure 4.4: PXD traces for uncalcined samples containing varying proportions of ruthenium and titanium oxide as indicated; the breadth of peaks, as indicated by arrows, at (a) ca. 28° was examined to estimate $RuO_2$ particle size and (b) ca. 47° to estimate $TiO_2$ (anatase) particle size**

In Figure 4.4, the characteristic pure rutile-type $RuO_2$ (TITB1) and anatase $TiO_2$ (TITB2) diffractograms are observed as the top and bottom lines. When moving down the Figure, the mixed-metal samples (TITB2-5) can be seen to exhibit reflections characteristic to both $RuO_2$ and antase-$TiO_2$. This superposition of the two different sets of reflections suggests that both phases are present, providing evidence that no significant amount of single-phase ruthenia-titania material was made (however, phases consisting of less than ca. 5% of the product are difficult to detect by PXD).

To gauge particle sizes, the line widths of distinctive peaks attributed to $RuO_2$ (at $2\theta$ = ca.28°) and anatase $TiO_2$ (at $2\theta$ = ca.47°) were examined, and the Scherrer equation employed to estimate the crystallite size. An estimation of the accuracy, when measuring line width of the $RuO_2$ reflection at ca. 28° to the nearest pixel, was made. The results are presented in Table 4.3.

**Table 4.3: particle sizes for the $RuO_2$ and $TiO_2$ phases present in samples analysed by PXD from experiments using precursors containing different proportions of ruthenium nitrosyl nitrate and titanium oxynitrate (as indicated). Particle sizes were calculated using the Scherrer equation.**

| | | Particle size /nm | | | |
|---|---|---|---|---|---|
| | Ru:Ti | $RuO_2$ (ca. 28°) | $TiO_2$ anatase (ca. 47°) | estimated % error in RuO2 size | Phases present |
| TITB1 | 100:0 | 19 | | 25 | $RuO_2$ |
| TITB2 | 80:20 | 15 | | 13 | $RuO_2$, minor: anatase $TiO_2$, poorly crystalline $Ru_xTi_{1-x}O_2$ |
| TITB3 | 60:40 | 19 | 143 | 9 | $RuO_2$, anatase $TiO_2$, poorly crystalline $Ru_xTi_{1-x}O_2$) |
| TITB4 | 40:60 | 108 | 97 | 11 | anatase $TiO_2$, minor $Ru_xTi_{1-x}O_2$, trace brookite $TiO_2$ |
| TITB5 | 20:80 | 55 | 78 | 8 | anatase $TiO_2$, minor $Ru_xTi_{1-x}O_2$ |
| TITB6 | 0:100 | | 91 | | anatase $TiO_2$, minor rutile $TiO_2$, brookite $TiO_2$ |

Examination of PXD results shows that the sought-for single, rutile, ruthenium-titanium phase *was* formed in all mixed-metal samples, but only as a minor product. It is nonetheless interesting to see whether the presence of titania affects ruthenia crystallite sizes and vice versa. Results in the above table suggest a general increase in size of $TiO_2$ crystallites on increasing ruthenium content and a decrease in $RuO_2$ crystallite size on increasing titanium content.

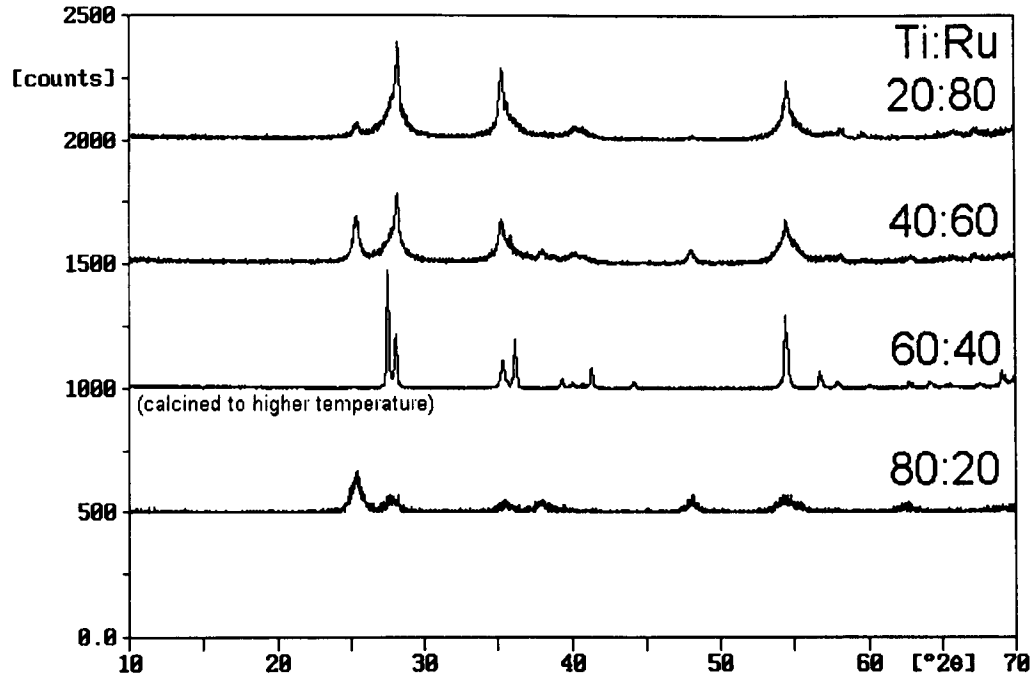


**Figure 4.5: PXD traces for samples calcined at 500°C for 5h, containing varying proportions of ruthenium and titanium oxide as indicated; the peaks are narrower, indicating the formation of larger particles during calcinations. The sample with Ti:Ru ratio of 60:40 was inadvertently calcined to a much higher temperature of ca. 1500°C, owing to a faulty thermostat. The visibly narrower peaks show that much smaller particles have formed. The different reflections present suggest that the required mixed phase was formed, albeit with larger particle sizes rendering it less useful.**

Figure 4.5 shows the diffractograms for samples TITB2-5 (i.e. those containing both ruthenium and titanium). (TITB2, 3 and 5 were calcined to 500°C for five hours whereas TITB4 was inadvertently calcined to ca. 1500°C for ca. 30 min, owing to a thermostat failure.)

Whilst the peaks have become narrower and more distinct, indicating the formation of larger particles, the positions of the reflections in the samples calcined at the lower temperature remain unchanged when compared with Figure 4.4. However, the completely different diffraction pattern for the

overheated TITB4 sample show a change of phase has taken place. The particle sizes of the calcined samples and the phases present are shown in Table 4.4.

**Table 4.4: particle sizes and phases present in samples calcined at 500°C for 5h (except *TITB4 that was heated to ca. 1200°C for 30 min).**

| | Ru:Ti ratio | Particle size /nm | | Phases present (detected by visual inspection) |
|---|---|---|---|---|
| | | ca. 28° ($RuO_2$ / rutile mixed phase) | ca. 48° ($TiO_2$ anatase) | |
| TITB2 | 80:20 | 339 | 96 | $RuO_2$, $TiO_2$ (anatase) |
| TITB3 | 60:40 | 309 | 169 | $RuO_2$, $TiO_2$ (anatase) |
| TITB4* | 40:60 | 450 | | $Ru_xTi_{1-x}O_2$ |
| TITB5 | 20:80 | | 158 | $RuO_2$, $TiO_2$ (anatase) |

**An increase in particle size compared to the uncalcined samples was observed, especially in TITB4. However, the formation of a mixed $Ru_xTi_{1-x}O_2$ phase was not observed, except in the more strongly heated TITB4 sample. Analysis was performed by PXD from experiments using precursors containing different proportions of ruthenium nitrosyl nitrate and titanium oxynitrate (as indicated). Particle sizes were calculated using the Scherrer equation.**

The reflections correspond to a rutile phase, with peak positions somewhere between $RuO_2$ and $TiO_2$. However, this phase change was accompanied by an increase in particle size to 450nm that would render the material considerably less catalytically active.

BET surface-area measurements showed a general increase in surface area, going from compositions of pure ruthenia to pure titania, from 15 $m^2g^{-1}$ to

80 $m^2g^{-1}$ (see Figure 4.6), as the ruthenium oxide particles formed were invariably smaller than those of titanium oxide.

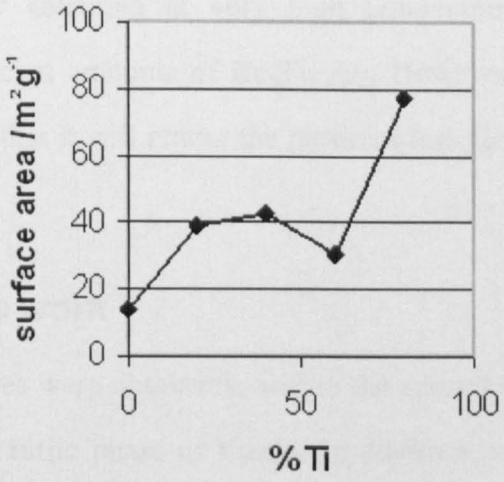


**Figure 4.6: a general increase in surface area was observed with increasing titanium content, as can be observed in this graph of BET surface area measurements, plotted against percentage titanium content, for samples containing varying proportions of titanium and ruthenium oxide**

The experiment involving VERTEC VEXP0424 (dissolved in diethylene glycol) and ruthenium acetate was not possible to run properly as the diethylene glycol formed a gelatinous complex with the ruthenium before it could be pumped into the reactor. Examination of the PXD results from all of the remaining experiments, as were tabulated in Table 4.2, showed that in all cases anatase, and not rutile, titania was present and (where ruthenium was present) a separate rutile $RuO_2$ phase was made.

## *Conclusions*

It was possible to decompose salts of both ruthenium and titanium to make oxide particles using the hydrothermal flow-synthesis technique. These particles were nanosized with high surface area; the $TiO_2$ particles consisted mainly of the anatase polymorph. Making rutile-phase $TiO_2$ or $Ru_xTi_{1-x}O_2$ as a major product seems not to be possible using the conditions and precursors

tried in this research. Calcining of the products at moderate temperatures does not allow the rutile mixed-metal phase to form from separate anatase-$TiO_2$ and $RuO_2$ phases. Only calcining at very high temperatures seems to allow formation of significant amounts of $Ru_xTi_{1-x}O_2$. However, this leads to such loss of surface area that it will render the particles less catalytically active and hence less useful.

## Possible future work

If higher temperatures were obtainable within the reactor, it might be possible to form the desired rutile phase of titania. In addition, an exhaustive test of different precursors was not carried out. If the stability to hydrothermal decomposition of ruthenium and titanium precursors could be matched, the formation of single-phase ruthenia-titania might become possible.

## References


[1] M. Gratzel, *J. Photochem. Photobiol. A-Chem.*, **2004**, *164*, 3.
[2] J. Akikusa, S. U. M. Khan, *Int. J. Hydrog. Energy*, **2002**, *27*, 863.
[3] W. Zhou, C. W. Sun, Z. Z. Yang, *J. Inorg. Mater.*, **1998**, *13*, 275.
[4] B. Kim, D. Kim, D. Cho, S. Cho, *Chemosphere*, **2003**, *52*, 277.
[5] F. Tiarks, T. Frechen, S. Kirsch, J. Leuninger, M. Melan, A. Pfau, F. Richter, B. Schuler, C. L. Zhao, *Macromol. Symp.*, **2002**, *187*, 739.
[6] T. E. Gamar, R. J. Stanaway, in *Industrial Minerals and Rocks*, 6th ed. (Ed.: D. D. Cain), Society for Mining, Metallurgy and Exploration inc., **1994**.
[7] W. L. Bragg, G. F. Claringbull, *Crystal Structures of Minerals, Vol. 4*, G. Bell and Sons Ltd, London, **1965**.
[8] J. F. Banfield, D. R. Veblen, *Am. Miner.*, **1992**, *77*, 545.
[9] F. Dachille, P. Y. Simons, R. Roy, *Am. Miner.*, **1968**, *53*, 1929.
[10] A. Cabanas, J. A. Darr, E. Lester, M. Poliakoff, *J. Mater. Chem.*, **2001**, *11*, 561.
[11] A. A. Galkin, B. G. Kostyuk, V. V. Lunin, M. Poliakoff, *Angew. Chem.-Int. Edit.*, **2000**, *39*, 2738.

# Chapter 5: cerium dioxide and cerium-zirconium mixed-oxide compounds

## *Summary*

Work by Cabañas et al. in Nottingham had revealed the possibility of making single-phase mixed-metal oxides such as $Ce_{1-x}Zr_xO_2$ nanoparticles. The compound was successfully made with different ratios of cerium to zirconium, over a wide range of $x$. Experiments were carried out under different conditions in order to investigate the possibility of controlling particle size.

Firstly, an efficient method of separating the suspended particles from the raw product was developed. Addition of a small amount of acid turned out to be a simple and effective way of causing the particles to settle out of suspension, and much more practical than filtration.

Initial experiments at different flow rates revealed no significant effect of flow rate upon particle size. Use of different precursor concentrations also failed to show any effect on particle size.

However, it was observed that an increase in temperature led to a marked increase in particle size, as well as in reaction yield.

Temperature-programmed reduction experiments were attempted, and showed that catalytic activity occurred at a rather higher temperature than that of commercially-available ceria-zirconia compounds.

# *Introduction*

## Catalytic converters

One of the most important areas of catalyst research, both economically and environmentally, is automotive catalytic converters[1]. In the USA, the Clean-Air Act of 1970 was one of the main driving forces towards finding ways to reduce the amount of polluting gases from cars. Gradually, catalytic silencers were introduced into American car exhausts. By 1979, converters using "three-way catalysts" (TWCs) were available. Nowadays, legislation enforcing the use of catalytic converters is in place in Japan, the UK and Europe, and in South America. TWCs are so called because they accelerate reactions that destroy the following three classes of pollutant:

| | | | |
|---|---|---|---|
| Carbon monoxide | CO | } | Reducing pollutants |
| Unburned hydrocarbons | $C_xH_y$ | | |
| Nitrogen Oxides | $NO_x$ | | Oxidising pollutant |

These pollutants can react to form relatively harmless products by the following reactions, which include both reductions and oxidations:

| | |
|---|---|
| Oxidation: | $2CO + O_2 \rightarrow CO_2$<br>$C_xH_y + (x + x/4)O_2 \rightarrow xCO_2 + y/2H_2O$ |
| Reduction | $2CO + 2NO \rightarrow 2CO_2 + N_2$<br>$C_xH_y + (2x+x/2)NO \rightarrow xCO_2 + y/2H_2O + (x+y/4)N_2$ |

The main catalytic species in a converter are rhodium and platinum and/or palladium (known as noble metals). Typically, there are 1-2 g of platinum and 0.2-0.3 g of rhodium in any one converter.

The three-dimensional structure of a TWC consists of a honeycomb-like lattice designed to maximise the surface area available to the pollutants for reaction. The structure is maintained by a ceramic support, which is coated with a thin, porous layer of chemicals, or "washcoat". The mixture is predominantly alumina (70-80%) and the remainder is made up of other metal oxides, each serving a different purpose. Cerium dioxide (also known as ceria), or sometimes another *f*-block metal oxide, is added to the washcoat to store oxygen, as will be discussed below. A Group 2 metal oxide, such as barium oxide, may also be used to sequester any leftover oxygen. Only a small percentage of the washcoat consists of noble metals. Platinum and palladium catalyse the oxidation reactions within the converter, whilst rhodium catalyses the reduction reactions.

## Uses for ceria / ceria-zirconia mixed oxide

### Catalytic converters

Since the early 1980s, ceria has become widely used in automotive catalytic converters and, as such, has become the most important application of rare-earth oxides today[2]. TWCs used in the late 1980s mostly contained rhodium and platinum as active noble metals, and also incorporated ceria. The ceria has been suggested to serve several different purposes[3]:

- To promote the noble metal dispersion
- To increase the thermal stability of the alumina support
- To promote the water gas shift and steam reforming reactions:

Water gas shift reaction: $CO + H_2O \rightarrow CO_2 + H_2$

Steam reforming reaction: $C_xH_y + 2xH_2O \rightarrow xCO_2 + (2x + y/2)H_2$

- To favour catalytic activity at the interfacial metal-support sites
- To promote carbon monoxide removal through oxidation employing lattice oxygen
- To store and release oxygen under lean or rich conditions according to the following reactions:

Oxygen release: $xCO + CeO_2 \rightarrow xCO_2 + CeO_{2-x}$

Oxygen storage: $x/2O_2 + CeO_{2-x} \rightarrow CeO_2$

All of these aspects exploit the ability of systems incorporating noble metals and ceria to promote migration and exchange of oxygen, and this last aspect, of storing and releasing oxygen, appears to be the most important. The highest conversion of pollutants to less harmful products is achieved when they pass through the converter with a stoichiometric amount of oxygen. Fuel-rich or fuel-poor air-to-fuel ratios greatly decrease the efficiency of TWCs. The air-to-fuel ratio significantly oscillates around the optimum value and could therefore present a serious limitation for a TWC system.

Addition of ceria to the catalyst means that it can operate over a range of air-to-fuel ratios because it acts as an oxygen buffer. It can store and release oxygen thanks to the $Ce^{4+}/Ce^{3+}$ couple. With a higher Oxygen Storage Capacity (OSC), a catalyst will have a higher conversion efficiency and higher resistance to thermal ageing. The presence of the noble metal actually promotes the reduction of surface oxygen, a phenomenon that has been attributed to the ability of the noble metal to "spill" the reducing species over the cerium support.

New restrictions on automotive emissions have set new challenges to the developers of TWC systems[4]. A major problem with TWCs is that they only

function efficiently at high temperatures (above ca. 300°C). Therefore, during the cold start of an engine, pollutant emissions, particularly those of unburned hydrocarbons, are high until the required temperature is reached. If this cold start is incorporated into the tests, and the emission limits are set very low, development of "close-couple" catalysts will be required. These catalysts operate at above 1000°C because they are mounted on the exhaust manifold, and hence need to be stable at these temperatures. As soon as any thermal sintering occurs, both OSC and metal-support interactions are inhibited.

It has been found that a proportion of zirconium dioxide (zirconia) in solid solution with ceria, promotes the thermal stability of the surface area of the catalyst and the efficiency of OSC[5] (allowing the surface to be reduced at a lower temperature). Some experiments showed that the surface area stability was increased by greater zirconia content up to about 60% molar[6], and that OSC was also increased up to about 40% zirconia, as displayed in Figure 5.1.

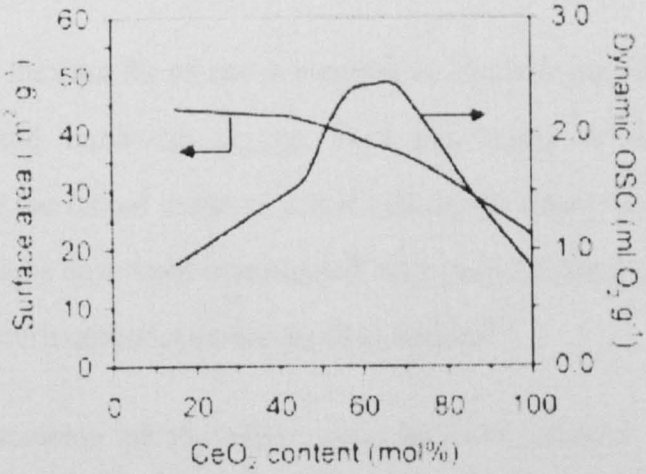


**Figure 5.1: Thermal stability and OSC at 673 K of ceria-zirconia mixed oxides after ageing at 1173 K for 6 h in air atmosphere, showing how thermal stability decreases on decreasing zirconium content, and how OSC is greatest at ca. 60% cerium content[6].**

In the mid-1990s, "fourth-generation" TWCs utilised this mixture, but industrial researchers only revealed the formulation at a 1997 "Catalyst and automotive pollution control" (CaPOC) symposium in Brussels[7].

## Other uses for ceria-zirconia catalysts

Yttrium-Stabilized Zirconia (YSZ) compounds are used in the developing technology of Solid-Oxide Fuel Cells (SOFC). Here, we give a very brief description, based upon a review[8], which should be consulted for further details. In these cells, hydrogen gas is reacted with air to form water, whilst producing an electrical current. It is hoped that such cells will become a viable source of electricity in the future, possibly as a less environmentally damaging source of power for cars. The YSZ mixed-oxide constitutes the anode of the cell; $O^{2-}$ ions within the lattice react with the hydrogen fuel to produce water, two electrons and an oxygen vacancy ($V_{\ddot{O},YSZ}$) in the lattice:

$$H_2 + O^{2-}{}_{YSZ} \rightarrow H_2O + 2e + V_{\ddot{O},YSZ}$$

Therefore, as is the case for its use in automotive catalytic converters, the ease of removing and replacing oxygen from the lattice is crucial to the effectiveness of the mixed oxide as a fuel cell anode. Many different mixed-oxide combinations have been investigated, and considerable interest has been shown in using ceria-zirconia oxides for this purpose[9].

For further discussion of the other uses for ceria-zirconia nanoparticles, including their use as gas sensors, chromatographic materials and in cosmetics, there is an excellent review by di Monte and Kašpar on the subject[10].

## The nature of ceria-zirconia solid solutions

Ceria has a fluorite structure (see Figure 5.2a). The similar radii of $Ce^{4+}$ and $Ce^{3+}$ ions enable the substitution of one for the other within the lattice, which leads to the possibility of oxygen storage.

At room temperature, the stable form of $ZrO_2$ is the monoclinic phase. The tetragonal phase is obtained at temperatures above 1170°C and the cubic phase is normally only stable at very high temperatures (2370°C) (Figure 5.2b-c). Alternatively, the cubic phase may be stabilised by the presence of another cation, such as $Ce^{4+}$, in the lattice.

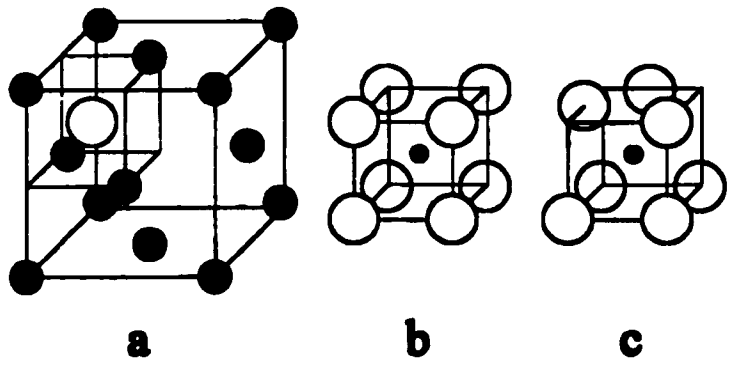


**Figure 5.2: ○ $O^{2-}$, ● $Ce^{4+}$ • $Zr^{4+}$**

**(a) the structure of fluorite $CeO_2$; (b) coordination environment for tetragonal and cubic zirconia (8-coordinate zirconium); (c) coordination environment for monoclinic zirconia (7-coordinate zirconium) (diagrams reproduced from Trovarelli[11])**

Solid solutions of ceria and zirconia form with a single cubic phase, as seen in Figure 5.3. Cerium and zirconium ions are randomly distributed in the lattice, and substitution of zirconium for cerium ions leads to a shrinking of the lattice.

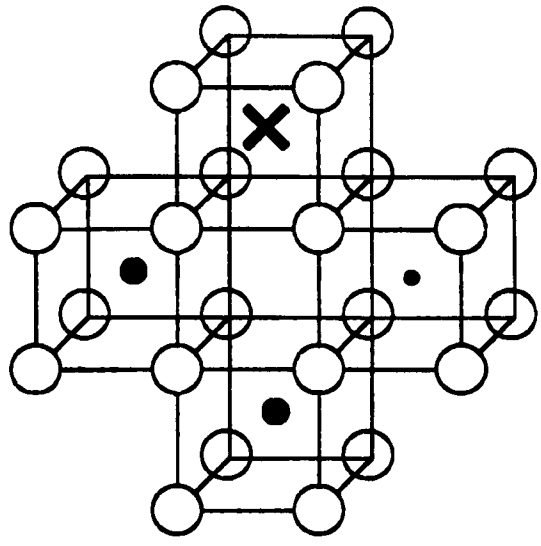

**Figure 5.3: a possible structure for a pure $Ce_{0.6}Zr_{0.4}O_2$ solid solution, where O $O^{2-}$, ● $Ce^{4+}$ • $Zr^{4+}$, × lattice vacancy (diagram reproduced from Trovarelli[11])**

A phase diagram for ceria-zirconia systems at different temperatures and with different Ce:Zr ratios is shown in Figure 5.4.

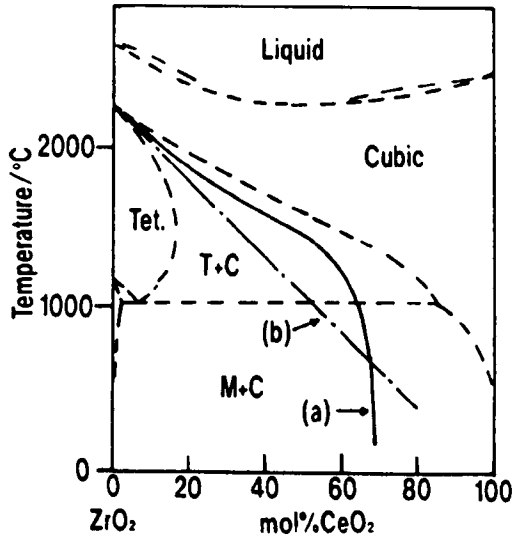


**Figure 5.4: Stable-metastable phase diagram in the $ZrO_2$-$CeO_2$ system. (b) represents the equilibrium temperature between cubic and tetragonal phases calculated based on a simple regular-solution model whilst (a) represents the tetragonal-to-cubic transition temperature determined experimentally (reproduced from Yashima and Yoshimura[12])**

## Previous synthesis of ceria-zirconia oxides

### Non-hydrothermal and batch hydrothermal syntheses

Ceria-zirconia compounds have, in the past been made using various methods, such as high-temperature solid-state syntheses[13, 14], high-energy ball milling[15], sol-gel[13, 16] or microemulsion[17] methods, and co-precipitation followed by ageing[18]. However, these techniques suffer from several difficulties. Some require long reaction times (involving multi-step syntheses or aging), many involve very high temperatures and are therefore energy intensive, and many require organic liquids that are damaging to the environment. In addition, when nano-scale particles are required, the complexity and cost of their production becomes even higher.

The use of hydrothermal processes, operating at the relatively low temperatures (up to ca. 400°C), would seem to overcome most of these problems. Batch hydrothermal techniques have already been used by, for example, Hirano and Kato[19], who reacted cerium (III) nitrate with zirconium oxychloride at 180°C. However, they only achieved a single-phase solid solution with reaction mixtures containing low proportions of cerium, and reaction times of several hours were required.

As will be seen, the use of a flow system for hydrothermal reactions allows fast, low-temperature syntheses, using only water as solvent, which overcomes all of the disadvantages of other methods mentioned above.

### The Arai-Adschiri group

The group of Arai and Adschiri from Tohoku University in Japan were the first to attempt the hydrothermal formation of cerium dioxide in a flow reactor[20]. During their work, cerium (III) nitrate was reacted in a rig similar to Rig 1 used in this Thesis. The reaction was performed at temperatures in the range

250-400°C and with residence times of ca. 1 s. At 250°C, conversions of up to 30% and particle size of ca. 200 nm were achieved. Conversion was almost 100% at supercritical temperatures, and particle sizes were also much smaller (ca. 20 nm). The high reaction rate was attributed to the high rate of hydrolysis and the low solvent power of supercritical water causing a high degree of supersaturation, and leading to rapid particle nucleation.

In addition, the Arai-Adschiri group has experimented with making mixed oxides of titanium and zirconium; $Ti_{0.99}Zr_{0.01}O_2$ was prepared, using zirconium acetate as the zirconium source.

Discussion of further techniques for the synthesis of ceria-zirconia nanoparticles may be found, along with a great deal of other information about the compounds, in the excellent review by di Monte and Kašpar[10].

## Previous work in Nottingham

Arai's work on ceria and zirconia production was developed further in Nottingham for the synthesis of single-phase mixed oxides of cerium and zirconium[21, 22]. A solution of cerium ammonium nitrate and zirconium acetate was reacted in Rig 1, with the metal-salt and water flows meeting at a simple T-piece. Near-critical conditions of 300°C and 25 MPa, and varying proportions of cerium and zirconium precursors were used, to form solid solutions of $Ce_{1-x}Zr_xO_2$ with $x = 0.2$-$0.9$. Large surface areas (60-180$m^2$) and correspondingly small particle sizes (7-3.5nm) were observed from BET and PXD techniques respectively. These results were attributed to rapid precipitation and low reaction temperature.

When $x \leq 0.5$ (i.e. for materials containing smaller proportions of zirconium), PXD patterns corresponded to a cubic fluorite structure. An increase in zirconium content causes a decrease in the lattice parameter owing to the small

size of the zirconium ions in comparison to the cerium ions. For $x = 0.8$-$0.9$, a tetragonal phase was assigned and, for pure zirconia, there was a mixture of monoclinic and tetragonal $ZrO_2$ phases.

## *Objectives of the research to be described here*

1. **to achieve an effective way of separating ceria-zirconia nanoparticles from the raw reaction product.** The raw product consists of a suspension of metal-oxide particles and a solution of unreacted metal-salt precursors. Several different separation methods would be attempted and the samples thus obtained would then be analysed by PXD.

2. **to test the reproducibility of the rig.** Experiments would be run several times at the same conditions and the results compared by BET surface-area measurements, in the hope of achieving consistent results.

3. **to investigate the effects of changing temperature, flow-rate and concentration on the product particle size.** A range of reaction conditions were to be used, and the particles produced analysed by PXD. Results were compared with the predictions of the effect of reaction conditions upon particle size that were made in Chapter 1.

4. **to investigate the catalytic activity of the ceria-zirconia products.** Temperature-programmed oxidation would be used to test the compounds made in a real-life situation.

5. **to attempt the formation of iron-cerium single-phase mixed oxides.** A mixture of dissolved iron and cerium salts would be reacted in the hydrothermal flow reactor and the products formed analysed by PXD.

## *Results and Discussion*

### Particle separation

In Chapter 3, centrifugation followed by decantation was found to be an effective means of separating copper oxide particles from the crude reactor product. It was therefore attempted to use this method for the separation of ceria-zirconia particles. However, even after centrifuging for long periods (4 h at 4000 rpm), very few particles had settled to the bottom, and the liquid remained milky. In addition, the acidic and oxidising effects of the cerium ammonium nitrate precursor were causing the aluminium centrifuge canisters to corrode. It therefore became clear that a new method of separation was required. Several alternative methods were therefore tried: rotary evaporation, membrane filtration, manually removing crystals of precursor, using ion-exchange resin and finally acidification followed by decantation. The resulting powders were analysed for impurities by PXD, producing diffractograms as shown in Figure 5.5. Acidification followed by decantation proved to be not only very convenient but also a very effective method of purification.

### Sample preparation

Crude 200 $cm^3$ samples of product were subjected to the different means of purification. These samples had been prepared in Rig 1 from 0.2 M solutions of cerium ammonium nitrate and zirconium oxynitrate in equal proportions, operating at a mixing-point temperature 300°C and 250 bar. Flow rates were 10 ml $min^{-1}$ for the water feed and 5 ml $min^{-1}$ for the metal-salt feed. The product samples were pale yellow and opaque, because the nanoparticles had remained in suspension.

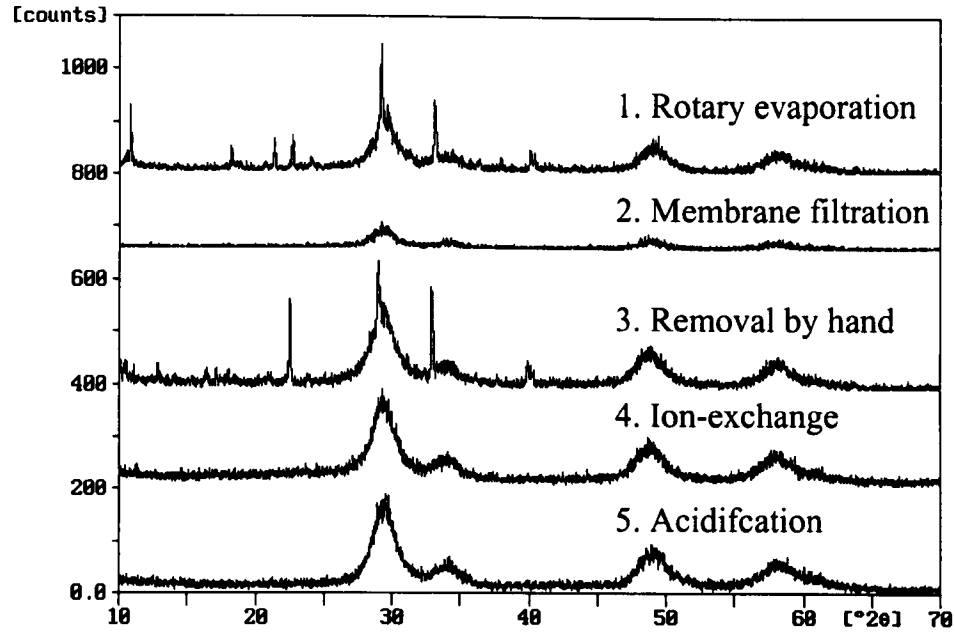


**Figure 5.5: PXD results from samples purified by the different means described below, showing that the membrane filtration, ion-exchange and acidification methods all allow good purification of ceria-zirconia nanoparticles. This can be seen because, in contrast to the other PXD traces, there are only broad peaks from the mixed-oxide nanoparticles and no sharp spikes – attributable to large crystals of precursor salts. Acidification (followed by decantation) was eventually chosen to be the best method, as it was simple, cheap and effective.**

## 1. Rotary evaporation

The first method attempted was to remove most of the water from the reaction product on a rotary evaporator. The resulting concentrated suspension was then poured into an evaporating basin and placed in an oven at ca. 80°C and left overnight to allow the remaining water to evaporate. The residue consisted of pale-yellow powder collecting around the edge of the basin and bright orange crystals of ammonium cerium nitrate, which collected in the centre of the basin. All of this solid material was collected for PXD analysis. As can be observed from Figure 5.5, there were several sharp spikes among the broader peaks (from $CeO_2$ nanoparticles) in the diffractogram. These narrow peaks

were caused by large crystals of precursor that crystallised out of solution in the oven.

## 2. Membrane filtration followed by oven-drying

The second method was to use a membrane filter with suction to collect the small oxide particles. The membrane filter consisted of a thin layer of micro-porous plastic that would allow only water and water-soluble precursors to pass. However, the filter quickly became clogged, so the method was adapted slightly to become more practical. The product was evaporated using the rotary evaporator followed by the oven, as in Method 1 above. The dry particles were then placed in the filter (with suction) and water added dropwise until the orange cerium ammonium crystals were seen to have been dissolved and to have passed through the filter. The remaining pale-yellow powder was collected for PXD analysis. As can be observed from Figure 5.5, the diffractogram of this sample still exhibited many of the same narrow peaks as the sample from Method 1, which was unpurified apart from evaporating the water.

## 3. Drying, followed by removal by hand of precursor

After drying the unpurified sample from Method 1 in an evaporating basin, it was observed that a pale-yellow powder was deposited around the edge of the basin whilst large, bright-orange crystals were deposited in the centre. This is because the precursor materials are very soluble and will therefore remain in solution until almost all of the liquid is evaporated. The nanoparticles that were originally in suspension will be deposited much earlier as the suspension is not stable when there is a higher concentration of dissolved salt present.

It was therefore thought possible to obtain a purer product by simply discarding these crystals from the centre of the dish, which would contain the

majority of the precursors. The paler crystals were then collected from the edge. This process is illustrated in Figure 5.6.

When the pale-yellow crystals were analysed by PXD (see Figure 5.5), the diffractogram was seen to contain many of the same sharp peaks as the unpurified sample, showing that significant amounts of precursor were remaining in the supposedly purified product. It was therefore concluded that this method was unsuitable for purification.

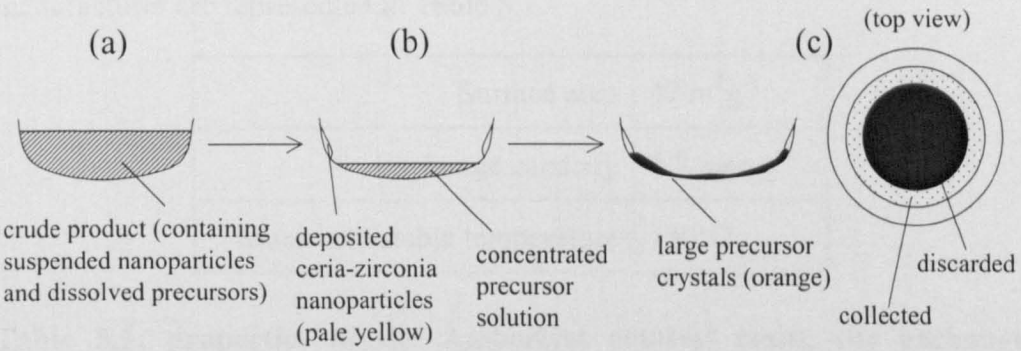


**Figure 5.6: A proposed method for separating ceria-zirconia nanoparticles from unwanted precursor. (a) The raw reactor product, containing dissolved precursors and suspended nanoparticles, is placed in the oven to dry. (b) As some water evaporates, the suspension of nanoparticles is no longer stable and so the particles are deposited on the side of the basin. This leaves a concentrated solution of precursors in the bottom of the dish. (c) The water is evaporated from this concentrated solution, allowing the precursors to slowly crystallise. Large precursor crystals are left behind (the ammonium cerium nitrate precursor is bright orange, giving an intense colour to these crystals). A view from above the basin is also presented, showing that the pale-coloured particles are collected from around the edge of the basin, whilst the large, brightly coloured crystals from the centre are discarded.**

## 4. Ion exchange resin

The fourth method was to attempt to replace the metal ions dissolved in the water with $H^+$ ions, using an ion-exchange resin, leaving only ammonium nitrate and nitric acid in solution. Ion-exchange resins can then be regenerated by washing in acid.

Amberlyst resin was chosen as it was inexpensive and was already in use as an acid catalyst within the research group. The data provided by the catalyst manufacturer are represented in Table 5.1.

| | |
|---|---|
| Surface area | 47 $m^2g^{-1}$ |
| Exchange capacity | 4.7 meq $g^{-1}$ |
| Maximum stable temperature | 130°C |

**Table 5.1: properties of the Amberlyst catalyst resin; the exchange capacity is required for the calculation of the required amount to be used in these separation experiments.**

The mass of resin required can be calculated using Equation 5.1 below, adding an arbitrary 20% excess. There then follows the calculation for amount of $H^+$ required.

$$\text{Proportion of excess} \times \frac{\text{Amount of } H^+ \text{ required}}{\text{Exchange capacity}} = \textbf{Mass of resin required}$$

$$\frac{120\%}{100\%} \times \frac{0.067 \text{ mol}}{0.0047 \text{ eq } g^{-1}} = \textbf{17 g}$$

**Equation 5.1: calculating the mass of ion-exchange resin required; the amount of H+ required is calculated below.**

To calculate the amount of $H^+$ needed, the following balanced reaction equation was examined, where $x$ is the amount of zirconium present, divided by the total amount of cerium and zirconium present.

$$(1\text{-}x)[NH_4]_2Ce(NO_3)_6 + xZrO(NO_3)_2 + (2\text{-}x)H_2O \longrightarrow Ce_{1\text{-}x}Zr_xO_2 + (4\text{-}2x)HNO_3 + (2\text{-}2x)NH_4NO_3$$

We assume that all species are both ionic and water soluble except for the metal oxide (which is an insoluble solid) and water itself. It can be calculated that, amongst these soluble, ionic precursors, 6-2$x$ positive charges (and the same number of negative charges) are present. Amongst the products there are 6-4$x$ positive charges (and, again, the same number of negative charges). Therefore, the ion-exchange resin would have to provide more $H^+$ ions if no conversion took place than if complete conversion occurred. Therefore, a zero-conversion situation will be considered.

In this case, $x = 0.5$, so the unreacted precursors would require 5 equivalents of $H^+$ per equivalent of metal ion. The original concentration of the precursors (in terms of total metal-ion concentration) is 0.2 mol $dm^{-3}$ but this would be diluted to one third of its original concentration in the rig. 200 $cm^3$ of product stream is collected for each sample so the maximum quantity of $H^+$ ions that could be required, in the extreme case of zero conversion, is expressed in Equation 5.2.

| feed concentration | × | volume of product collected | × | dilution factor | × | equivalents of $H^+$ required | = | **amount of $H^+$ required** |
|---|---|---|---|---|---|---|---|---|
| 0.2 mol $dm^{-3}$ | × | 0.2 $dm^{-3}$ | × | 1/3 | × | 5 | = | **0.067 mol** |

**Equation 5.2: calculation of amount of $H^+$ ions required for a specific ceria-zirconia synthesis reaction**

One sample was stirred with the 17 g of Amberlyst beads, the required mass, as calculated in Equation 5.1. Initially, a crackling noise was heard, which subsided after ca. 10 min. Attempts at separating the beads from the remaining material using filter paper proved unsuccessful owing to the rapid clogging of the paper. The beads were therefore separated from the liquid and particles using the coarse wire mesh from the membrane filtration assembly used in Method 2 above. As much of the solid oxide material as possible was washed from the beads through the mesh, using deionised water. This filtrate was then placed in a measuring cylinder.

Unexpectedly, the particles were observed to have settled from suspension. The supernatant liquid was removed by pipette and the remaining particles were dried overnight in an oven at ca. 80°C and submitted to PXD analysis.

The diffractogram, as shown in Figure 5.5, showed only broad peaks caused by the expected ceria-zirconia mixed oxide nanoparticles; no sharp peaks corresponding to large precursor crystals were observed. It was therefore concluded that this method would be a possible satisfactory method for purification.

It was attempted to regenerate the Amberlyst resin by soaking in 0.5 mol $dm^{-3}$ HCl. However, the supposedly-regenerated resin was no longer effective: the crackling noise that was heard when using fresh beads did not happen, and the nanoparticles did not settle out of suspension. The method of regeneration described by Malshe et al.[23] suggested washing the used beads in 5% NaOH solution followed by 5% HCl. However, these beads were no more effective than those that had been washed in acid alone. It was therefore necessary to use fresh resin for each product sample.

Ion-exchange resin was used to purify the product from several experiments (as indicated within their separate sections), but once the addition of acid

(Method 5 below) was found to have a similar effect, it was used form then on, to avoid unnecessary waste of resin.

## 5. Addition of acid then decantation (the best method tested)

The unexpected settling of particles in Method 4 led to the most effective method of purification. It was thought possible that the same effect caused by exchange of metal ions for $H^+$ could be achieved by simply adding $H^+$ in the form of concentrated acid. However, adding acid might lead to the addition of yet another impurity into the product. This problem is largely avoided by using nitric acid, which is merely the acid of the nitrate ions that were already present from the precursors.

10 $cm^3$ of concentrated nitric acid was added to a 200 $cm^3$ sample of crude reactor product, and the mixture was briefly stirred with a glass rod to allow mixing. After leaving overnight, the particles had settled out of suspension as had been hoped, leaving a clear supernatant liquid.

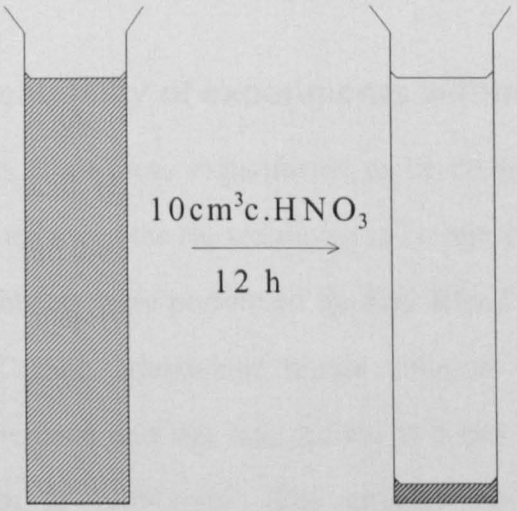


**Figure 5.7: addition of concentrated nitric acid causes ceria-zirconia nanoparticles to settle out of suspension overnight, as shown in the above diagram, which shows the product before and after settling.**

This clear liquid was removed by pipette, being careful not to disturb the settled particles; the remaining sediment was then dried in the oven at ca. 80°C. The resulting dry powder was analysed by PXD.

The diffractogram showed only broad peaks from ceria-zirconia and no sharp peaks from leftover precursors. Owing to the straightforward, cheap and effective nature of this purification process, it was decided to use this in future experiments.

As part of the reason behind using the hydrothermal method is that it avoids the use of harmful chemicals (bases, and volatile organic compounds), it is perhaps a pity that the chosen separation technique involves the use of concentrated acid. Future work might involve finding the absolute minimum amount of acid required for particle settling. Also, it might be useful to investigate whether simply increasing the ionic concentration of the suspension by the addition of a salt, less harmful than nitric acid, would have the same effect.

## Proving the repeatability of experiments within the rig

For any conclusions from these experiments to be credible, it is vital that experiments performed using the rig are shown to be repeatable. With this aim in mind, five experiments were performed by Paul Blood on Rig 2 using the same conditions. Cerium ammonium nitrate solution with concentration 0.1 mol $dm^{-3}$ was prepared and run into the rig at a rate of 5 ml $min^{-1}$, with water being run in at 10 ml $min^{-1}$. The mixing point temperature was maintained at 300°C, and the pressure at 250 bar.

The product suspension was acidified to allow the $CeO_2$ particles to settle, and the particles were then allowed to dry overnight in an oven at ca. 80°C. An alternative method to PXD was used to analyse the particles.

$$\frac{V}{V_{mon}} = \frac{cz}{(1-z)(1-(1-c)z)} \quad \text{where } z = \frac{p}{p^*}$$

**Equation 5.3:** The BET isotherm, where
$p$ = pressure above sample
$p^*$ = vapour pressure above a layer of adsorbate, resembling a bulk liquid
$V$ = volume of gas adsorbed
$V_{mon}$ = volume of gas in one monolayer
$c$ = constant (large, when enthalpy of desorption from monolayer is large compared with enthalpy of vaporization of liquid adsorbate)

Adsorption of nitrogen gas, and analysis using the BET isotherm, according to Equation 5.3, was used to acquire the surface area per unit mass of the products. The BET isotherm is a model for the adsorption of gas upon a surface: in this model, adsorption is considered to continue beyond one monolayer.

By exposing a sample in a vacuum chamber to varying amounts of nitrogen gas, and measuring the pressure above the sample, it is possible to obtain a value for $V$, the volume of nitrogen gas adsorbed. As the area occupied by one $N_2$ molecule is already known, the surface area of the sample can be calculated (and divided by the known mass to obtain a "specific" value for the material). Furthermore, if the density of the material is known, an estimate for the particle size can be found by assuming uniform spherical particles using the formula $d = 6 / \rho A_m$ where $d$ is particle diameter, $\rho$ is material density and $A_m$ is the surface area per unit mass.

The results from the five repeatability experiments are presented in Figure 5.8. It can be seen from the Figure that the points are centred on a mean of 95 $m^2 g^{-1}$ with a spread of $\pm$ 5 $m^2 g^{-1}$. This constitutes an error in surface area of ca. 5%. The surface area is proportional to the square root of the particle radius and so the error in the radius can be estimated to be $\pm(\sqrt{5})\% \approx \pm$ **2%**. This lends credibility to the results obtained in Rig 2 and allows the continuation of experiments with the expectation of meaningful results.

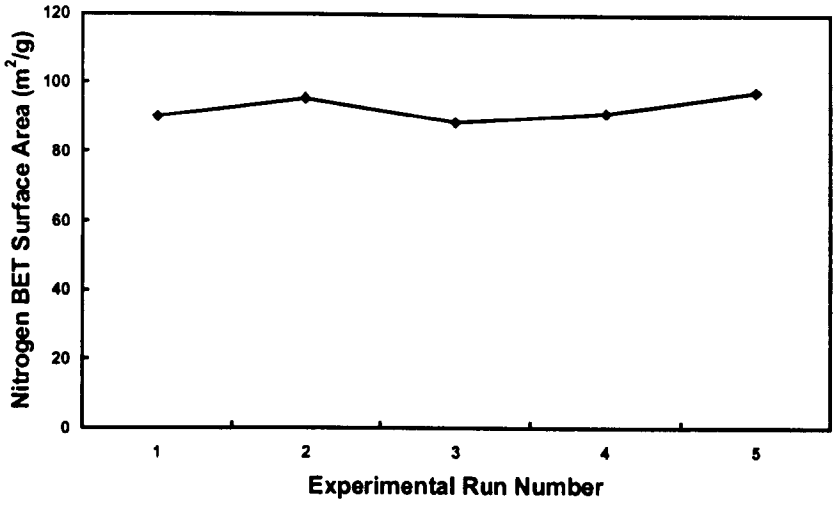


**Figure 5.8: comparison of the surface area (per unit mass) of products made in Rig 2 at the same nominal conditions shows a good agreement between samples.**

## Characterisation of mixed-oxide samples with differing Ce:Zr ratios

At Nottingham, the characterisation methods that are available for regular use are limited to PXD, BET and TEM (transmission electron microscopy), with PXD being the only method practical for frequent use. Through collaboration with Johnson Matthey, the many characterisation techniques available at their Research Centre at Sonning Common were made available.

A week of using this equipment provided a unique opportunity for the extensive use of several techniques: temperature-programmed reduction (TPR) for the assessment of catalytic activity; surface-area measurement using adsorption of nitrogen and the BET model; dynamic light scattering (DLS) for measuring the size of particles whilst still in suspension; testing whether the particles are compatible with some common catalytic substrates.

Since time was limited, we decided to focus upon the characterisation of ceria-zirconia compounds of different compositions, because these were the most

likely to give interesting, and different results. The help of Dr. Janet Fisher and Dr. Dave Thompsett from Johnson Matthey in this characterisation work is gratefully acknowledged.

## Sample preparation

Oxide powders containing different proportions of cerium and zirconium were produced for analysis using Rig 1, which used a simple T-piece for mixing as opposed to the new nozzle.

Solutions of cerium ammonium nitrate and zirconium nitrate were prepared with Ce:Zr ratios of 100:0, 80:20, 60:40; 50:50 40:60; 20:80; 0:100, with a total metal-ion concentration of 0.2 mol $dm^{-3}$. Large (ca. 10 g) samples of $Ce_{1-x}Zr_xO_2$ (with $x$ = 0, 0.2, 0.4, 0.6, 0.6, 0.8, 1) were then made in the rig. The reaction was carried out with a mixing-point temperature of 300°C and a pressure of ca. 250 bar. A sample of particle suspension was set aside. To the remaining suspension was added ca. 20 $cm^3$ of concentrated nitric acid in order to settle the particles; the supernatant liquid was then removed by siphoning and the remaining material was dried in an oven at 80°C. The samples were fired for 4 h at 500°C.

A portion of each of these samples was then palladated by 1%. As discussed above, ceria-zirconia compounds are used in automotive catalysts as an oxygen-storage component, in conjunction with small amounts of precious metal, usually rhodium and/or platinum. For TPR analysis, it is interesting to test the properties of both the untreated ceria-zirconia compound and the compound mixed with a precious metal, to better judge its potential performance in a real-life situation.

Palladation was performed by the incipient wetness method: the particles were soaked in aqueous palladium chloride solution for several hours. The samples were then dried in an oven at ca. 80°C and then fired at 500°C for a further 4 h.

## Temperature programmed reduction (TPR) analysis

TPR analysis can provide information on the catalytic activity of the particles. As the ceria-zirconia compound is used as an oxygen-storage component in catalytic systems, its ability to react with hydrogen gas is a useful gauge of its activity. In the TPR process, a gas-flow containing 5% $H_2$ gas (the remainder consisting of $N_2$) is passed continuously over the sample. The catalyst sample is then heated linearly to ca. 1000°C. Some of the hydrogen will react with the oxygen in the catalyst to form water (i.e. the catalyst is reduced). A thermal-conductivity detector measures the concentration of $H_2$ gas remaining in the flow after this reaction. Plotting conductivity against temperature provides a characteristic "fingerprint" of a sample. The peaks on the trace can then be integrated to provide a value for the amount of $H_2$ reacted per unit mass.

All palladated and non-palladated samples were analysed by temperature-programmed reduction (TPR) (up to 900°C).

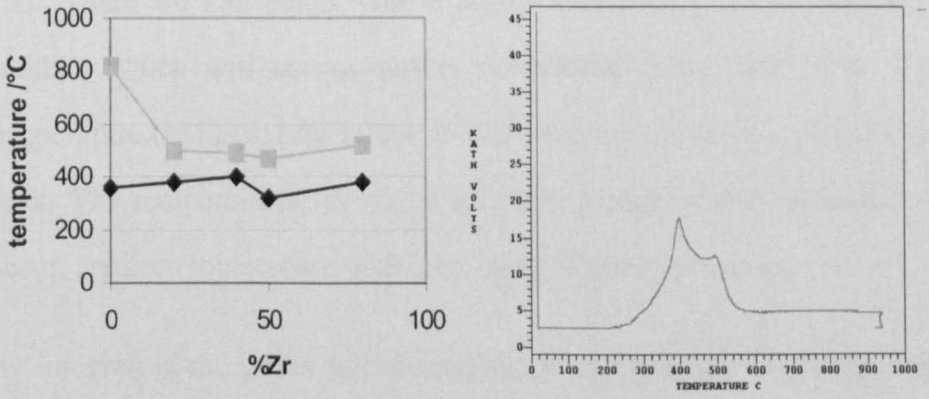


**Figure 5.9: the temperature at which the two observed peaks – low-temperature (LT, ◆) and high temperature (HT, ■) - occur in the TPR trace, and an example of the typical TPR trace observed for non-palladated samples.**

The typical form of the TPR trace for a non-palladated sample is shown in Figure 5.9, with two overlapping peaks. The position of the maxima of these peaks is plotted against percentage zirconia. It appears that the addition of any zirconia to ceria causes a movement of the high temperature (HT) peak to lower temperatures, but further addition of zirconia does not affect this peak. The effect on the low temperature (LT) peak appears to be insignificant.

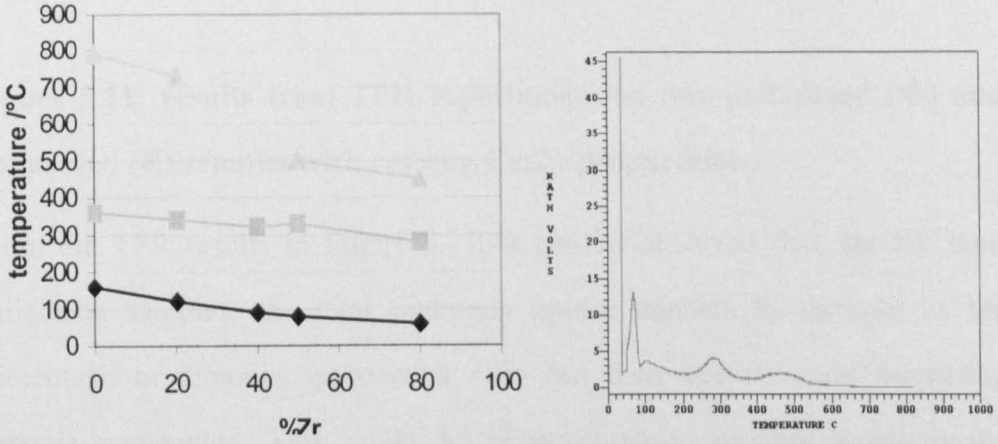


**Figure 5.10 – graph showing the position of the three peaks – at high temperature (HT, ▲), medium temperature (MT, ■) and low temperature (LT, ◆) - observed in the TPR traces for palladated samples.**

The typical form of the TPR trace for palladated samples is shown in Figure 5.10. There are four peaks. One is at low temperature (LT), overlapping with another, which will not be further considered here. Then come a medium temperature (MT) (except in the 40%Zr sample) and a high temperature (HT) peak. The temperatures, at which all three peaks for the palladated samples occur, are seen to decrease with increasing zirconium content.

By integrating the peaks in the samples, it was possible to obtain a value for the amount of hydrogen that reacted per gram of sample.

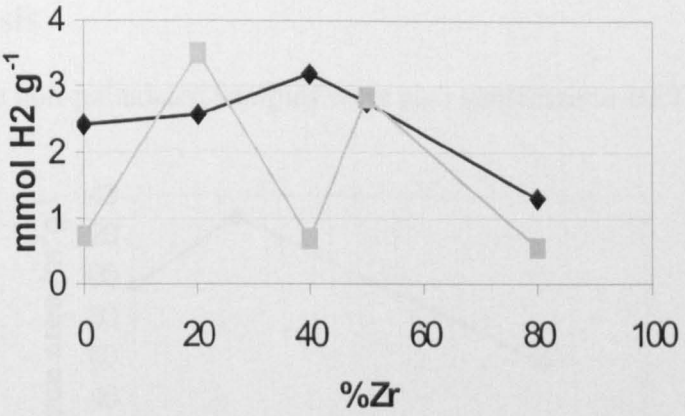


**Figure 5.11: results from TPR experiments on non-palladated (◆) and palladated (■) samples with varying Ce:Zr proportions.**

From the TPR results in Figure 5.11, it can be observed that, for the non-palladated samples, the total hydrogen uptake appears to increase as the percentage of zirconia approached 40% but then decreases on increasing zirconia percentage. This might be expected since zirconia increases the accessibility of the oxygen in the oxide, but also decreases the amount of oxygen available to react. The hydrogen uptake for the palladated samples seems to bear little relationship to the zirconia content, but this may be due to inconsistencies in the palladating process between samples.

Further interpretation of the TPR results was possible following BET analysis (see below).

## BET analysis

Several of the non-palladated samples were also subjected to BET analysis.

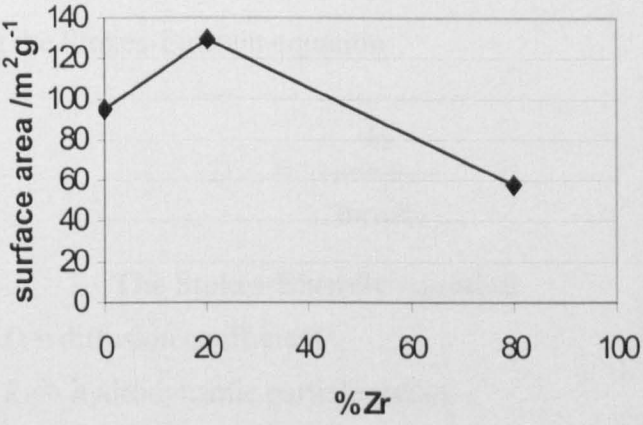


**Figure 5.12: BET results showing the high surface areas attainable with ceria-zirconia compounds with low zirconia contents.**

The aim had been to measure the BET surface areas of the fresh and fired (non-palladated) samples. However, there was only time to analyse three of the samples. What can be concluded from Figure 5.14 is the possibility of high surface areas, especially for the mixed oxides when compared to the single oxides.

This also sheds some light upon the reason for the rise and subsequent fall in catalytic activity as detected from TPR and shown in Figure 5.11. If the mixed-oxide samples give greater surface areas, then they are also likely to exhibit greater activity.

## Using dynamic light scattering to find the hydrodynamic particle radius

The sizes of the hydrated particles in the samples of product suspension were investigated using Zetasizer apparatus. This apparatus uses the principle of dynamic light scattering (DLS) to find the hydrodynamic particle radius.

Molecules in liquids are undergoing constant diffusion, which will cause movement of particles suspended within, known as Brownian motion. The diffusion coefficient is related to the size of the diffusing object and can be expressed using the Stokes-Einstein equation:

$$D = \frac{kT}{6\pi\eta R_H}$$

**The Stokes-Einstein equation**

$D$ = diffusion coefficient

$R_H$ = hydrodynamic particle radius

$T$ = temperature

$\eta$ = viscosity of medium

DLS is used to measure the diffusion coefficient. Polarised laser light is shone into a sample of the suspension. Incident photons cause an oscillation in the electron cloud of the molecules in the suspension medium. As the dipole changes, energy is radiated in all directions. The intensity of this scattered light is measured over time. This intensity fluctuates as a consequence of diffusion in the liquid medium of the suspension. This fluctuation can be analysed using a correlation function to provide the diffusion coefficient, and hence, using the Stokes-Einstein equation above, a value for particle radius can be obtained. The range of sizes detectable by Zetasizer DLS equipment was ca. 2 nm – 3 μm, but becomes less and less accurate at lower particle sizes.

It was hoped that DLS would provide an alternative method of particle-size measurement, which allowed results to be obtained faster, without having to settle, decant and dry the suspension, as is necessary for both BET and PXD. The hydrodynamic particle radius was therefore measured for the oxide samples containing differing proportions of ceria and zirconia, as shown in Figure 5.13.

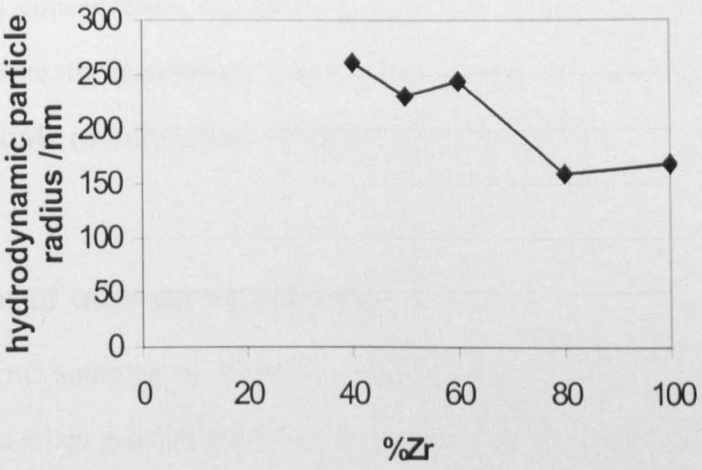


**Figure 5.13: Zetasizer results showing a general trend toward smaller particle size with greater zirconium content in ceria-zirconia mixed-oxide compounds**

The DSL results in Figure 5.13 show that a general decrease in particle size is observed on increasing zirconia percentage. These measured particle sizes are much larger than those estimated by PXD (which were usually diameters of 50 nm or less, compared to these radii corresponding to diameters of 300 nm or more). Whilst we might initially conclude that PXD was detecting small crystallites, but these were agglomerated into the large particles detected by DLS, this is not very likely, as we would then see much lower surface-area measurements with BET.

One possible explanation for the high particle-size values from DLS is that the *effective* radius – which is what is being measured, i.e. the radius of a particle that would cause the diffusion observed – is much larger than the actual radius, as found from BET and estimated from PXD. Another, very likely reason is that DLS is less well-suited to measuring the size of the very smallest particles. Therefore, those sizes that are obtained are likely to be those of the larger particles in the distribution. The values therefore do not represent a mean size, unlike those from PXD and BET and may therefore not be representative of the

sample. As a consequence, the DSL method was rejected as a useful method for particle-size measurement, and a combination of PXD, BET and, on occasion, TEM (transmission electron microscopy) was used in future experiments.

## Assessment of take-up on substrate

Separate 5 $cm^3$ samples of 50:50 and 20:80 ceria:zirconia suspension were stirred with a silica powder (SP18-9638) or with an alumina powder (Puralox SCFa-140). The samples were filtered, and the filtrate dried. The dry mass was then compared with the dry mass obtained from evaporating the water from 5 $cm^3$ of each fresh suspension and filtering through the same grade of filter paper.

The results of the absorption experiments are shown in Table 5.2; it can be seen that both samples are taken up better on silica than on alumina. Also, the zirconia-rich sample is taken up less well than that with equal ceria-zirconia content.

**Table 5.2: results from experiments to assess the "take-up" of nanoparticles with different Ce:Zr ratios upon a substrate**

| Ce:Zr ratio | Dry mass of fresh /g | Dry mass on silica /g | Dry mass on alumina /g | Mass taken up on silica /g | Mass taken up on alumina /g | % take up on silica | % take up on alumina |
|---|---|---|---|---|---|---|---|
| 50:50 | 0.1353 | 0.1153 | 0.1363 | 0.02 | [-0.001] | **15%** | **LOW** |
| 20:80 | 0.0595 | 0.0558 | 0.0566 | 0.0037 | 0.0029 | **6%** | **5%** |

## Conclusions for characterisation work

In summary, it was observed that differing proportions of cerium and zirconium within a mixed oxide cause, as might be expected, different properties to be exhibited by the powder.

It seems that the formulations containing only ceria or only zirconia show the lowest catalytic activity. This is as expected from past experiments[21], where greater percentage zirconia content led to smaller particles – but it is the cerium dioxide that provides the best oxygen-storage properties (with zirconium added to stabilise the structure). Hence, as zirconium content increases, surface area increases but oxygen-storage decreases, giving an optimum somewhere approaching mid-way between the two.

The effects of palladation in these experiments were as expected: palladation reduced the temperature at which the oxygen in the powder could react with hydrogen in the TPR experiment.

In addition, it was noted that the dynamic light scattering (using "Zetasizer" apparatus) was not a useful method for the calculation of particle sizes, primarily because the particles are smaller than the range detectable by the apparatus.

## The effect of reaction conditions upon formation of ceria-zirconia particles

### Strategy

According to the discussion in Chapter 1, an increase in flow-rate would be expected to cause a decrease in residence time, which, in turn would lead to a decrease in particle size. Experiments using a range of flow-rates, whilst keeping other parameters constant, were therefore performed.

Increasing temperature would be expected to have some effect upon particle size, but this might be an increase or a decrease, depending upon the relative effects of nucleation rate and diffusivity. Experiments were performed at a range of temperatures. Since changing the temperature of water also decreases

its density, the pump flow rates were also changed so that the volumetric flow rate through the reactor should be the same for all experiments.

An increase in solute concentration would be expected to cause an increase in nucleation rate and therefore a decrease in particle size. Experiments at a range of precursor concentrations were therefore attempted.

When moving to Rig 2, it was decided to perform new experiments at a range of temperatures, but without the adjustment of pump rates. The pumps were not deemed to be accurate enough for such delicate adjustment to have any effect, and adjusting too many parameters at once might lead to an effect that was difficult to identify or repeat.

It is interesting to see whether the reaction will still be able to occur at lower or higher pressures than those we have normally used (ca. 260 bar). Lower operating pressures would be useful if the process were to be scaled up, since they would make reactor construction much easier. With this aim in mind, experiments were carried out at a range of pressures. According to the previous discussion, changes in pressure would be unlikely to have much effect at subcritical conditions, as the compressibility of water is low.

## 1. Changing residence time

Solutions were prepared from zirconyl nitrate hydrate and cerium ammonium nitrate that were 0.1 M in zirconium and 0.056 M in cerium. Reactions were carried out in Rig 1. (These unusual ratios were used owing to an initial miscalculation of the relative formula mass of the cerium precursor that was only discovered later!)

In order to know the residence time ($t_r$) of the reaction, from control of flow rates, it was necessary to know the approximate volume of the reactor. This, in turn, required a definition of what constituted the "reactor" within the entire

rig. This was defined as the section of the rig tubing where the reaction can take place: i.e. the volume that is hot and in which the precursors and hot water are mixing or have already mixed. Therefore, the volume of the "reactor" in Rig 1 is taken to be the volume of the mixing T-piece: the metal salts and hot water are assumed not to mix upstream, whilst the hot reaction mixture is immediately cooled downstream.

The volume of the reactor T-piece was measured by filling an identical T-piece with water and then measuring the amount of water that was required. This was performed three times and a mean value taken, yielding the value 3.6 $cm^3$.

Whilst the total flow rate into and out of the rig is known to be 15 ml $min^{-1}$, the volumetric flow rate through the T-piece will be greater. The density of water at the high temperatures and high pressures in the reaction zone will be lower than that at room temperature. The mass of water flowing through any point in the reactor, however, *is* known to be 15 g $min^{-1}$. The volume of water flowing through a point in the T-piece can therefore be calculated using the specific volume of water at the conditions in the rig (300°C, 250 bar). This was found, from steam tables, to be 0.0013 $m^3$ $kg^{-1}$, which is equivalent to a density of 0.75 g $cm^{-3}$.

The flow rates required to give different residence times, but keeping the water:metal salt pump ratio at 2:1, were calculated in Table 5.3.

**Table 5.3: flow rates required for different residence times with reactor conditions of 300°C and 250 bar. These are calculated from the reactor volume and knowing the density of water at these conditions.**

| $t_r$ /s | F /ml min (through system) | | |
|---|---|---|---|
| | water | metal | Total |
| 5.35 | 20.00 | 10.00 | 30.00 |
| 8.03 | 13.33 | 6.67 | 20.00 |
| 10.70 | 10.00 | 5.00 | 15.00 |
| 13.38 | 8.00 | 4.00 | 12.00 |
| 16.06 | 5.00 | 3.33 | 10.00 |

A sample of 200 $cm^3$ was collected for each reaction – these samples were a slightly yellow opaque suspension. To each sample was added 17 g of Amberlyst ion-exchange resin (see method 5 in the Sample Preparation section above). Each sample was then stirred overnight during which time the nanoparticles had settled. The supernatant liquid was removed by pipette; the remaining material was then filtered through a wire mesh to remove the Amberlyst beads. These beads were then washed with deionised water to allow as much of the oxide particles as possible to pass through the wire mesh. The resulting filtrate was dried in an oven at ca. 80°C and the dry particles thus formed were submitted for PXD to approximate particle sizes. Two different peaks were used and so each sample gave two different particle sizes for comparison. These results are shown in Figure 5.14.

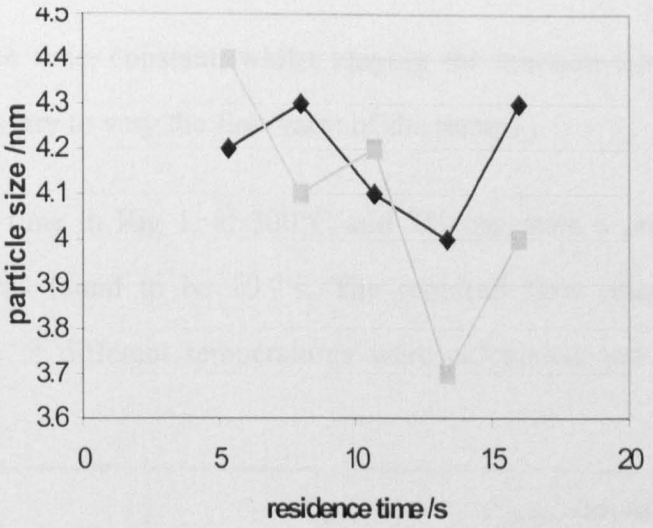


**Figure 5.14: Comparing the sizes of particles from products made with differing residence times (controlled by varying flow rates), it can be seen that the particle size varies very little in the range of residence times tested. This shows that, whilst it was not possible to vary the particle size by this method, it is therefore possible to make particles of the same size no matter what residence time is used. A reasonable agreement between sizes estimated from peak A (◆) and peak B (■) was observed.**

As can be seen from Figure 5.14, using flow rates to vary the residence times between 5 and 16 s has little effect on the particle size. This is contrary to predictions. It must therefore be concluded that the particles form completely in a very short time and do not grow any further.

## 2. Changing temperature and flow rate

As the temperature of the reactor is changed, the properties of water will also change. Water becomes less dense as it nears its critical point – it is this very change in density that is often used to distinguish "near-critical" water as something distinct from the liquid. If the density of water in the reaction zone is significantly less than that of water at ambient temperature, the volumetric flow rate in that zone will not equal the flow rate of the pumps feeding water and metal-salt solution into the reactor. To keep the volumetric flow rate, and

hence residence time, constant, whilst varying the reaction temperature, it is therefore necessary to vary the flow rates of the pumps.

The residence time in Rig 1, at 300°C and 250 bar, with a pumping rate of 15 ml min-$^{1}$ was found to be 10.7 s. The required flow rates to give this residence time at different temperatures were calculated and are shown in Table 5.4.

| $T$ /°C | $V$ /m$^3$ kg$^{-1}$ | $d$ /kg m$^{-3}$ | $F_{pumps}$ /ml min$^{-1}$ | | |
|---|---|---|---|---|---|
| | | | *water* | *metal* | *total* |
| 200 | 0.001134 | 882 | 11.86 | 5.93 | 17.79 |
| 220 | 0.001164 | 859 | 11.56 | 5.78 | 17.34 |
| 240 | 0.001198 | 835 | 11.23 | 5.61 | 16.84 |
| 260 | 0.001238 | 807 | 10.86 | 5.43 | 16.29 |
| 280 | 0.001268 | 777 | 10.46 | 5.23 | 15.69 |
| 300 | 0.001345 | 743 | 10.00 | 5.00 | 15.00 |

**Table 5.4: calculating required pumping rates to keep a constant residence time in the hot reactor zone of the rig whilst it is at different temperatures. $T$ = reaction temperature; $V$ = specific volume of water at $T$ and 250 bar; $d$ = density of water at $T$ and 250 bar; $F_{pumps}$ = required flow rate of pumps**

Feed solutions were prepared from zirconyl nitrate hydrate and cerium ammonium nitrate that were 0.1 M in zirconium and 0.056 M in cerium, as before. The calculated pumping rates from Table 5.4 were used to program the pumps for the experiment, at temperatures ranging from 200 to 300°C. Amberlyst beads were once more used to settle the particles from the crude product suspension; the supernatant liquid was then removed by pipette and the remaining particles dried in an oven at ca. 80°C. The resulting dry powder

was then submitted for PXD testing, and the particle size for each sample estimated using the Scherrer equation. The results are presented in Figure 5.15.

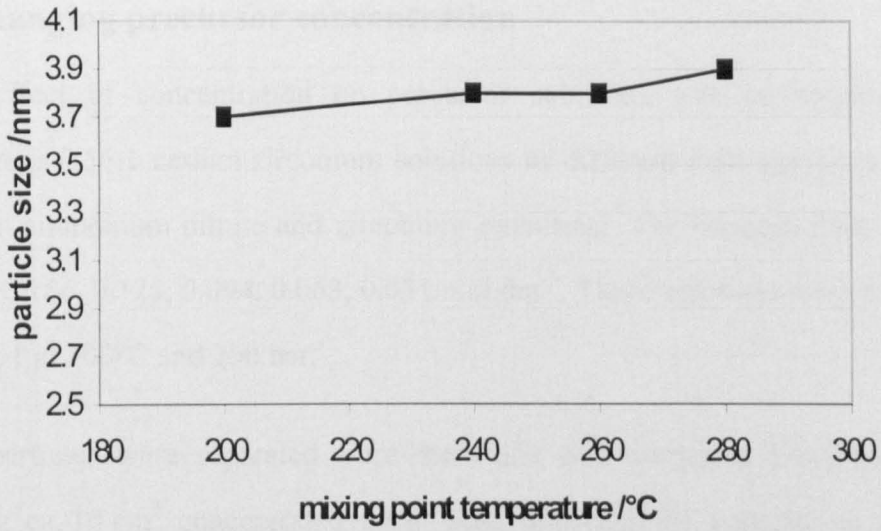


**Figure 5.15: Changing the reaction temperature at the same time, whilst changing the flow rate of the feeds to keep the residence time the same, has a negligible effect on ceria-zirconia particle size, as seen in the graph. The graph does, however, show that it should be possible to make particles of similar size consistently despite fluctuations in temperature.**

The results show that changing temperature within the range tested (200-300°C), whilst keeping the volumetric flow rate the same does not have any observable effect upon the particle size, which remains constant at ca. 3.8 nm. This is contrary to predictions that adjustment of temperature should affect particles size. This may be due to the fact that a large enough range of temperatures was not tested. It may also be due to fluctuations in temperature throughout the experiment meaning that the recorded temperature was not very representative of what was actually happening in the reactor.

Once more, whilst this result did not show that control of particle size is possible, it did show the possibility of reliably making particles of the same

size *despite* the use of different temperatures; it is useful if using a lower temperature is feasible, as the reactor would require less energy to run.

## 4. Changing precursor concentration

The effect of concentration on precursor solutions was investigated by preparing 0.56:1 cerium:zirconium solutions of different concentrations from cerium ammonium nitrate and zirconium oxynitrate. The concentrations used were: 0.156, 0.125, 0.094, 0.063, 0.031 mol $dm^{-3}$. These solutions were reacted in Rig 1 at 300°C and 250 bar.

The particles were separated from the water and unreacted precursors by adding ca. 10 $cm^3$ concentrated nitric acid, allowing the particles to settle, removing the clear supernatant liquid by pipette, and finally allowing the material to dry in an oven at 80°C. The particles were then submitted for PXD analysis so as to estimate the particle sizes using the Scherrer equation. The results are presented in Figure 5.16.

Figure 5.16 shows that the particle size in samples produced from precursors with a range of concentrations were all very similar, with a range of only 0.5 nm. A decrease in particle size with increasing solute concentration was expected. The fact that no such change was observed might be put down to the fact that a fairly small range of concentrations was used. Whilst control of particle sizes would be useful, what can be seen is that relatively high concentrations of precursors can nonetheless lead to particles of a similar size to those made at low concentrations. If this process were to be used for larger-scale preparation of nanoparticles, the use of higher concentrations, and therefore the attainment of greater yields, would be very useful.

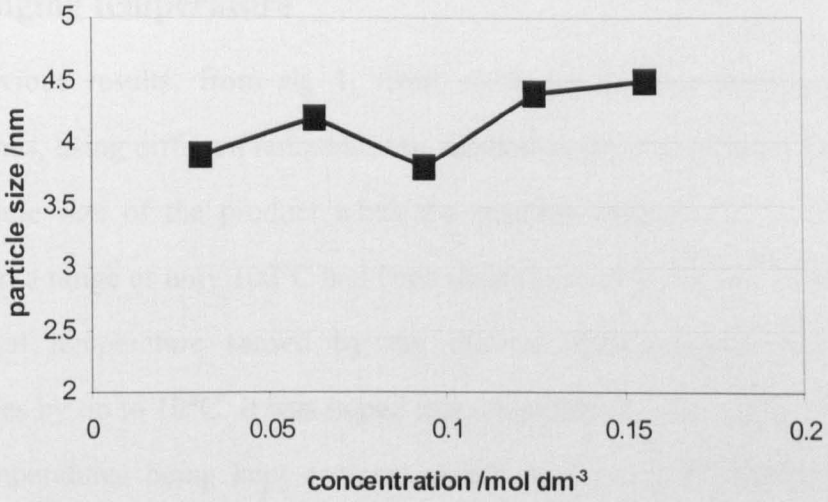


**Figure 5.16: The size of the particles produced at different precursor concentrations varies very little with changing concentration over the range tested, as can be seen from this graph. This means that relatively high precursor concentrations could be used without adversely affecting the size of particles in the product.**

## Rig 2: a new and more-reliable rig – testing dependence of ceria particle properties on reaction conditions

Rig 2 was designed with an improved mixing-piece design and a more effective water heater (see Chapter 2). This allowed the reactor to be run at higher temperatures more easily, owing to the greater efficiency of the heater, and also for more runs to be made without blockages, owing to the new mixing-piece.

It was decided to make further investigations of particle size control but this time to investigate only ceria (and not ceria-zirconia) compounds, as they very rarely cause blockages, and the PXD results are much easier to analyse, as fewer reflections are present.

## 1. Changing temperature

The previous results, from rig 1, from synthesis of ceria-zirconia mixed compounds, using different temperatures, seemed to show very little change in the particle size of the product when the reaction temperature is changed. However, a range of only 100°C had been used (from 200-300°C). In addition, the actual temperature sensed by the internal thermocouples fluctuated, sometimes by up to 10°C. It was hoped that temperatures over a greater range, with temperatures being kept constant, might lead to more conclusive and interesting results.

Experiments were therefore performed in Rig 2, using 0.2 mol $dm^{-3}$ cerium ammonium nitrate at a range of mixing-point temperatures from 100°C to 300°C. In order to allow these temperatures to be attained, but not exceeded, the operating temperature of the pre-heater was also adjusted. The pre-heater temperature ($T_{pre}$) was calculated from the desired mixing-point temperature ($T_{mix}$) by keeping a constant ratio between the two (using the absolute temperatures, expressed in Kelvin). It was known to be possible to maintain the mixing-point temperature at 300°C when the pre-heater was running at 400°C. Therefore the ratio required was calculated as in Equation 5.4.

$$\frac{T_{pre}}{T_{mix}} = \frac{400°C}{300°C} \equiv \frac{673\ K}{573\ K} = \mathbf{1.175}$$

**Equation 5.4: Calculation of feasible ratio of pre-heater temperature ($T_{pre}$) to mixing-point temperature ($T_{mix}$)**

The temperatures calculated from Equation 5.4 are presented in Table 5.5.

**Table 5.5: necessary pre-heater temperatures to maintain required mixing-point temperatures, as calculated from Equation 5.4**

| Mixing-point temperature /°C | Pre-heater temperature /°C |
|---|---|
| 100 | 165 |
| 140 | 212 |
| 180 | 259 |
| 220 | 306 |
| 260 | 353 |
| 300 | 400 |

Pressure in the reactor was maintained at 250 bar, and flow rates were maintained at 10 ml $min^{-1}$ for the water flow, and 5 ml $min^{-1}$ for the metal-salt flow. A 200 $cm^3$ sample of crude product was collected from each experiment to which was added ca. 20 $cm^3$ of concentrated nitric acid. The particles were allowed to settle overnight and the clear supernatant liquid was removed by siphoning. The remaining particles were dried overnight in an oven at ca. 80°C. The dry powder was then submitted for PXD analysis and particle size estimated using the Scherrer equation. Two peaks were used for the analysis, so that two estimates for the particle size could be compared, and errors due to incorrect selection of $CeO_2$ peaks could be detected. The chosen peaks were at $2\theta = 28.6°$ (peak A) and 33.1°C (peak B).

For the experiments performed at 100°C and 140°C, whilst some opaque oxide product was clearly observed to have formed in the reactor output, the PXD traces did not show clear $CeO_2$ peaks. It was concluded that the cerium oxide produced was not sufficiently crystalline for PXD analysis. This indicates that, whilst particles were nucleated, they did not grow sufficiently to become more crystalline, possibly because the rate of crystal growth was too low at the low temperatures. The estimated particle sizes are presented in Table 5.6 and Figure 5.17.

**Table 5.6: In Rig 2, increasing reaction temperature *does* appear to yield larger particles, despite earlier results from the older rig showing little change in particle size with increasing reaction temperature.**

| Mixing-point temperature /°C | Estimated particle size from PXD | |
|---|---|---|
| | 2θ = 28.6° (A) | 2θ = 33.1° (B) |
| 100 | * | * |
| 140 | * | * |
| 180 | 2.9 | 2.0 |
| 220 | 3.3 | 3.7 |
| 260 | 4.6 | 4.3 |
| 300 | 6.2 | 5.8 |

* indicates those samples not sufficiently crystalline to analyse for particle size estimation.

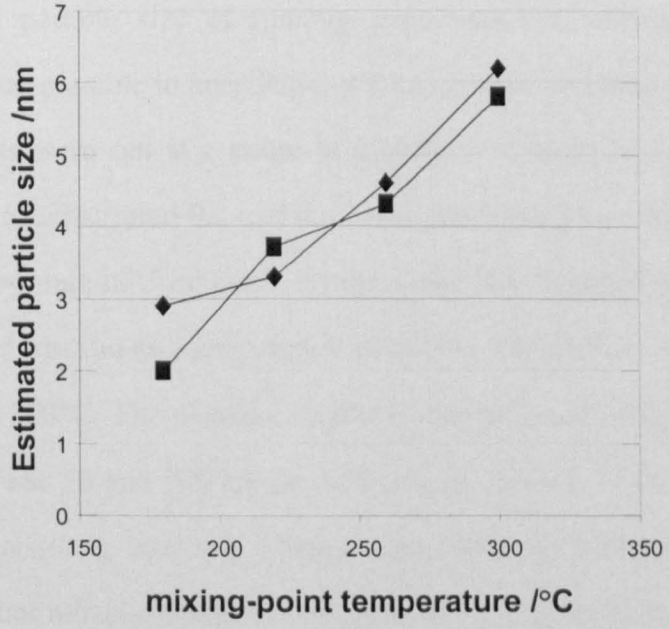


**Figure 5.17: Plot showing how the estimated particle size increases with increasing mixing-point temperature. A good agreement between sizes estimated for peak A (◆) and from peak B (■) is observed.**

As can be seen in Figure 5.17, there appears to be an approximately linear relationship between reaction temperature and particle size. This is in contrast

to the results from ceria-zirconia synthesis in Rig 1, which showed no significant change in the particle size with changing temperature. This suggests that the reaction temperature is more accurately controlled in Rig 2 configuration, with the new nozzle, than in Rig 1, which contained the basic T-piece.

The fact that an increase, and not a decrease, in particle size with increasing temperature was observed, suggests that diffusivity effects are more important than the change in nucleation rate. The increase in diffusivity at greater temperature (expected to yield larger particles) must override the effect of the increase in nucleation rate (expected to yield smaller particles).

## 2. Changing pressure

The constantly varying pressure in Rig 1 had made it impractical to investigate the effect on particle size of running experiments at different pressures. However, it was possible to keep Rig 2 at a much more consistent pressure and so experiments were run at a range of pressures. Cerium ammonium nitrate solution with concentration 0.2 mol $dm^{-3}$ was prepared. This was pumped into Rig 2 at a flow rate of 5 ml $min^{-1}$, whilst water was pumped at 10 ml $min^{-1}$. The pre-heater was run at a temperature of 400°C whilst the mixing point was maintained at 300°C. The pressure regulator was adjusted to keep a specified pressure between 50 and 300 bar as indicated in Table 5.7. The very highest and lowest pressures, however, seemed impossible to maintain: the Gilson pumps could not reliably maintain a pressure of 300 bar, and this pressure also caused the joints in the remainder of the reactor to leak; at 50 bar, the 300°C mixing-point temperature was unreachable.

**Table 5.7: conditions used for experiments to investigate the effect of changing pressure upon particle size. Two experiments were aborted: [a] at 300 bar, the Gilson pumps began to stop working properly and the joints of the reactor began to leak; [b] at 50 bar, the required mixing-point temperature of 300°C could not be reached**

| Experiment number | Pressure /bar |
|---|---|
| 1 | 300[a] |
| 2 | 250 |
| 3 | 200 |
| 4 | 150 |
| 5 | 100 |
| 6 | 50[b] |

The product suspensions were acidified to force the particles to settle. The clear supernatant liquid was then removed by siphoning, and the remaining particles dried in an oven at ca. 80°C. The particles were then analysed using PXD and the particle sizes estimated using the Scherrer equation. Two different peaks at 2θ values of 28° and 33° were used so that any errors caused due to reflections not caused by $CeO_2$ nanoparticles would be obvious. The results are displayed in Figure 5.18.

As can be seen in Figure 5.18, the estimated particle sizes from the two different PXD reflections agree well with each other, showing that the chosen reflections were both caused by the same species. Any change in particle size caused by the differences in pressure is small, and a trend cannot easily be recognised. This confirms the prediction that pressure would have little effect upon particle size at the subcritical conditions being used here.

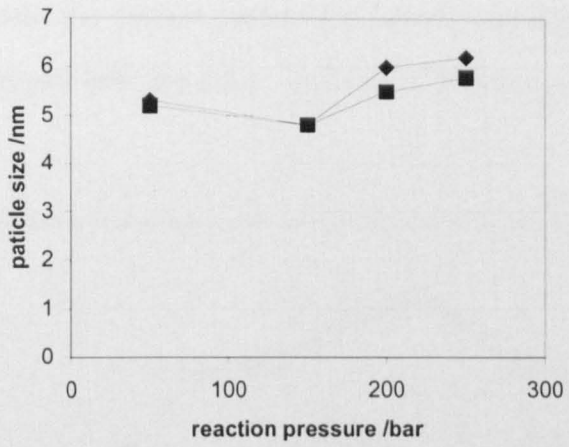


**Figure 5.18: as can be seen from a plot of particle size against reaction pressure, there is little or no effect of increasing pressure upon particle size. Two different peaks were used for particle size estimation: 2θ = ca. 28° (◆) and ca. 33° (■). These can be seen to have given a good agreement.**

It may therefore be possible to run experiments at a generally lower pressure and still achieve the same results; this would be useful if the process were ever to be considered for industrial purposes.

## *Conclusions*

A major achievement is that acidification followed by decantation has been identified as an effective method of particle separation. In addition, we have shown that some control of particle size is possible with Rig 2, yielding larger particles at higher temperatures. Rig 2 also gives better control of the temperature at the mixing point than Rig 1.

## Additional $CeO_2$ experiments, carried out by Dr. Paul Blood

After my work was finished, Dr. Paul Blood conducted additional experiments to make cerium dioxide nanoparticles, using Rig 3. Notably, a series of experiments was performed where the metal-salt flow rate was varied within a range of 1-10 ml $min^{-1}$, whilst the flow rate of the water feed was kept at

10 ml $min^{-1}$. The specific surface area of the sample was then measured using adsorption of nitrogen and the BET isotherm. The results are presented in Figure 5.19.

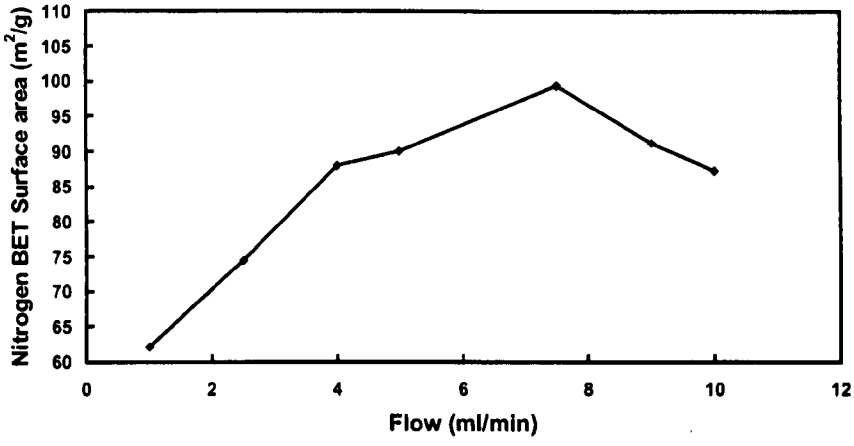


**Figure 5.19: As the flow rate of metal-salt solution is increased, the specific surface area of the particles in the product increases towards a maximum (i.e. a minimum particle size is reached). Above this optimum flow rate, the surface area of the product is seen to decrease once more (indicating an increase in particle size).**

The first possible explanation for this behaviour, involving particle nucleation and growth, is easier to understand. At low flow rates, the metal salt will travel through the reactor slowly, allowing greater time for particle nucleation and significant particle growth. This would lead to the formation of larger particles (and hence lower surface area). The residence time would be expected to decrease as flow rate increases, resulting in smaller particles (and greater surface area). At the highest flow rates, the residence time of reagents in the reactor is smaller, but the local metal-ion concentration is much greater, which would lead to excessive particle growth and smaller surface area.

Another explanation, involving fluid dynamics, might therefore be offered as follows. The forces at work in a fluid-flow system can be divided into three types:

- **viscous force:** this serves to hold the fluid together and keep the flow laminar

- **inertial force:** produced by forced convection (i.e. pumping)

- **buoyancy force:** produced by natural convection (i.e. density gradients)

Buoyancy forces in most systems are usually insignificant. However, the system within the new flow-reactor design (in Rigs 2 and 3) depends upon buoyancy forces, from the difference in density between the hot and cold streams, for efficient mixing. The ideal situation in the reactor is therefore for buoyancy forces to be greater than inertial and viscous forces.

An indicator of the interaction between buoyancy and viscous forces is the Grashofs number, Gr. This is approximately equal to the buoyancy forces divided by the viscous forces. Turbulent flow, caused by fluid buoyancy, results when Gr > ca. 100, and this constitutes the ideal reaction scenario.

At low metal-salt flow rates, inertial forces will be low compared to buoyancy; however, the much higher flow inertia of the hot water flow would cause a reduction in buoyancy-induced turbulence. The hot-water flow would be likely to penetrate significantly down into the metal-salt inlet because of large differences in relative inertia. Particles would begin to form upstream of the mixing point, and have a longer residence time, leading to larger particles and lower surface area.

This effect would diminish as the metal-salt flow rate increases relative to the water flow rate, leading to smaller particles and greater surface areas. However, at the highest flow rates, inertial forces will begin to dominate, once more disrupting the ideal buoyancy-driven scenario and leading to slower mixing, larger particles and higher surface areas.

## Final Conclusions

The experiments performed in Rig 2 have proven to be repeatable, which is vital to the future use of this method in nanoparticles synthesis. The key to controlling particle size appears to be in controlling the reaction temperature. It should also be noted that the relative flow rate of water and metal salts appears to have a strong, but perhaps less predictable, effect upon particle size. It is possible that the normal high pressures used in these reactions may not be necessary, and use of a lower pressure, whilst still many times atmospheric pressure, may be possible.

These results are promising for the ongoing work upon synthesising these nanoparticles in near-critical hydrothermal flow reactors, for their possible use in such exciting technologies as fuel cells.

## Possible future work

It would be interesting to be able to investigate what effect supercritical conditions would have upon particle size, now that an effect of temperature on particle size has been identified. At supercritical conditions, there might also be an effect of pressure upon particle size. The effect of reactant concentration could also be investigated further over a much wider range of concentrations to see whether the predictions of its effect on particle size were correct. Finally, it would be advantageous to find a less environmentally damaging variation on the separation technique that was identified – by adding, for example, a soluble salt instead of acid.

## References


[1] J. M. Thomas, W. J. Thomas, *Principles and Practice of Heterogeneous Catalysis*, Wiley-VCH, Weinheim, Germany, **1996**.

[2] J. Kaspar, P. Fornasiero, M. Graziani, *Catal. Today* **1999**, *50*, 285.

[3] A. Trovarelli, *Catal. Rev.-Sci. Eng.* **1996**, *38*, 439.

[4] G. C. Koltsakis, I. P. Kandylas, A. M. Stamatelos, *Chem. Eng. Commun.* **1998**, *164*, 153.

[5] EP337809, Europe, **1989**.

[6] J. P. Cuif, G. Blanchard, O. Touret, A. Seugneurin, M. Marezi, E. Quémeré, SAE 970463, **1997**.

[7] R. M. Heck, R. J. Farrauto, *Catalytic Air Pollution Control - Commercial Technology*, John Wiley & Sons Inc, **1994**.

[8] S. P. Jiang, S. H. Chan, *J. Mater. Sci.* **2004**, *39*, 4405.

[9] Yokokawa H, Sakai N, Horita T, Yamaji K, B. ME, *Electrochem.* **2005**, *71*, 20.

[10] R. di Monte, J. Kašpar, *J. Mater. Chem.* **2004**, *15*, 633.

[11] A. Trovarelli, *Catalysis by ceria and related materials*, Imperial College Press, London, **2002**.

[12] M. Yashima, M. Yoshimura, *Jpn. J. Appl. Phys.* **1992**, *31*, L1614.

[13] T. Masui, Y. Peng, K. Machida, G. Adachi, *Chem. Mater.* **1992**, *10*, 4005.

[14] M. Yashima, K. Morimoto, N. Ishizawa, M. Yoshimura, *J. Am. Ceram. Soc.* **1993**, *76*, 1745.

[15] C. de Leitenberg, A. Trovarelli, F. Zamar, G. Maschio, G. Dolcetti, J. Llorca, *Chem. Commun.* **1995**, 2181.

[16] A. Deptula, M. Carewska, T. Olczak, W. Lada, F. Croce, *J. Electrochem. Soc.* **1993**, *140*, 2294.

[17] T. Masui, J. Fujiwara, Y. Peng, T. Sakata, K. Machida, H. Mori, G. Adachi, *J. Alloys Cmpd.* **1998**, *269*, 116.

[18] B. Djurcic, D. McGarry, S. Pickering, *J. Mater. Sci. Lett.* **1993**, *12*, 1320.

[19] M. Hirano, E. Kato, *J. Ceram. Soc. Jpn.* **1996**, *104*, 958.

[20] Y. Hakuta, S. Onai, H. Terayama, T. Adschiri, K. Arai, *J. Mater. Sci. Lett.* **1998**, *17*, 1211.

[21] A. Cabañas, J. A. Darr, E. Lester, M. Poliakoff, *Chem. Commun.* **2000**, 901.

[22] A. Cabañas, J. A. Darr, E. Lester, M. Poliakoff, *J. Mater. Chem.* **2001**, *11*, 561.

[23] V. C. Malshe, E. S. Sujatha, *React. Funct. Polym.* **1997**, *35*, 159.

# Chapter 6: Iron Oxide

## *Summary*

The formation of $Fe_3O_4$ and ferrites, containing ions of a different metal in addition to iron, with formula $MFe_2O_4$, had previously been examined in Nottingham using the hydrothermal flow apparatus[1]. This work had been performed with degassed water, and hence, without dissolved oxygen in the water, had led to magnetite, $Fe_3O_4$, with a lower oxidation state of iron. The work for this Thesis, using deionised water without further treatment as reactant and solvent, led to $Fe_2O_3$ (hematite), owing, presumably to the oxidising effect of the dissolved oxygen. The possibility of forming $\gamma$-$Fe_2O_3$ (as opposed to the more usual polymorph, $\alpha$-$Fe_2O_3$) was also investigated, but turned out not to be possible using the techniques attempted here.

Assessment of the conversion and yield in previous experiments had been rather difficult: unknown amounts of product particles remain in the reactor tubing, and a quick, simple way of finding the concentration of precursor remaining in the product stream was not available. One reason for choosing to investigate iron oxide was that it would be straightforward to measure the concentration of dissolved, unreacted, iron precursor by using the atomic absorption (AA) technique.

The use of this technique allowed the investigation of the effects of temperature change on conversion and particle size. As had already been suggested from work on ceria and ceria-zirconia, reactions to make iron oxide that are carried out at higher temperatures lead to larger particle sizes. With the evidence from the AA technique, it can also be seen that they lead to greater conversions and yields.

Freeze drying was employed as a method for producing dry particles without the agglomeration that occurs when drying in the oven. Particles formed at lower reactor temperatures formed a deep-red, clear suspension and were found, by TEM, to be very small. Particles formed at a higher temperature were rust-red and formed an opaque suspension. TEM showed that these particles were considerably larger than those formed at the lower temperature.

It has been found, by materials scientists at Nottingham, that graphitic nanofibres can be produced through chemical vapour deposition (CVD) from an ethene-hydrogen gas mixture, using $Fe_2O_3$ nanoparticles as a catalyst. Iron oxide particles were made using the hydrothermal flow process at different temperatures. Crystalline particles formed at 300°C were found to provide better yields of graphitic nanofibres than those formed from conventional precipitation techniques. The less crystalline particles did not allow any formation of nanofibres under CVD except at very high temperatures.

## The different phases of Iron Oxide

Iron oxide can exist in several forms[2]. The first is FeO, which is an unstable pyrophoric compound, which will disproportionate to Fe and $Fe_3O_4$. It possesses a rock-salt structure (i.e. a face-centred cubic lattice of $O^{2-}$ with $Fe^{2+}$ occupying the octahedral interstices).

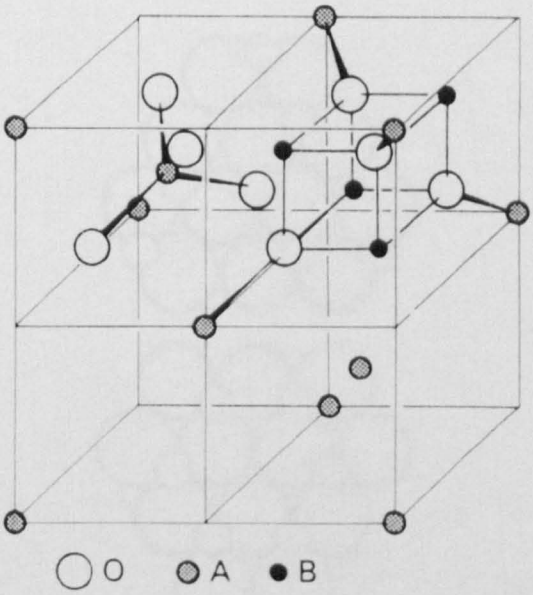


**Figure 6.1: The normal spinel structure, reproduced from Shriver et al.[3], highlighting the environments of the A and B ions consisting of a face-centred cubic $O^{2-}$ lattice with $A^{2+}$ occupying one eighth of the tetrahedral holes, and $B^{3+}$ occupying one half of the octahedral holes. The structure of magnetite is, however, an inverse spinel, in which an eighth of the tetrahedral holes contain $Fe^{3+}$ whilst half of the octahedral holes contain equal proportions of $Fe^{2+}$ and $Fe^{3+}$ ions.**

Magnetite ($Fe_3O_4$) is an oxide containing iron with mixed oxidation states, with a $Fe^{3+}$:$Fe^{2+}$ ratio of 2:1 and might therefore be expressed as $Fe^{II}Fe^{III}{}_2O_4$. The compound has an inverse spinel structure: a spinel, whether inverse or normal, has formula $AB_2O_4$. A normal spinel consists of a face-centred cubic lattice of $O^{2-}$ ions[3] within which, one eighth of the tetrahedral holes are

occupied by $A^{2+}$ ions, whilst one half of the octahedral holes are occupied by $B^{3+}$ ions. The inverse spinel structure (adopted by magnetite) differs from the normal spinel structure in that $B^{3+}$ ions now occupy one eighth of the tetrahedral holes whilst half of the octahedral holes are now occupied by both $A^{2+}$ and $B^{3+}$ ions in a 1:1 ratio. The normal spinel structure is illustrated in Figure 6.1. Metal ferrites with formula $MFe_2O_4$ will also adopt a normal or inverse spinel structure.

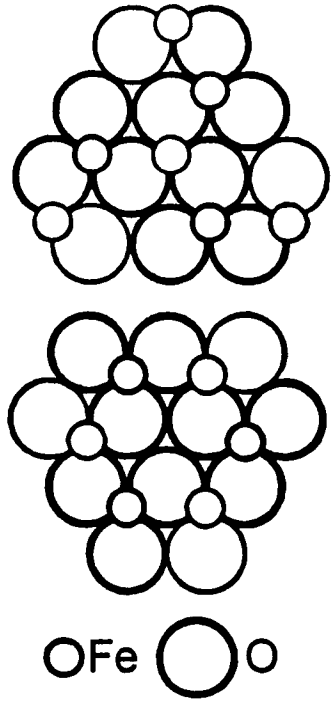


**Figure 6.2: The structure of $\alpha$-$Fe_2O_3$, reproduced from Bragg et al.[4], showing successive layers of atoms: two-thirds of the octahedral interstices in a cubic close-packed lattice of $O^{2-}$ ions are filled with $Fe^{3+}$ ions.**

The third form of iron oxide is $Fe_2O_3$ which itself can be found in a variety of modifications, most notably the $\alpha$- and $\gamma$-forms. The more common form is hematite ($\alpha$-$Fe_2O_3$), which has the corundum structure, giving it the same structure as $\alpha$-$Al_2O_3$: a hexagonal close-packed lattice of $O^{2-}$ has two-thirds of its octahedral holes filled with $Fe^{3+}$ ions. The structure of $\alpha$-$Fe_2O_3$ is shown in Figure 6.2.

$\gamma$-$Fe_2O_3$ is metastable and can be obtained by careful oxidation of $Fe_3O_4$, and has a cubic structure. Heating $\gamma$-$Fe_2O_3$ *in vacuo* causes it to revert to $Fe_3O_4$, whilst heating in air causes it to be converted to $\alpha$-$Fe_2O_3$.

The interconversion of FeO, $Fe_3O_4$ and $\gamma$-$Fe_2O_3$ is possible due to their structural similarity: each contains a cubic close-packed lattice of $O^{2-}$ ions whereas $\alpha$-$Fe_2O_3$ is based upon a hexagonal close-packed structure.

## The uses for iron oxide and metal ferrite nanoparticles

Hematite particles are used as pigments in paint, as magnetic materials, catalysts and gas sensing materials, and in photoelectric devices[5, 6]. Iron-containing spinel compounds, such as magnetite ($Fe_3O_4$) and metal ferrites have found use in a variety of materials, including magnetic pigments in recording media and in catalysis[7, 8]. Nanoparticles of these magnetic materials are of particular interest, as they could lead to the possibility of miniaturising the devices that use them[9]. Magnetic properties depend strongly upon particle size: whilst a large particle will contain many magnetic domains, a nanoparticle might contain only one domain, where the spins of all atoms in the particle will be aligned in the same direction.

## Standard syntheses of these compounds

Particles are routinely synthesised, at temperatures around 1400°C, by conventional solid-state routes[10], but such high temperatures can lead to sintering of the particles and consequential loss of their nanosize properties. Several wet-chemical methods have been employed, such as coprecipitation[7], sol-gel techniques[11, 12], microemulsions[11], oxidation techniques[13], microwave[14] and batch hydrothermal syntheses[15, 16]. These methods have overcome the problem of sintering. However, some involve the use of toxic organic compounds: sol-gel and microemulsion techniques require the use of large amounts of organic solvents or the addition of surfactants. In the

coprecipitation method, the pH of a metal salt is raised by adding a base to precipitate metal hydroxides, thus requiring strict control of pH and stirring rate. In most of these cases, the product requires further processing of some kind, such as ageing, calcination or hydrothermal treatment to allow dehydration and give greater crystallinity.

Batch hydrothermal syntheses of iron oxide compounds have been common: published work includes the hydrothermal production of hematite[17-19], magnetite[9, 17, 18, 20] and metal ferrites[8, 9, 15, 16, 21, 22].

## Previous work in Nottingham

An earlier version of Rig 1 was used in Nottingham by Dr. Albertina Cabañas to form iron-containing nanoparticles[1]. Hydrothermal decomposition of metal acetate solutions led to the formation of samples of magnetic spinel-type compounds, such as magnetite ($Fe_3O_4$), several ferrite compounds with formula $MFe_2O_4$ (where M = Co, Ni, Zn) and a mixed cobalt and nickel ferrite, $Ni_xCo_{1-x}Fe_2O_4$.

The reactor used a simple T-piece for mixing and incorporated a tube furnace downstream of this mixing point but was otherwise very similar to Rig 1. The other principal difference is that Cabañas used nanopure water, through which nitrogen gas had been bubbled, in order to remove almost all dissolved oxygen. The experiments in this Thesis used deionised water, which had not been further treated in any way.

In Cabañas' work, experiments were performed with iron acetate alone over a range of mixing-point temperatures of 200°C-345°C, and at 25 MPa pressure. The $Fe_3O_4$ particles formed had sizes of 40-92 nm, as estimated from PXD data, using the Scherrer equation. A batch hydrothermal reaction was also

performed at 380°C and 33 MPa, which gave $Fe_3O_4$ with a significantly larger size of 158 nm.

Particles of iron were also detected in the PXD traces, with more intense signals, suggesting larger amounts, in samples made at higher temperatures. As has already been mentioned, Arai et al. had put forward the idea that metal oxide particles form through a hydrolysis reaction, to form metal hydroxide, followed by dehydration[17]. Reaction of iron (II) acetate might therefore be expected to form iron (II) oxide, FeO. There must be a further reaction step to form the magnetite observed in this reaction. Cabañas et al. suggested that a further disproportionation to form magnetite and elemental iron might occur[1]:

$$4FeO \rightarrow Fe + Fe_3O_4$$

and an overall scheme for the reaction was presented thus:

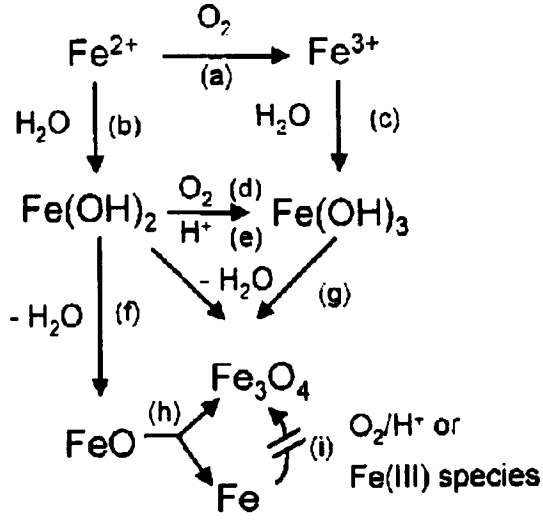


In this scheme, the change of oxidation of the iron from $Fe^{2+}$ to $Fe^{3+}$ takes place before (step a), or after (step d), the hydrolysis step (b or c). $Fe_3O_4$ is then formed by either (f) dehydrating $Fe(OH)_2$ to from FeO followed by (h) disproportionation or (g) the dehydration of a combination of $Fe^{2+}$ or $Fe^{3+}$ hydrolysed species.

Temperature was found to affect product distribution, with less metallic iron produced at higher temperatures. This was attributed to the fact that step (f) in the scheme above is exothermic, whilst step (g) is endothermic. As a consequence, at higher temperatures, the mechanism is more likely to proceed via step (g) than step (f), therefore avoiding the formation of metallic iron. In addition, at the higher temperature, the water in the reactor is much less dense, so the residence time is far shorter (ca. 5 s) than at the cooler temperature (ca. 25 s). This extra reaction time available at the cooler temperatures might allow the oxidation of Fe to $Fe_3O_4$ (step i).

It is presumably as a consequence of the partial removal of oxygen from the water that reaction of iron (II) acetate led to magnetite ($Fe_3O_4$), which contains a mixture of $Fe^{2+}$ and $Fe^{3+}$ ions, and not hematite ($Fe_2O_3$), the more oxidised compound, which contains only $Fe^{3+}$ ions. The absence of dissolved oxygen allows only the partial oxidation of the metal ions. As will be noted from later experiments, if water is used that has not been treated with nitrogen gas, the more oxidised hematite is formed.

In all of the syntheses, except that of the mixed nickel-cobalt ferrite, the particle size, estimated from PXD results was observed to increase significantly on increasing temperature from 300-400°C. In the case of the nickel-cobalt ferrite, a small decrease in size, too small to be deemed significant, was observed. TEM pictures revealed there to be a bimodal distribution of particles in all samples, consisting of small particles of 10 nm or less, and larger aggregates of up to 100 nm.

## Other syntheses

Outside of Nottingham, four groups have attempted the synthesis of iron oxide and ferrite compounds in flow reactors: those of Matson, Linehan and Bean at the Pacific Northwest Laboratory, USA; the group of Adschiri and Arai at

Tohoku University, Japan; Cote and Teja from the Georgia Institute of Technology, USA; and lastly Rho and Park from the Korea Institute of Energy Research.

The Pacific Northwest group[23, 24] seem to have been the first to attempt the hydrothermal flow synthesis of $Fe_2O_3$, giving the method the title RTDS (rapid thermal decomposition of precursors in solution). They used 0.1 mol $dm^{-3}$ solutions of iron (III) nitrate or ammonium iron (III) sulfate that were pumped under pressure through a 90 cm-long heated tube. The pressure was released as the product mixture was sprayed through narrow pipes at the end of the reactor. Reactions were performed at temperatures (measured at the reactor exit) in the range 225-400°C, and at 48-55 MPa pressure. The precursor mixture in this reactor would be heated slowly along the length of the heated tubing, whereas in the reactor designs used by other groups, a method for rapid heating was found. Nevertheless, small particles seem to have been made, in the range 10-60 nm (from PXD analysis).

It would appear that the Tohoku University group conceived of their hydrothermal flow method independently, without knowledge of the work in America, and published their first work at a similar time[25]. They performed the synthesis of the mixed oxide, barium hexaferrite ($BaO.6Fe_2O_3$) in a flow apparatus[21], similar in design to that eventually used in Nottingham (which, of course, was suggested by the original Japanese design).

The reaction mixture[21], unlike in the Nottingham design, is heated by two successive injections of hot water into the flow, as opposed to one, and the mixture is kept hot for a residence time of ca. 60 s. The conditions used were 400°C and 30 MPa. Whilst PXD was used to ascertain that a single phase was made, it seems that no attempt was made to determine the particle sizes.

The team from the Georgia Institute of Technology, Cote (née Holm) and Teja, published a synthesis of $MnFe_2O_4$ in a near-critical water flow reactor[9]. Nanoparticles were made using a precursor mixture of iron (III) nitrate and manganese (II) nitrate, with sodium hydroxide being added within the rig.

The Cote-Teja group later went on to publish a synthesis of $CoFe_2O_4$, again using iron (III) nitrate, but this time also with cobalt (II) nitrate[26, 27]. Without using sodium hydroxide, $Fe_2O_3$ was produced, but not $CoFe_2O_4$. With addition of base, the cobalt ferrite was produced as intended. Different rig configurations allowed the base and metal salts to be mixed either cold (before heating) or hot (after heating). It was observed that with cold mixing, there was much less unwanted $Fe_2O_3$ present in the product than with the hot-mixing regime.

Lastly, Rho and Park, from the Korean Institute of Energy Research, have published a supercritical flow synthesis of barium hexaferrite[28]. Their methods employed a rig similar to that of the Arai-Adschiri group, and used a precursor mixture of barium nitrate and iron (III) nitrate. Base, in the form of potassium hydroxide was added to promote hydroxide formation.

## *Objectives*

The aims of this work were as follows:

1. To test the feasibility of making iron oxide nanoparticles, particularly $\gamma$-$Fe_2O_3$, in the hydrothermal flow reactor.

2. To find a practicable precursor concentration for reliable function of the rig.

3. To assess the effect of different reaction temperatures upon

a. conversion – by atomic absorption (AA) analysis of unreacted, soluble precursor in the product suspension

b. crystalline phase – by PXD pattern analysis

c. particle size – primarily by use of PXD and the Scherrer equation, but also by transmission electron microscopy (TEM), which will allow an analysis of the distribution of particle sizes

d. morphology and crystallinity of particles – by examining TEM photographs

## *Results and discussion*

Unless otherwise indicated, experiments in this chapter were performed using Rig 2, which incorporated the new mixing nozzle design (see Chapter 2).

### Preliminary experiments

At first, it was necessary to find a practicable precursor concentration for the formation of iron oxide. Initial experiments were performed using a 0.2 mol $dm^{-3}$ solution of iron (III) nitrate, and a mixing-point temperature of 300°C (necessitating the main water heater to be kept at 400°C), with pressure 260 bar. On reaction of the material, rust-red particles were observed to emerge from the rig, suggesting the formation of $Fe_2O_3$. However, it became clear that this concentration of reactants, whilst it had been perfectly adequate for the ceria and ceria-zirconia experiments, was too great for sensible running of iron oxide experiments.

At the high reactant concentration, occasional partial blocking of the rig occurred, but a far greater problem was the way that the particles affected the back-pressure regulator. The 260 bar pressure was not being held reliably, and whilst the pressure could be maintained when running clear water through the

apparatus, as soon as particles were being formed, the pressure began slowly to descend, and manual adjustment of the regulator had no effect.

An iron (III) nitrate concentration of 0.05 mol $dm^{-3}$, one quarter of the original, was then tested. After this reduction in precursor concentration, blockages almost never occurred, the back-pressure regulator very rarely stopped working, and the pressure was reliably maintained over the course of many experiments.

## Conversion calculation using atomic absorption (AA)

When deciding upon a method for quantifying conversion, it was necessary to find a technique that was relatively quick to perform, was readily available for frequent use, and was reliable and reproducible.

Simply drying and weighing the sample would lead to an extremely inaccurate value for the conversion, as it would be difficult to know how much of the solid sample consisted of product, and how much of precursor, and also difficult to tell how much material had been left behind inside the reactor.

However, if the insoluble iron oxide particles were separated from the crude product suspension, the concentration of soluble iron nitrate precursor within the liquid could be measured, and give a very good indication of how much of this precursor reacted in the rig. Titration would be a very time-consuming way of measuring this concentration. Much more straightforward, and possibly less prone to experimental error, is the use of atomic absorption.

As the concentration of the precursor going into the reactor (0.05 mol $dm^{-3}$) was known, as were the approximate flow rates of metal-salt solution (5 ml $min^{-1}$) and water (10 ml $min^{-1}$), a value for the expected concentration of dissolved iron in the reactor product, if there were no conversion, is obtainable.

This value can then be compared with the actual concentration of iron to work out the percentage of conversion.

Analytical standards with concentrations of 5, 10 and 25 ppm in iron were prepared. For AA analysis, the solid particles would have to be removed, and the concentration of iron brought down to ca. 10 ppm. Firstly, a sample of 20 $cm^3$ was removed from the product suspension. To this was added 2 $cm^3$ of concentrated nitric acid, which would cause the iron particles to settle, just as it caused the ceria particles to settle in Chapter 5. For high-conversion samples, the concentration of iron in the product was already low enough for AA analysis without further dilution. However, experiments with lower conversions required further dilution to bring the concentration of the iron in the sample down to ca. 10 ppm.

## Freeze drying of samples: a method for preventing particle agglomeration

It was thought that the oven-drying of samples might lead to the agglomeration of particles, and that this would lead to a reduction in surface area (although it would be unlikely to lead to an increase in crystallite size, as estimated from PXD and the Scherrer equation). Therefore, freeze drying was attempted, as an alternative method of drying. The product suspensions were frozen inside round-bottomed flasks, using liquid nitrogen. These flasks were then attached to the freeze-drying apparatus, which greatly reduced the pressure in the system, whilst gently warming the samples. At these low pressures, the frozen water would not melt and then evaporate, but rather sublime. This would avoid the presence of liquid water, and hence avoid surface tension, which in turn would prevent the collapse of the structure of the suspension as the water evaporates and agglomeration of particles. This was hoped to allow the retention of high surface area in the solid particles.

The dry powder was also submitted for PXD analysis, in order to identify the phase of iron oxide present. In all cases, the phase was found to be $\alpha$-$Fe_2O_3$ which, whilst not perhaps the form of iron oxide that had been originally intended, nonetheless found a useful application, as will be seen towards the end of this chapter.

## Transmission electron microscopy (TEM) investigations

TEM can provide extra information about particle sizes that PXD cannot. TEM allows the determination of the sizes of particles that are made from agglomerations of many crystallites, whilst PXD gives the approximate crystallite size. Also, PXD gives a value for the average crystallite size, whereas TEM allows the measurement of the size of individual particles within the area covered by a micrograph, and evaluation of the particle-size distribution. TEM was used in some of these experiments to acquire the particle-size distribution.

## Analysing two samples made at high and low reaction temperatures

Two samples of particles were produced from 0.05 mol $dm^{-3}$ iron (III) nitrate at 260 bar. One was produced with the rig at a high temperature (300°C) and the other at a low temperature (100°C). According to the discussion in Chapter 2, temperature was expected to have an effect upon particle size. In Chapter 5, an increase in cerium dioxide particle size was observed with increasing reaction temperature, so this was also expected to be observed for iron oxide.

There was a clearly-visible difference between the two samples: the high-temperature sample contained rust-red, opaque particles that settled from solution without further treatment; the low-temperature sample contained a deep-red, transparent suspension, which, upon addition of acid, as used for

ceria-particle suspensions in Chapter 5, settled and became rust-red particles, which resembled those of the high-temperature sample.

It was therefore strongly suspected that the samples contained the same chemical substance ($Fe_2O_3$) but with different particle properties. TEM was used to analyse each of the two samples.

A small portion of each sample was taken and dried onto a copper TEM grid. The samples were examined using a Tecnai F20 Microscope with 200 kV voltage, in bright-field mode.

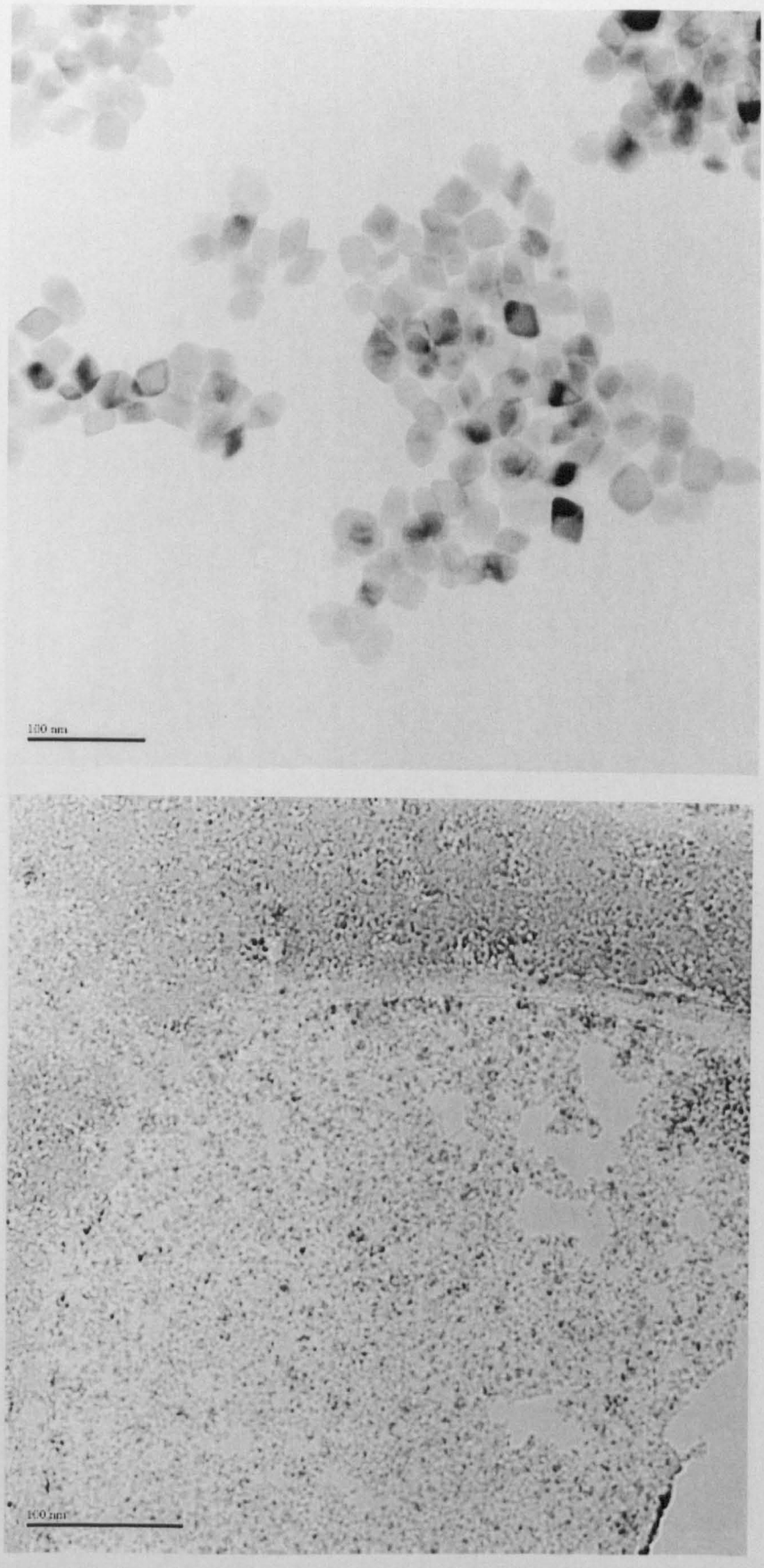


**Figure 6.3: TEM pictures of iron oxide particles synthesised at 300°C (above) and 100°C (below), showing that particles made at the higher temperature are very much larger than those made at lower temperatures. (scale bars indicate lengths of 100 nm)**

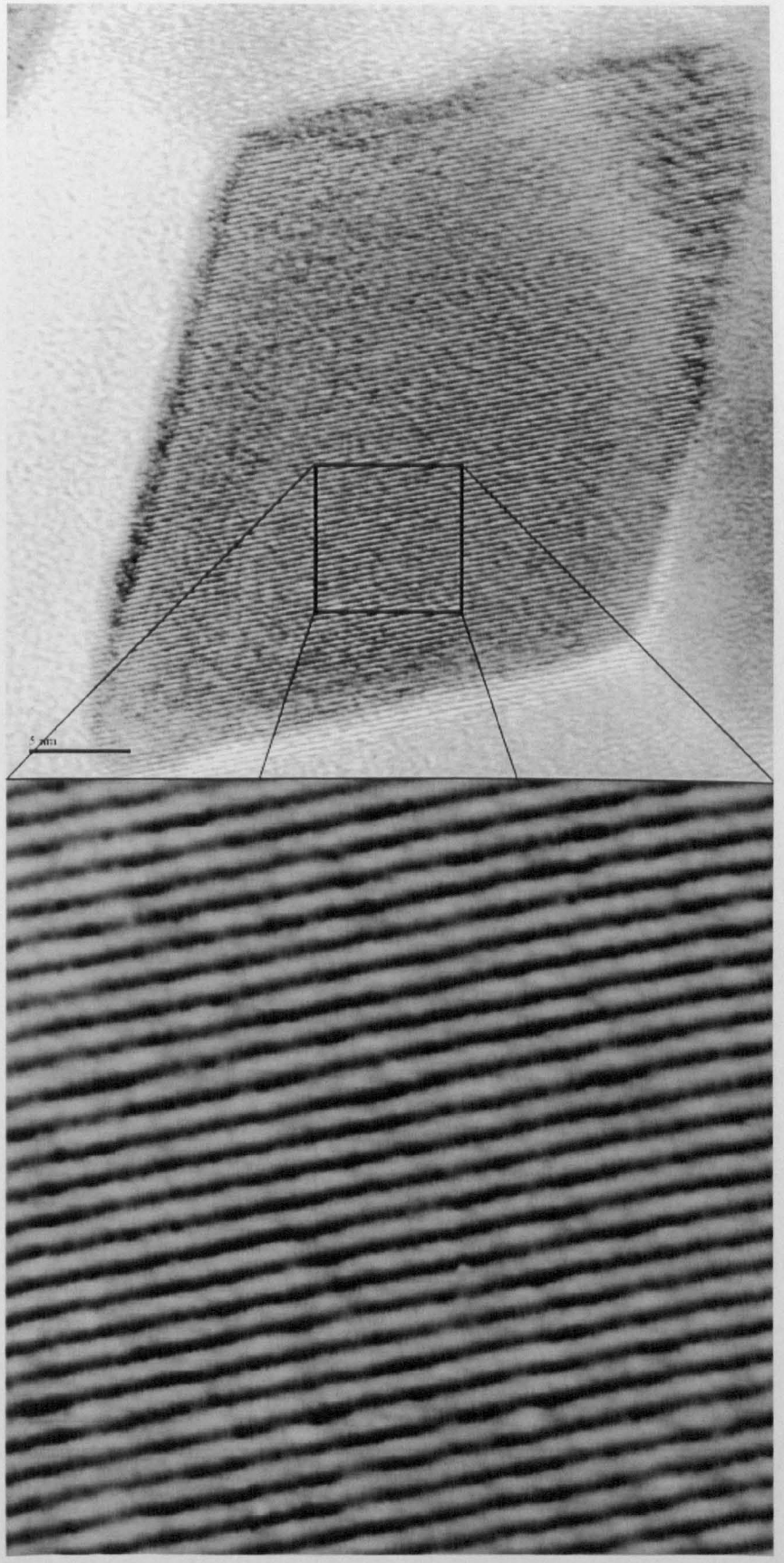

**Figure 6.4: TEM picture at high magnification (scale bar indicates 5 nm) showing how the high-temperature sample consists of large, faceted, particles which, when enlarged by computer (inset), show lattice fringes, giving evidence of high crystallinity.**

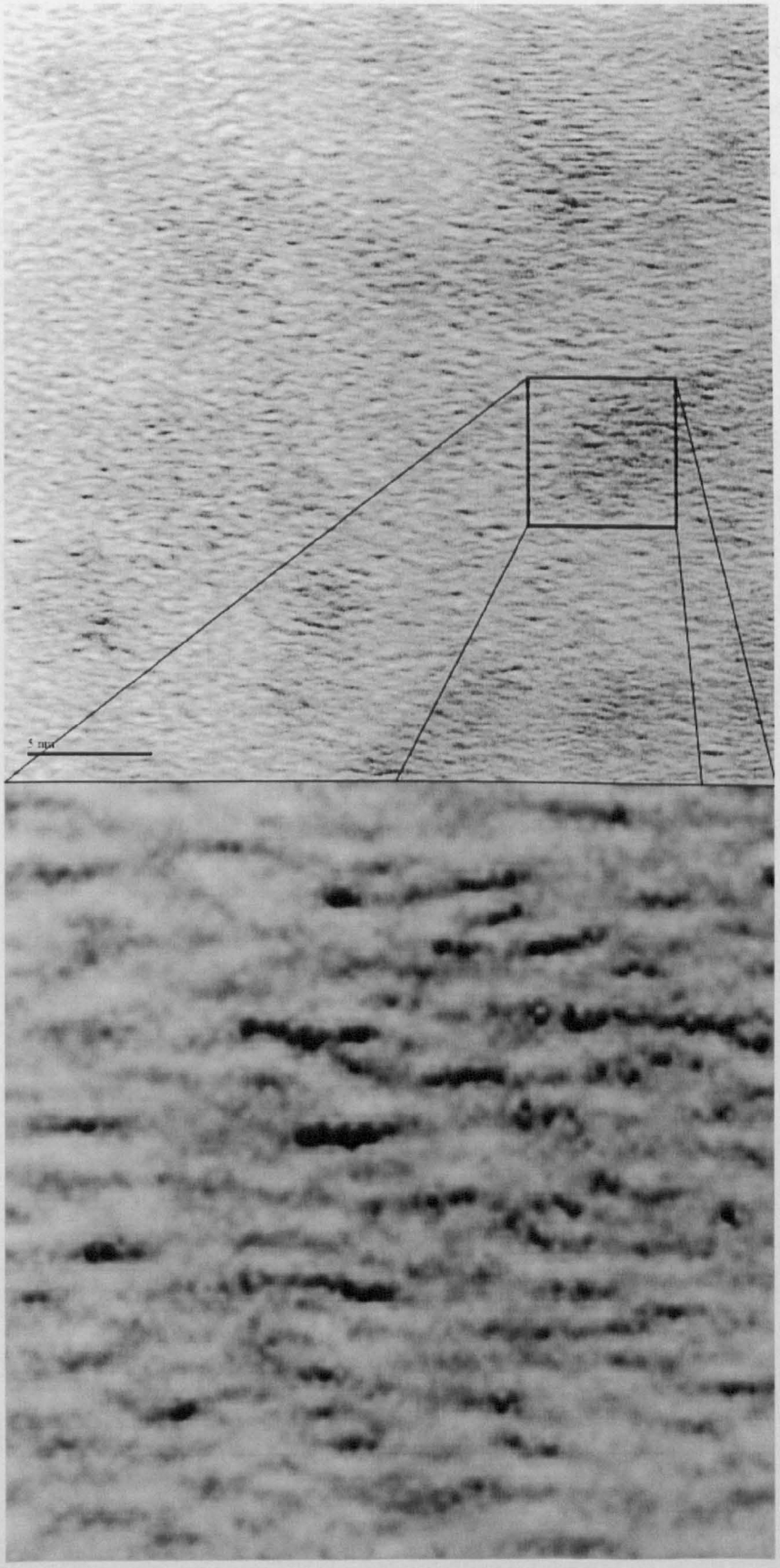

**Figure 6.5: TEM picture at high magnification (scale bar indicates 5 nm) showing how the low-temperature sample consists of small, mostly amorphous. Magnification of the image by computer (inset) shows some lattice fringes arising from small regions of crystallinity.**

Figure 6.3 provides a comparison of TEM images of the high-temperature sample (above) and the low-temperature sample (below). The high-temperature sample can be seen to contain particles that are faceted and crystalline, with particles typically 17-50 nm across. The striking feature of the low-temperature sample was the much-reduced size of the particles and the lack of crystallinity. The particles ranged from 2-7 nm across.

Figure 6.4 shows a higher-magnification TEM of the high-temperature sample. The faceted crystals contained within the sample are clearly visible and, on closer inspection (in the inset), lattice fringes become visible, providing further proof of the highly crystalline nature of the sample.

Figure 6.5 shows a high-magnification TEM of the low-temperature sample. Few lattice fringes, and hence very little crystalline order, were observed. The inset shows a more magnified section showing some signs of lattice fringes, revealing the presence of some crystallinity within the largely amorphous sample.

These TEM images provided the strongest evidence so far that we have control of particle sizes through control of reaction temperature. It seems that at lower temperatures, the rate of agglomeration, as discussed in Chapter 2, is low enough that the product will not contain well-defined crystals, but rather primary particles that have nucleated and grown a little, but not agglomerated.

## A series of experiments to test the effect of temperature change upon particle size and conversion

It has already been established above that synthesis of iron oxide at 300°C produces significantly larger particles than synthesis at 100°C. It was thought interesting to investigate the point at which this transition occurs, and to use

the AA method for determination of the conversion, observing how this relates to temperature.

To this end, experiments were performed at a range of temperatures, 100-400°C, 250 bar and with the usual pump rates of 5 ml $min^{-1}$ for the 0.05 mol $dm^{-3}$ iron (III) nitrate solution, and 10 ml $min^{-1}$ for the water flow.

300°C was the highest mixing-point temperature that can be maintained on Rig 2. In order to test the effects upon iron oxide formation of supercritical temperatures, a similar set of experiments was performed on Rig 3 by Paul Blood, but over the temperature range of 150-400°C, which was made possible by the use of a more powerful heater. This allowed some comparison between products from Rig 2 and Rig 3.

The iron oxide particle component was removed from a sample of crude reactor product for each experiment; the liquid component was then analysed for iron content by AA, and the conversion calculated, using the method described above. The remainder of each sample from those experiments performed in Rig 3 was taken for analysis by TEM.

On visual inspection of the samples, it could be seen that there was a fairly sharp transition between samples that consisted of the deep-red suspension (representing smaller particles, as discussed above) and those that formed a rust-red, opaque suspension of larger particles. This transition occurred at ca. 280°C in the case of samples made in Rig 3, and at ca. 250°C in the case of particles made in Rig 2. This can be observed from the photograph displayed in Figure 6.6.

The discrepancy in the transition temperature between rigs is likely to be caused by the thermocouples within the reactor not sampling the temperature at quite the same point in the rig. The mixing pieces contain very steep

temperature gradients, where the cold stream meets the hot stream, so even small discrepancies in thermocouple position between the rigs could lead to inconsistencies, and recorded temperatures much lower than the true mixing temperature.

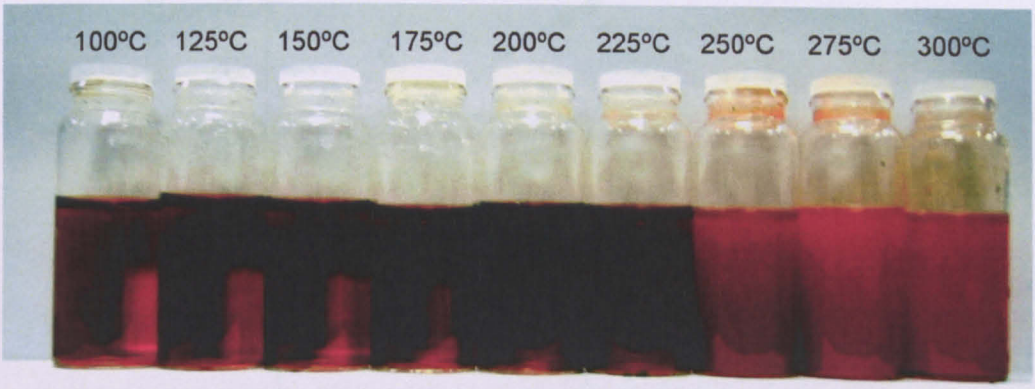


**Figure 6.6: unprocessed products from a sequence of experiments (performed on Rig 2) at a range of temperatures, increasing left-right, showing the transition between the deep-red, clear suspension made at low temperatures, to the rust-red, opaque material made at higher temperatures, in the three right-most vials. The lowest temperature to produce the opaque, orange samples was 250°C**

Analysis by AA to determine the conversion in the experiments, performed on Rigs 2 and 3, revealed, as was expected, a very strong dependence of conversion upon reaction temperature. As can be seen from Figure 6.7, very low conversions were observed at the lowest temperatures (approximately 5% at 150°C in Rig 3), whilst at the highest temperature, near 100% conversion was achieved. This suggests that at lower temperatures, the rate of crystal growth is insufficient to allow very much of the solute to be consumed, and therefore leads to small, only partially crystalline, particles. The graphs of conversion in each rig are very similar, albeit offset by ca. 100°C, as demonstrated in the second graph where data set A is shifted 100°C to the right. This provides yet more evidence that there was a discrepancy in temperature measurement between the two machines.

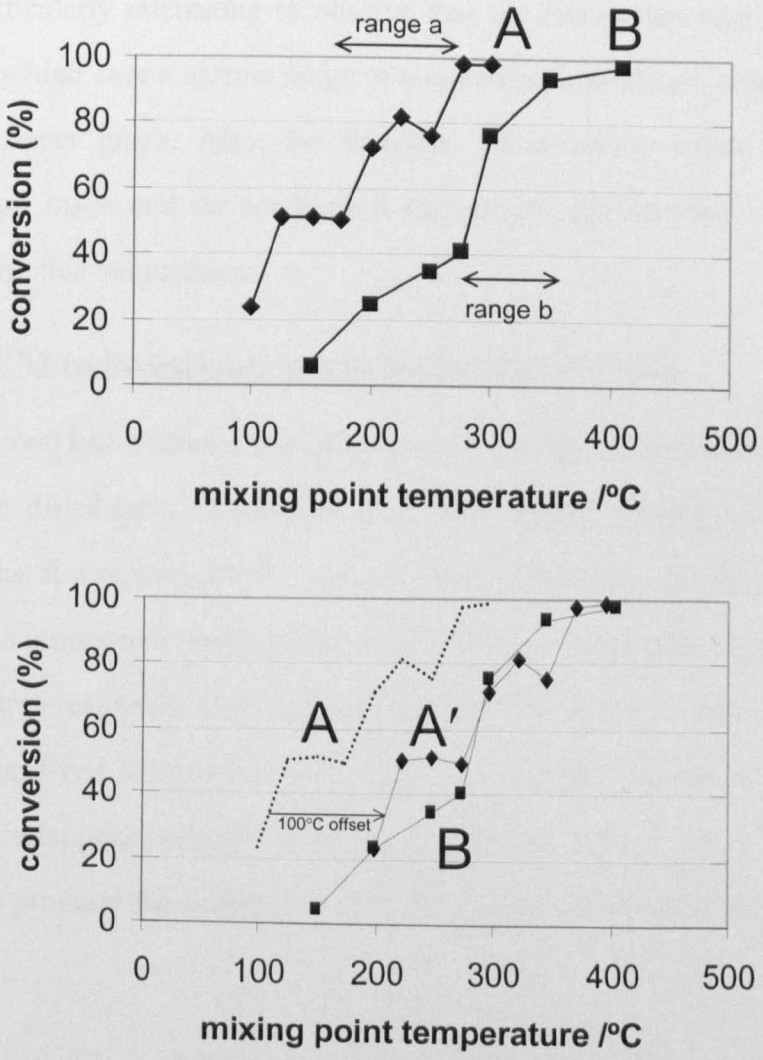


**Figure 6.7: a comparison of conversions for iron oxide reactions at different temperatures using data from Rig 2 (series A, ◆) compared with that from the supposedly similar Rig 3 (series B, ■). These two graphs are observed to be quite similar to one another, but offset. The graphs can be made to almost coincide, as can be observed on the second graph, when the A graph is moved to the right by 100°C to become graph A′. This offset is most likely to be due to a discrepancy in measuring the mixing-point temperatures between the two rigs. In addition, there is observed to be a steep increase in conversion through temperature ranges a and b on the graph. At temperatures above this range, significantly larger particles are observed to form than at lower temperatures.**

It was particularly interesting to observe that the conversion rose from very low to very high over a narrow range of temperatures, marked by ranges a and b on the upper graph. Also, the transition point, above which the larger particles are made and do not form a suspension, can be seen to coincide roughly with this temperature.

## Using TEM to investigate particle-size distribution

Dr. Paul Blood had written a MatLab routine to partially automate the analysis of the size distribution of particles in a TEM image. Having obtained the micrographs, it was necessary to trace a sample of particles, by hand, in black marker on a transparent acetate sheet. Firstly, this provided high-contrast edges for the routine to detect, in comparison to the low-contrast edges in the raw TEM image. Even more importantly, this also allowed a human to locate the edges of overlapping particles in the TEM, which would have been extremely different to program the computer to do. The tracings were then scanned into a computer.

Once the routine had identified the particle diameter of every particle traced from the TEM images, values were rounded to the nearest nanometre, and the frequency of particles with each size, within each sample, was determined. These results are presented in Figure 6.8, and show that the particles formed at low temperatures have a very narrow size distribution, and are smaller, whilst those at higher temperatures have a much broader size distribution, and are bigger. Figure 6.9 summarises the data in Figure 6.8, and marks the mean particle size and one standard deviation either side of it. The considerable broadening of the distribution at higher temperatures becomes very obvious.

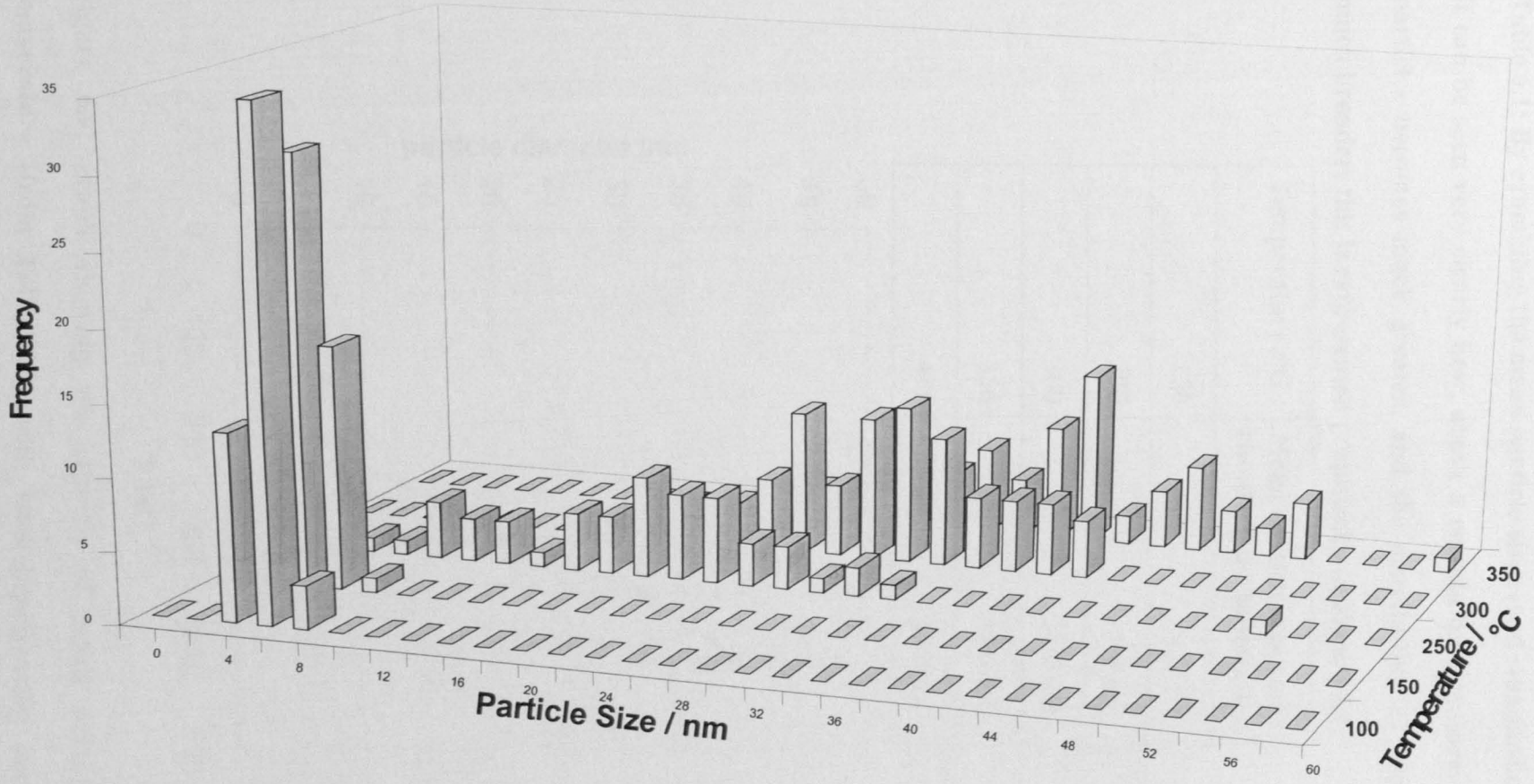


**Figure 6.8: the distribution of particle sizes in samples made at the lowest temperatures in Rig 3 are seen to be narrow and centred on 6 nm; the distributions for samples made at higher temperatures is much broader with mean 20-40 nm depending on temperature.**

**Table 6.1: By examining the mean particle sizes (and standard deviations), it can be seen very clearly how, above a certain temperature, the size of particles becomes much greater, and the distribution of sizes becomes much broader; this is represented graphically in Figure 6.9.**

| Temperature /°C | Mean particle size (with standard deviation) /nm |
|---|---|
| 150 | 6.5 ± 1 |
| 200 | 5.9 ± 1 |
| 300 | 21.0 ± 9 |
| 350 | 32.0 ± 6 |
| 415 | 39.9 ± 7 |

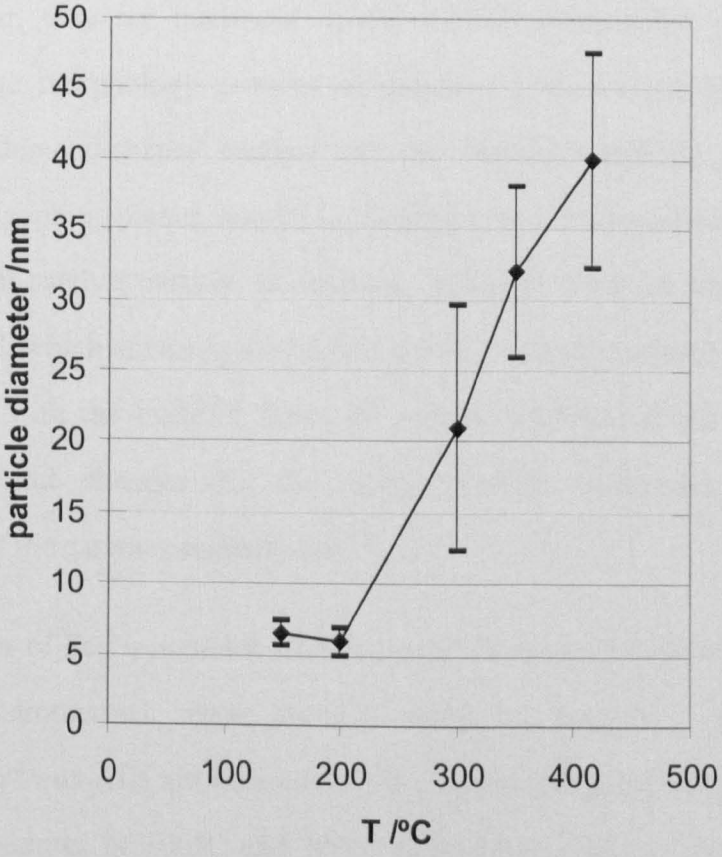


**Figure 6.9: graph showing the relation of mean particle size to temperature (from Table 6.1), with bars representing one standard deviation either side of the mean indicating the greatly increased spread in data at higher temperatures.**

## Growing graphitic nanofibres on $Fe_2O_3$ particles

Carbon nanotubes (CNT) and graphite nanofibres (GNF) have found use as electrically conductive fillers in polymer composites and as lubricants, as well as, amongst other applications, hydrogen storage materials[29]. However, to make the use of these materials commercially viable, it is necessary to be able to control their functional properties, morphology and yield.

Hannah Edwards and co-workers, from the University of Nottingham School of Mechanical, Materials and Manufacturing Engineering (SMMME), have been investigating the control of nanofibre growth using chemical vapour deposition (CVD) upon particles of $Fe_2O_3$ catalyst.

In particular, they are interested in the control of nanofibre morphology. Herring-bone morphology consists of graphitic planes organised as cones around a diamond-shaped catalyst particle; platelet nanofibre morphology consists of graphitic planes, normal to the long axis of the nanofibre emanating form an oval catalyst particle. In addition, multiwall nanotube structures may be produced, which are associated either with a rounded, encapsulated catalyst particle, or with the exposed facets of a clean catalyst particle[30]. Also of interest are the changes that the catalyst particle undergoes during the formation of the carbon nanoparticles[31].

Two samples of $Fe_2O_3$ particles were made by me in the School of Chemistry, in the hydrothermal flow reactor using a precursor solution of 0.05 mol $dm^{-3}$ iron (III) nitrate nonohydrate, a pressure of 250 bar and mixing-point temperatures of 100°C and 300°C respectively. As had been observed before, the particles made at the lower temperature remained in a deep-red, clear suspension, whereas those made at the higher temperature formed an opaque, rust-red suspension.

In addition to these samples, $Fe_2O_3$ particles were made by a simple precipitation method; iron nitrate was heated in a solution of aqueous ammonia to 100°C, with magnetic stirring. All of the particles were freeze dried.

Graphitic nanofibres were then grown upon the hematite particles by CVD in SMMME. Samples of catalyst were heated under argon to the reaction temperature of 500°C or 700°C. The samples were then exposed to a gas mixture of 80% $H_2$ and 20% $C_2H_4$ for one hour, before being allowed to cool once more under argon.

Analysis of the particles was carried out by a variety of methods: PXD on a Bruker D8 diffractometer, TEM on a Jeol 2000fx electron microscope, and high-resolution electron microscopy (HREM) on a Jeol 4000fx electron microscope. TEM samples were prepared on porous carbon film copper grids using a suspension of the powders in acetone, prepared by sonication for 3 min.

Figure 6.10 shows TEM images of the $Fe_2O_3$ particles used showing, as would be expected, how the particles produced by simple precipitation are considerably larger than those produced at a high temperature in the flow reactor (with a mean diameter of 20 nm), which in turn are larger, and more crystalline, than those produced at the lower temperature (with a mean diameter of 6 nm).

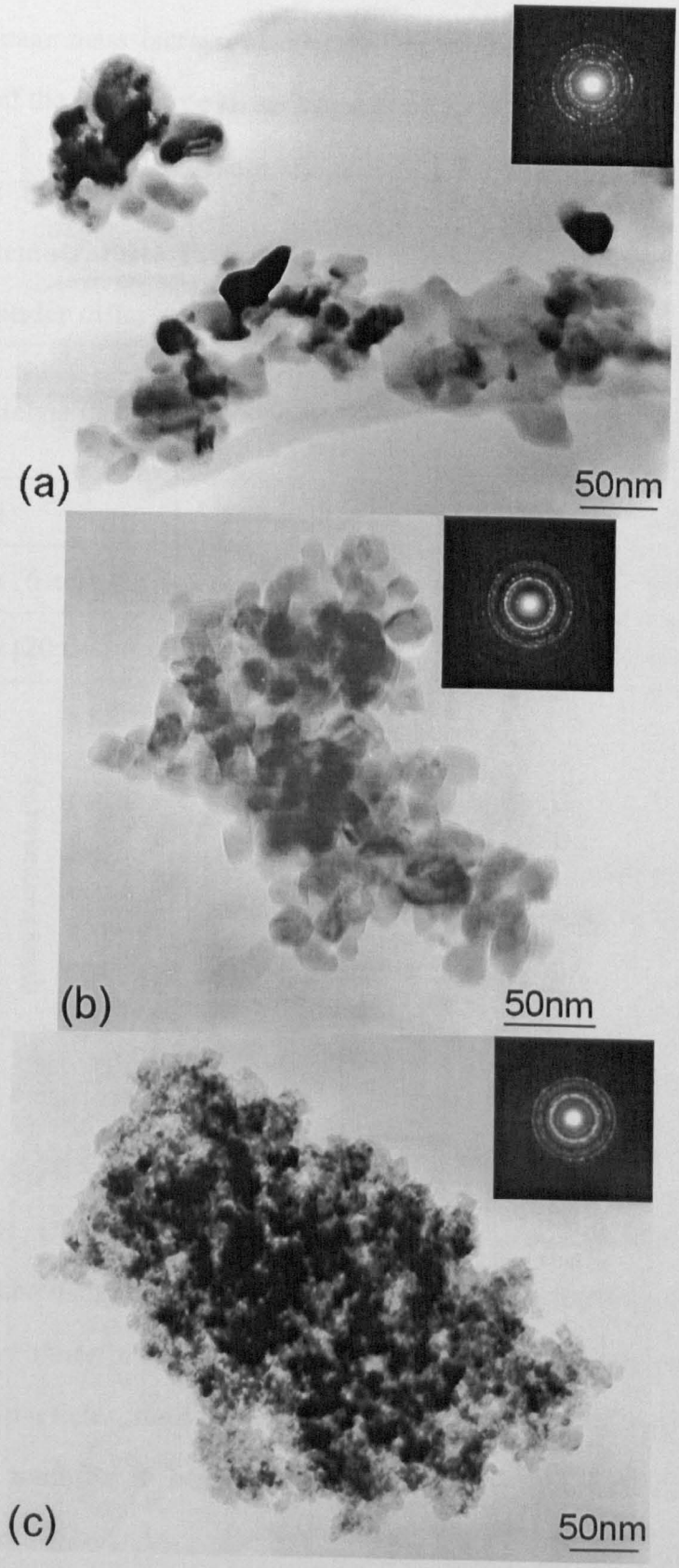


**Figure 6.10: TEM images showing $Fe_2O_3$ starting materials produced by (a) a simple precipitation route, and in the flow reactor at (b) 300°C (with mean diameter 20 nm) and (c) 100°C (mean diameter 6 nm).**

The percentage mass increase during the CVD process was calculated as an indication of the reaction yield, as indicated in Table 6.2 and Figure 6.11.

**Table 6.2: Percentage increase in mass during CVD reaction at two different temperatures to grow GNFs upon $Fe_2O_3$ particles that were produced under different conditions**

| $Fe_2O_3$ catalyst used | mass increase (%) | |
|---|---|---|
| | 500°C | 700°C |
| precipitated | 210 | 368 |
| flow reactor (6 nm) | 0 | 343 |
| flow reactor (20 nm) | 485 | 1033 |

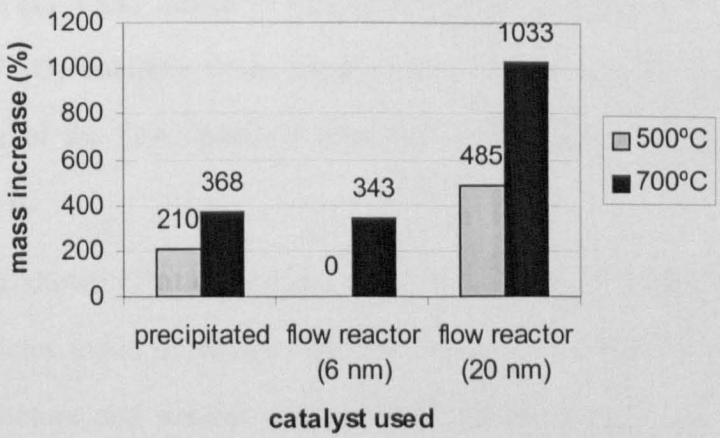


**Figure 6.11: Chart to illustrate the great increase in yield of GNF observed when using the $Fe_2O_3$ particles made by the 300°C hydrothermal method, over those prepared by standard precipitation techniques. Using the smaller particles, made at 100°C by the hydrothermal method, led to no carbon nanofibres being formed, except at the higher synthesis temperature.**

As can be observed from Figure 6.11, the larger $Fe_2O_3$ particles made by the hydrothermal flow method caused a graphitic nanofibre yield from the CVD process that far exceeded that provided by an $Fe_2O_3$ catalyst made by

conventional precipitation methods, whilst using the small particles led to no production of nanofibre particles at 500°C.

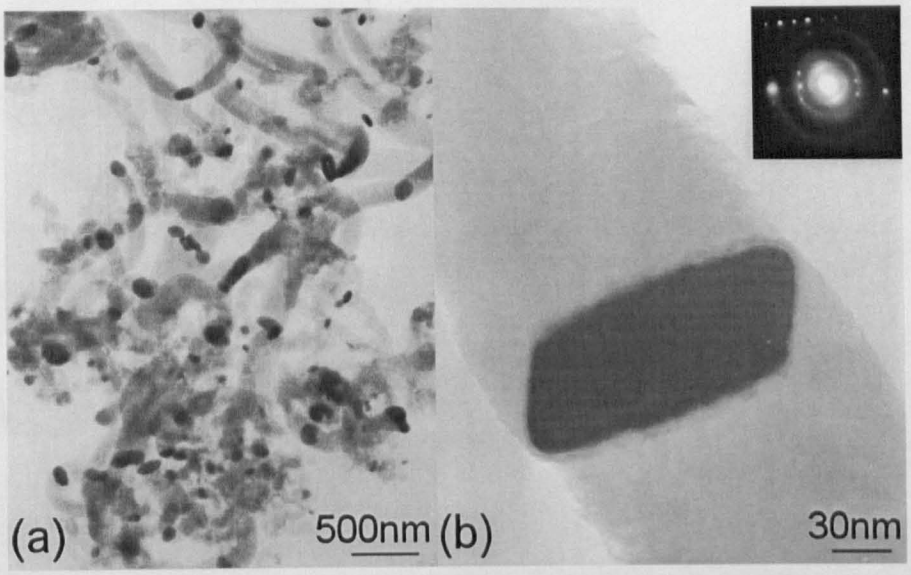


**Figure 6.12: (a) TEM image of GNFs produced by CVD at 500°C using the 20 nm $Fe_2O_3$ particles from the flow reactor (b) higher-magnification TEM image of an $Fe_3C$ particle and the herringbone GNFs that have grown upon it.**

Figure 6.12a shows GNFs produced at 500°C using the larger iron oxide catalyst particles made in the flow reactor. These fibres have a well-ordered graphitic structure and exhibit both platelet and herringbone morphologies, which are respectively associated with diamond- and oval-shaped single-crystal catalyst particles. Figure 6.12b shows two herring-bone fibres that have grown on a $Fe_3C$ catalyst particle. $Fe_3C$ is considered the product arising from initial reduction of $Fe_2O_3$ to Fe, and the final cooling down of Fe-C solid solution formed during GNF growth. The mean diameter of the nanofibres produced was 100 nm, whilst the yield was greater than that for the conventionally precipitated catalyst (see Figure 6.11). The high level of graphitic ordering within the nanofibres suggests that carbon deposition occurred as part of a steady-state growth process.

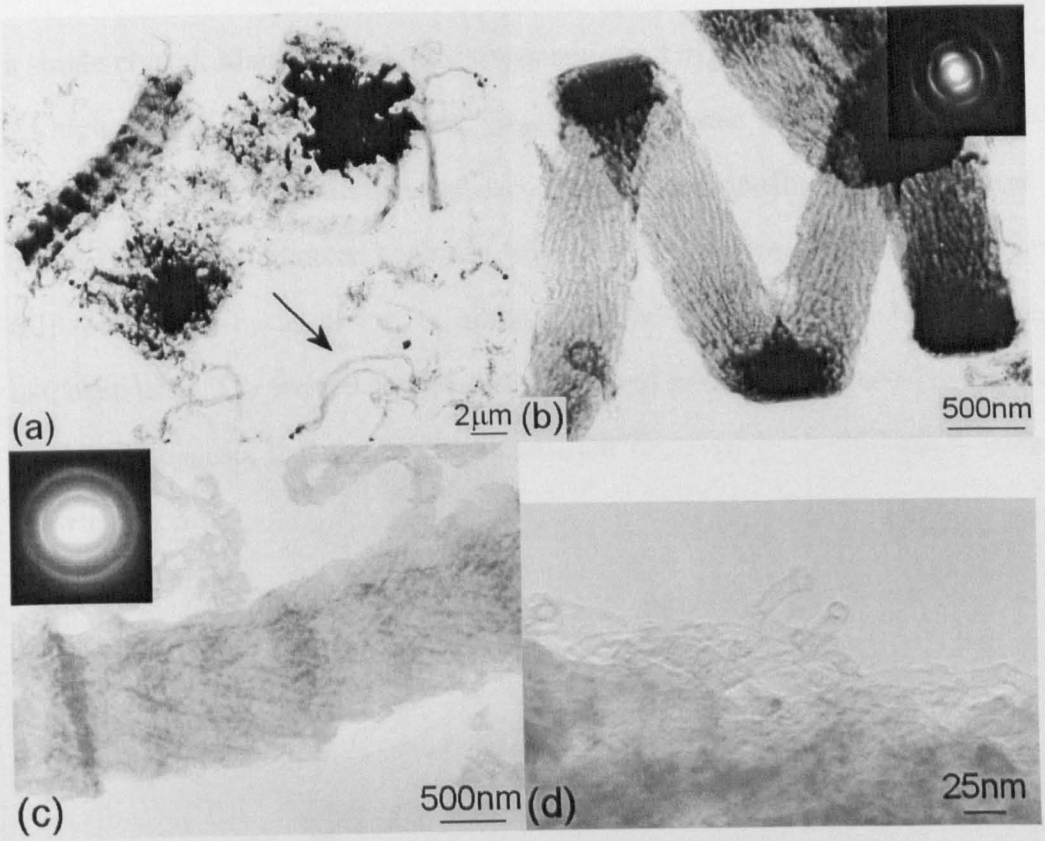


**Figure 6.13: (a, b) TEM images of GNFs produced by CVD at 700°C using the larger $Fe_2O_3$ particles from the flow reactor, showing the fibres to be less well ordered, with a broader size distribution, than those formed at a lower temperature; highly disordered chains of carbon shells were also observed (indicated by the arrow); (c, d) the larger fibres appeared striped and, at higher magnification, are revealed to consist of multiple graphitic domains, with multi-walled nanotubes at the nanofibre surface.**

Figure 6.13 shows images of the nanofibres produced by CVD at 700°C, using the larger iron oxide particles from the reactor as catalyst. The yield from these conditions was much higher than that produced using a conventionally precipitated catalyst (see Figure 6.11). However, the fibres produced were less well ordered, and had a considerably broader diameter distribution (500 nm - ca. 2μm). Large fibres exhibited a pseudo-platelet morphology, with graphite planes that were normal to the fibre-long axis. Fibres appeared to be growing on a cluster of small particles as opposed to the more usual growth on

a single crystal. Many of the larger fibres appeared to possess a striped texture. At higher magnification, however, these were revealed to consist of smaller graphitic domains with multiwalled nanotubes on the nanofibre surface (Figure 6.13c-d). Highly disordered chains of carbon shells were also observed (Figure 6.13a, indicated by an arrow, resulting from the high CVD temperature that had been used. The striped texture and disordered graphitic nature of the fibres produced suggests that the carbon deposition occurred by a non-steady-state growth process.

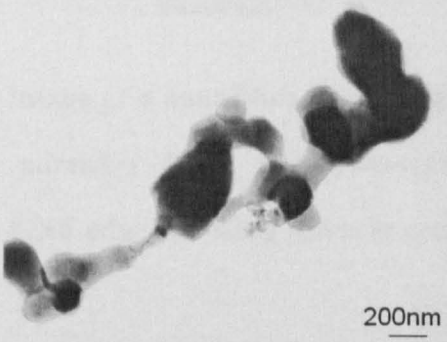


**Figure 6.14: TEM image showing how the $Fe_2O_3$ particles agglomerated following the attempted CVD at 500°C, whilst no GNFs were formed.**

No carbon deposition was observed during CVD at 500°C using the smaller iron oxide particles from the flow reactor. PXD investigations showed that the $Fe_2O_3$ had been reduced to Fe during the reaction. Figure 6.14 shows how the nanparticles agglomerated to form larger crystals. This intriguing result has yet to be explained.

Figure 6.15(a-b) show GNFs produce by CVD at 700°C using the smaller iron oxide particles from the flow reactor. The nanofibres produced were graphitically distorted, and adopted herring-bone and platelet morphologies, and a compound sub-structure. The high magnification image in Figure 6.15b shows distinct graphitic domains. Nanofibre dimensions were ca. 500 nm, and nanofibre yield was observed to be similar to that of a precipitated catalyst (see

Figure 6.11). As with the other particles made at 700°C, using the larger iron oxide particles, the GNF morphology suggests a non-steady-state growth process.

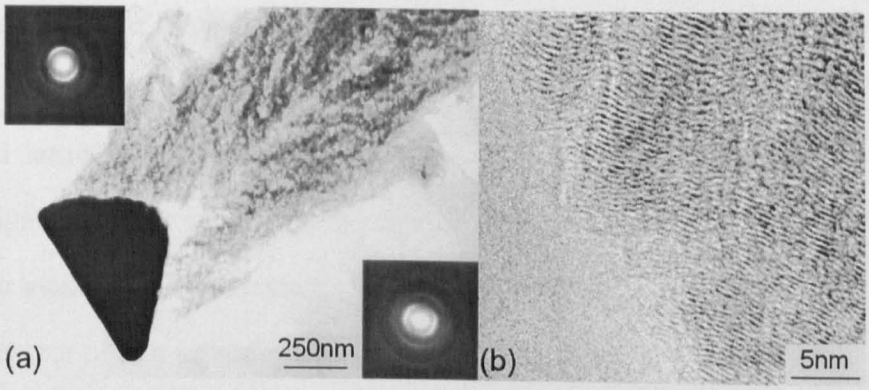


**Figure 6.15: a) TEM image of a nanofibre formed by CVD at 700°C using the smaller $Fe_2O_3$ particles from the hydrothermal flow reactor; b) HREM image of a GNF edge, showing discreet graphitic domains.**

## *Conclusions*

We conclude that it is simple to make $\alpha$-$Fe_2O_3$ using the hydrothermal flow reactor and deionised, but otherwise untreated, water. Good control of particle size has been achieved by adjusting the reaction temperature. Suspensions of particles made at low temperatures were noted to have a very different appearance from those of particles made at high temperatures. TEM analysis confirmed that the particles made at higher temperatures were larger and more crystalline than those made at lower temperatures, and also had a much broader size distribution. Finally, using the $\alpha$-$Fe_2O_3$ particles as a catalyst for the chemical vapour deposition of graphitic nanofibres showed that particles made by this method produced a greater number of nanofibres than those produced by conventional precipitation methods.

## Possible future work

Interest was expressed by the industrial sponsors of this project, Johnson Matthey, in the formation of $\gamma$-$Fe_2O_3$. During this Thesis, the formation of this

iron (III) oxide polymorph was not achieved. However, it is known from the work of Cabañas et al.[1] that, by bubbling nitrogen through the water and metal salt feeds before reacting, it is possible to form the less oxidised $Fe_3O_4$. It is stated[2] that $Fe_3O_4$ can be oxidised to form $\gamma$-$Fe_2O_3$, because the crystal structures of both compounds are similar, with each containing a cubic close-packed lattice of $O^{2-}$ ions. Further experiments involving iron oxide should investigate whether an adaptation of the hydrothermal flow synthesis can be used to make $\gamma$-$Fe_2O_3$ nanoparticles, with reduction occurring either within the flow reactor or in a separate stage afterwards.

## References


[1] A. Cabañas, M. Poliakoff, *J. Mater. Chem.* **2001**, *11*, 1408.

[2] N. N. Greenwood, A. Earnshaw, *Chemistry of the Elements*, 1st ed., Butterworth-Heinemann, Oxford, **1984**.

[3] D. F. Shriver, P. W. Atkins, C. H. Langford, *Inorganic Chemistry*, 2nd ed., Oxford University Press, Oxford, **1994**.

[4] L. B. Bragg, G. F. Claringbull, *Crystal Structures of Minerals*, G. Bell and Sons Ltd, London, **1965**.

[5] H. O. Jungk, C. Feldmann, *J. Mater. Res.* **2000**, *15*, 2244.

[6] R. Zboril, M. Mushlan, D. Petridis, *Chem. Mater.* **2002**, *14*, 969.

[7] T. Kodama, Y. Wada, T. Yamamoto, M. Tsuji, Y. Tamaura, *J. Mater. Chem.* **1995**, *5*, 1413.

[8] Y. Okano, T. Nakamura, *Colloids Surf. A: Physicochem. Eng. Aspects* **1998**, *139*, 279.

[9] L. J. Holm, A. S. Teja, in *5th International Symposium on Supercritical Fluids*, Atlanta, Georgia, USA, **2000**.

[10] S. Smit, H. P. J. Wijn, *Ferrites*, Gloeilampenfabrieken, **1959**.

[11] S. Hirano, T. Yogo, K. Kikuta, E. Asai, K. Sugiyama, H. Yamamoto, *J. Am. Ceram. Soc.* **1993**, *76*, 1788.

[12] T. Sugimoto, Y. S. Wang, H. Itoh, *Colloids Surf. A: Physicochem. Eng. Aspects* **1998**, *134*, 265.

[13] M. Kiyama, *Bull. Chem. Soc. Jpn.* **1978**, *51*, 134.

[14] H. Katsuki, *J. Am. Ceram. Soc.* **2001**, *84*, 2313.

[15] A. R. Gainsford, M. J. Sisley, T. W. Swaddle, *Can. J. Chem.* **1975**, *53*, 12.

[16] H. Kumazawa, K. Oki, H. M. Cho, E. Sada, *Chem. Eng. Commun.* **1992**, *115*, 25.

[17] T. Adschiri, K. Kanazawa, T. Arai, *J. Am. Ceram. Soc.* **1992**, *75*, 1019.

[18] T. Adschiri, S. Yamane, S. Onai, K. Arai, in *3rd Int. Symp. on Supercritical Fluids*, Strasbourg, France, **1994**.

[19] L. Diamandescu, D. Mihaila-Tarabasanu, N. Popescu-pogrion, A. Totovina, I. Bibicu, *Ceram. Int.* **1999**, *25*, 689.

[20] D. Chen, R. Xu, *Mater. Res. Bull.* **1998**, *33*, 1015.

[21] Y. Hakuta, T. Adschiri, T. Suzuki, T. Chida, K. Seino, K. Arai, *J. Am. Ceram. Soc.* **1998**, *81*, 2461.

[22] H. Kumazawa, H. M. Cho, E. Sada, *J. Mater. Sci.* **1993**, *28*, 5247.

[23] D. W. Matson, J. C. Linehan, R. M. Bean, *Mater. Lett.* **1992**, *14*, 22.

[24] D. W. Matson, J. C. Linehan, R. M. Bean, *Energy and Fuels* **1994**, *8*, 10.

[25] T. Adschiri, K. Kanazawa, K. Arai, *J. Am. Ceram. Soc.* **1992**, *75*, 2615.

[26] L. J. Cote, A. S. Teja, A. P. Wilkinson, Z. J. Zhang, *J. Mater. Res.* **2002**, *17*, 2410.

[27] L. J. Cote, A. S. Teja, A. P. Wilkinson, Z. J. Zhang, *Fluid Phase Equilib.* **2003**, *210*, 307.

[28] S. Rho, S. Park, *Korean J. Chem. Eng.* **2002**, *19*, 120.

[29] R. Baughman, A. Zakhidiv, d. H. W., *Science* **2002**, *297*, 787.

[30] S. Hong, Y. Shin, J. Ihm, *Jpn. J. Appl. Phys.* **2002**, *41*, 6142.

[31] J. Snoek, G. Froment, M. Fowles, *J. Catal.* **1997**, *169*, 240.

# Chapter 7: silver and cadmium sulfide

## *Summary*

Some success was achieved with experiments to make silver-metal particles, and cadmium sulfide quantum dots. In the case of silver, there was considerable contamination from other metals, and the experiments were difficult to repeat. In the case of cadmium sulfide, the toxicity of the reagents made the reaction rather inconvenient and hampered characterisation. Nonetheless, these experiments did show the potential for the hydrothermal flow method for synthesis of compounds beyond metal oxides.

## *Introduction*

Having discussed several examples of metal oxides made within the flow reactor, this chapter will discuss the formation of two other materials: a metal (silver) and another chalcogenide (cadmium sulfide).

The properties of metal and semiconductor nanoparticles are discussed in Chapter 1 so we shall deal here with alternative synthetic methods.

### *Silver*

Silver metal has a face-centred cubic structure (this is the same structure as copper metal – see Chapter 3). A review of synthetic methods for silver nanoparticles has been written by Evanoff and Chumanov[1]. Two traditional methods for making silver nanoparticles are the Lee-Meisel and Creighton methods. The Lee-Meisel method[2] involves the reduction of silver nitrate solution with sodium citrate to give a suspension of nanoparticles with a broad

range of sizes. The Creighton method[3] yields particles of ca. 10 nm with a narrow size distribution, and involves the reduction of silver nitrate with $NaBH_4$. Several adaptations of these methods have been used in which different silver salts or reducing agents are used[4-9].

Several silver nanoparticle synthesis methods which are significantly different from the Lee-Meisel and Creighton methods also exist. These include: silver particle synthesis through high-temperature reduction in porous solid matrices[10, 11], vapour-phase condensation of a metal onto a solid support[12-14], laser ablation of a metal target into a suspending liquid[15], photoreduction of $Ag^+$ ions[16, 17] and electrolysis of a silver-salt solution[18, 19].

Silver nitrate, reacted with formic acid, will form silver nanoparticles under hydrothermal conditions, according to the following reaction:

$$2AgNO_3 + 6HCOOH \longrightarrow 2Ag + 5H_2O + N_2 + CO_2$$

However, it was reported[20] that it was impossible to run the reactor even once without complete blocking.

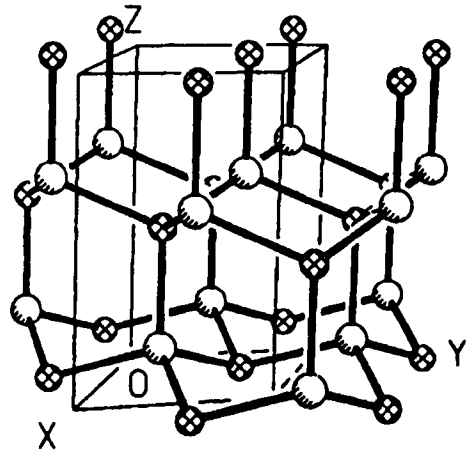


**Figure 7.1: Cadmium sulfide has a wurtzite crystal structure (reproduced from Mak et al.[21]).**

Cadmium sulfide has a wurtzite structure, as shown in Figure 7.1: sulfur atoms are arranged in a hexagonal close packed array in which one half of the tetrahedral holes are filled with zinc atoms. The possibility of tuning the size of particles by simple adjustment of reaction variables would be very useful if it could be applied to quantum dots. Ideally, pure, monodispersed, highly crystalline quantum dots could be synthesised[22].

There are two general approaches to quantum dot manufacture: "top-down" and "bottom-up". In the "top-down" approach, particles are lithographically or electrochemically etched from the material. This is expensive, requires specialised equipment and yields very little product. In the "bottom-up" approach, molecular or ionic precursors are reacted to produce a colloidal quantum dot suspension. However, this often yields non-crystalline products

with large size distributions, and precursors are often very toxic, air sensitive and expensive[23].

Bottom up methods include colloidal methods (whereby the growth of initial crystal seeds is controlled in an attempt to give monodisperse quantum dots[24]), and confined matrix methods (whereby quantum dots are formed in a restricted-growth environment, such as molecular sieves[25] or micelles[26]). However, the most popular method is using organometallic precursors (whereby a complex containing both the metal and chalcogenide is formed and rapidly pyrolised[27]). A small number of batch hydrothermal syntheses of CdS have been performed[28-31].

## Results and discussion

All experiments in this chapter were peformed in Rig 2, which incorporates the new mixing nozzle design (see Chapter 2).

### *Silver nanoparticles*

The revised nozzle design was used for this work. A solution with concentration 0.05 mol $dm^{-3}$ was used as feedstock. Instead of just water, the other feed was 0.11 mol $dm^{-3}$ formic acid solution. The regular flow rates of 10 ml $min^{-1}$ for the dilute acid, and 5 ml $min^{-1}$ for the salt solution; mixing-point temperature was 300°C. This gave an excess of 50% of formic acid at the mixing point, according to the above reaction. Particles were collected in the in-line filter and were analysed by BET and PXD.

According to the PXD results, silver particles with diameter of 53 nm were made. However, surface area, as measured buy BET, was high: 60 $m^2 g^{-1}$,

indicating a particle size of 9 nm. This discrepancy might be explained by the fact that estimating particle size from BET surface-area data assumes that the particles are smooth spheres. If particles have extremely rough surfaces, BET might yield a much smaller particle size than PXD.

STEM images of the particles, dusted on to a Cu TEM grid, were made. They were also subjected to EDAX analysis.

STEM revealed there to be three different particle morphologies present, as shown in Figure 7.2. These were identified, and are labelled as such, with the aid of EDAX, as follows:

(1) Large silver particles with diameters of up to 770 nm

(2) Ultrafine material, with a rough surface, consisting of particles of diameter 1-9 nm; this material consisted mainly of silver but also significant amounts of iron

(3) Flake-like regions, typically 150 nm in length, that contained silver and some iron

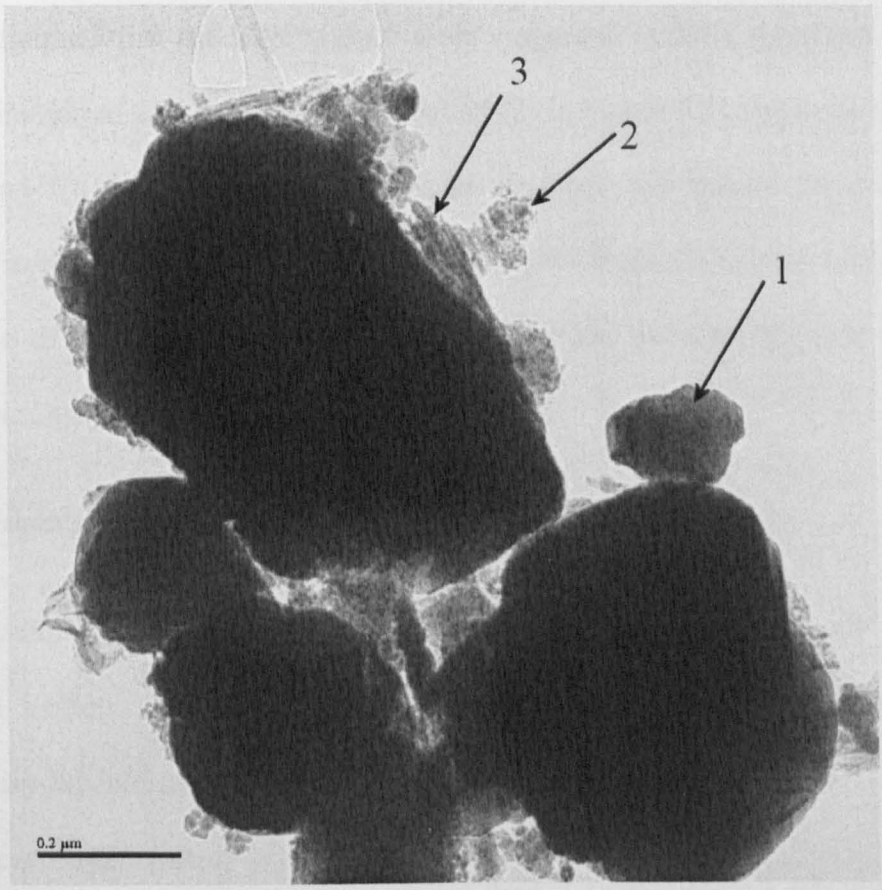


**Figure 7.2: the three different particle morphologies present in the silver sample – (1) large silver particles, (2) ultrafine silver/iron particles, (3) silver-iron flakes (scale bar represents 0.2 µm).**

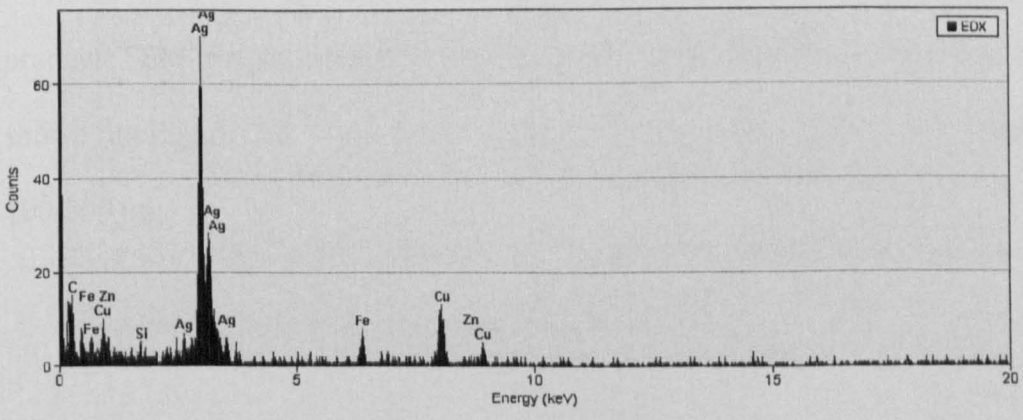


**Figure 7.3: EDAX analysis showing significant iron content in the supposedly silver particles. Also evident are impurities of Cu, Al, Si and Zn.**

It is assumed that the large surface areas suggested by BET were due to the contribution of the small particles (labelled (2) in Figure 7.3). Impurities of Al, Zn and Cu are thought to come from residues left behind by previous experiments, or, possibly, from leeching of iron from the reactor tubes. The source of the silicon is less clear, but may come from the glass in which reagents are kept.

***Cadmium sulfide***

The method employed for CdS particle synthesis was an adaptation of the batch hydrothermal synthesis used by Liu et al.[30]. Cadmium nitrate and thiocarbohydrazide – $SC(N_2H)_2$ – were reacted in a 1:1 ratio. Thiocarbohydrazide forms a complex with cadmium that decomposes under the reaction conditions to form CdS. An aqueous solution of concentration 0.025 mol $dm^{-3}$ in $Cd(NO_3)_2$, and also in $SC(N_2H)_2$, was prepared. No precipitation was observed from the cold solution.

Upon reaction, a suspension of bright-yellow CdS particles was collected as product. TEM images were recorded by Paul Blood to examine particle size, as shown in Figure 7.4. This figure shows particles with sizes in the range 100-200 nm.

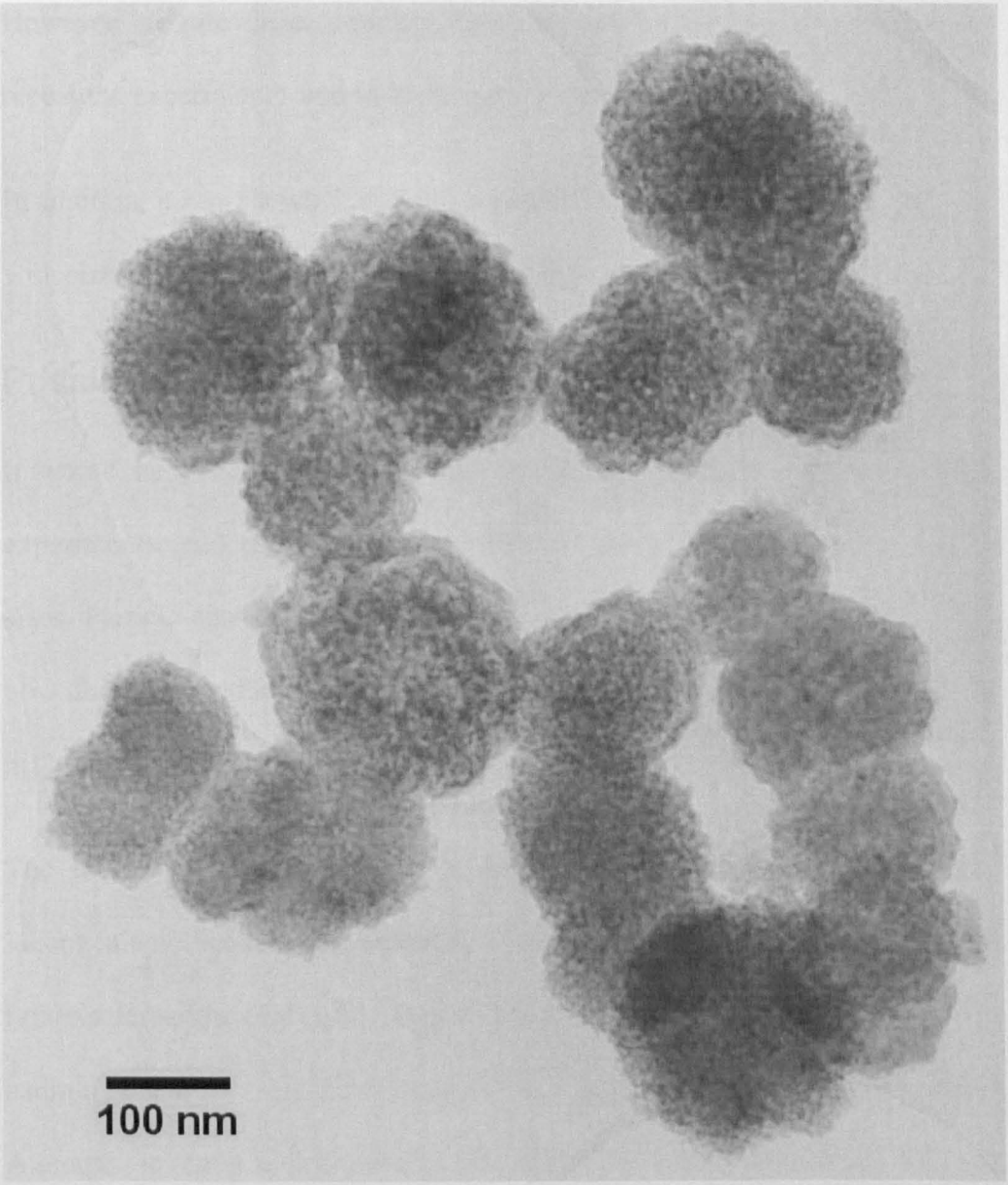


**Figure 7.4: TEM of CdS particles showing their size to be in the range of 100-200 nm (TEM performed by Paul Blood).**

## *Conclusions*

The principal achievement of this experiment is that silver nanoparticles were made without any blockages occurring. This was a significant step forward, and proof that the new nozzle design is far superior to a simple T-piece.

However, despite these initially promising results, it has been difficult to repeat the experiments, and to investigate improvements.

In addition, it was shown that it was possible to form cadmium sulfide particles with size 100-200 nm in the hydrothermal flow reactor.

## Possible future work

It would be very useful to be able to repeat the silver particle synthesis experiments, and test the effect of different temperatures upon the particle sizes. Particle size may be affected rather differently in this experiment from how they were affected in the oxide-formation experiments, owing to the different chemistry involved.

The toxicity of reagents used to form CdS made the synthesis method inconvenient. Future experiments to make CdS might employ thiourea as a rather safer sulfur-containing reagent. In addition, it might be possible to make cadmium selenide particles by reacting a cadmium salt with selenourea. Attempts to control the particle size might also be made using different reaction temperatures (although, as with silver, the chemistry differs from that in the oxide-formation reactions and particle size might be affected differently).

## References


[1] D. D. Evanoff, G. Chumanov, *Chemphyschem* **2005**, *6*, 1221.
[2] P. C. Lee, D. Meisel, *J. Phys. Chem.* **1982**, *86*, 3391.
[3] J. A. Creighton, C. G. Blatchford, M. G. Albrecht, *J. Chem. Soc.-Faraday Trans. II* **1979**, *75*, 790.
[4] N. Leopold, B. Lendl, *J. Phys. Chem. B* **2003**, *107*, 5723.
[5] X. L. Li, J. H. Zhang, W. Q. Xu, H. Y. Jia, X. Wang, B. Yang, B. Zhao, B. F. Li, Y. Ozaki, *Langmuir* **2003**, *19*, 4285.
[6] I. Sondi, D. V. Goia, E. Matijevic, *J. Colloid Interface Sci.* **2003**, *260*, 75.
[7] S. T. He, J. N. Yao, P. Jiang, D. X. Shi, H. X. Zhang, S. S. Xie, S. J. Pang, H. J. Gao, *Langmuir* **2001**, *17*, 1571.
[8] J. P. Cason, K. Khambaswadkar, C. B. Roberts, *Ind. Eng. Chem. Res.* **2000**, *39*, 4749.
[9] N. Shirtcliffe, U. Nickel, S. Schneider, *J. Colloid Interface Sci.* **1999**, *211*, 122.
[10] Y. Plyuto, J.-M. Berquier, C. Jacquiod, C. Ricolleau, *Chem. Commun.* **2002**, *17*, 1653.
[11] T. C. Wang, M. F. Rubner, R. E. Cohen, *Langmuir* **2002**, *18*, 3370.
[12] S. Z. Malynych, G. Chumanov, *J. Vac. Sci. Technol. A* **2003**, *21*, 723.
[13] Y. P. Zhao, D. X. Ye, G. C. Wang, T. M. Lu, *Nano Lett.* **2002**, *2*, 351.
[14] T. R. Jensen, M. D. Malinsky, C. L. Haynes, R. P. Van Duyne, *J. Phys. Chem. B* **2000**, *104*, 10549.
[15] F. Mafune, J. Kohno, Y. Takeda, T. Kondow, H. Sawabe, *J. Phys. Chem. B* **2000**, *104*, 8333.
[16] J. P. Abid, W. W. Wark, P. F. Brevet, H. H. Girault, *Chem. Commun.* **2002**, *7*.
[17] H. H. Huang, X. P. Ni, G. L. Loy, C. H. Chew, K. L. Tan, F. C. Loh, J. F. Deng, G. Q. Xu, *Langmuir* **1996**, *12*, 909.
[18] J. J. Zhu, S. W. Liu, O. Palchik, Y. Koltypin, A. Gedanken, *Langmuir* **2000**, *16*, 6396.
[19] N. A. Kotov, M. E. D. Zaniquelli, F. C. Meldrum, J. H. Fendler, *Langmuir* **1993**, *9*, 3710.
[20] ICI, *Personal communication*.
[21] T. C. W. Mak, G. Zhou, *Crystallography in Modern Chemistry*, John Wiley and Sons, New York, **1992**.
[22] M. Green, P. O'Brien, *Chem. Commun.* **1999**, 2235.
[23] X. Peng, *Chem. Eur. J.* **2002**, *8*, 334.
[24] N. Chestnoy, T. D. Harris, R. Hull, L. E. Brus, *J. Phys. Chem.* **1986**, *90*, 3393.
[25] T. Abe, Y. Tachibana, T. Uematsu, M. Iwamoto, *J. Chem. Soc.-Chem. Commun.* **1995**, 1617.
[26] M. P. Pileni, L. Motte, C. Petit, *Chem. Mat.* **1992**, *4*, 338.
[27] B. O. Dabbousi, J. RodriguezViejo, F. V. Mikulec, J. R. Heine, H. Mattoussi, R. Ober, K. F. Jensen, M. G. Bawendi, *J. Phys. Chem. B* **1997**, *101*, 9463.
[28] Q. L. Nie, Q. L. Yuan, Z. D. Xu, *J. Inorg. Mater.* **2004**, *19*, 1411.
[29] G. Q. Xu, B. Liu, S. J. Xu, C. H. Chew, S. J. Chua, L. M. Gana, *J. Phys. Chem. Solids* **2000**, *61*, 829.

[30] Y. F. Liu, J. H. Zhan, M. Ren, K. B. Tang, W. C. Yu, Y. T. Qian, *Mater. Res. Bull.* **2001**, *36*, 1231.
[31] S. H. Yu, J. Yang, Z. H. Han, Y. Zhou, R. Y. Yang, Y. T. Qian, Y. H. Zhang, *J. Mater. Chem.* **1999**, *9*, 1283.

# Chapter 8: Final conclusions

## *Introduction*

In retrospect, the focus of this Thesis was significantly different from that which was initially intended. The number of engineering problems that needed to be overcome for the successful performance of experiments was greater than anticipated. This transformed the whole project into an interdisciplinary chemistry-engineering collaboration.

As the only chemist on the project, my role was, in essence, to make the chemistry work. Most of the runs were carried out by me, but during the development stages, my engineering colleagues ran experiments, normally to my specifications. Whilst using the rig, I made changes to the engineers' overall rig design to make it more practical to run: these included the addition of a cooling coil upstream of the reactor to prevent oxide precipitation before the streams reached the mixing point, redesigning the pipework downstream of the reactor to avoid horizontal surfaces, and thus prevent particles being deposited on the interior of the pipes, and so on.

Ideally, the project would have reached its current state at an earlier stage. Happily, we are now in the situation where:-

1. The equipment now works reliably without blockages

2. When the same conditions are chosen for several experiments, the rig produces the same product reproducibly (surface-area measurements for $CeO_2$ particles vary by only ± 5% - see Chapter 5).

3. Temperatures up to 300°C are attainable on Rig 2 and over 400°C on Rig 3 – considerably higher than those that were possible before – and the temperature remains constant throughout experiments. This had been a particular problem with the work on copper oxide in Chapter 3, where the reaction temperature fluctuated to such an extent that to draw even the most tentative of conclusions was almost impossible.

4. A range of strategies for the separation of particles from the raw reactor product is now available (see Chapter 5).

5. The advantages and suitability of the various characterisation techniques available for the products are much clearer, and PXD has proven to be the quickest and simplest routine technique for determining the particle-size and crystalline phases present. TEM is also useful for assessment of particle-size distributions.

The major task now is to establish how far particle size and particle properties can be tuned via the reaction parameters. The factors of nucleation, precursor diffusion and agglomeration, which affect particle size, are themselves affected by temperature, reaction time and reactor concentration, as was discussed in Chapter 1. The experimental work in this Thesis confirms that particle size is increased when the reaction temperature is increased. It will now be possible to test the effect of the remaining reaction parameters systematically.

## *Conclusions and future work arising from the work in this Thesis*

The hydrothermal flow synthesis technique has proved effective for the rapid formation of several different metal oxides: CuO, $RuO_2$, $TiO_2$ (anatase) $CeO_2$, $ZrO_2$ and $Fe_2O_3$. These can all be formed from their salts, using only high-pressure, high-temperature water, without additional additives such as base or hydrogen peroxide.

In the work on copper oxide (Chapter 3), the use of different precursors was observed to lead to the formation of particles with different sizes. However, further work was hampered by the problems with blockages. Now that a reactor that does not suffer from such problems has been built, it would be useful to find how to achieve some form of continuous control over particle size. It is not yet known why the use of different precursors has an effect upon particle size but it may be due to differences in pH. Experiments to ascertain the effect of pH could therefore yield interesting results.

In the work on titania and ruthenia (Chapter 4), a method for making rutile-phase titania or ruthenia-titania mixed oxide using the hydrothermal flow apparatus was not found. Anatase $TiO_2$ is known to change to rutile $TiO_2$ at high temperatures, so if a rig could be built that went up to much higher temperatures than the current designs, formation of rutile nanoparticles might become possible. Only a fairly small range of titanium and ruthenium precursors was tried. If two reagents with similar stability to hydrothermal decomposition of ruthenium and titanium precursors could be found, it might become possible to form a single-phase ruthenia-titania compound.

Experiments on $Ce_xZr_{1-x}O_2$ (in Chapter 5) have shown the potential for single-step formation of single-phase mixed-oxide compounds. Attempts to make $Ru_xTi_{1-x}O_2$ were unsuccessful, but there are likely to be other combinations of metals that *are* possible to make by this technique, and the technique allows for quick testing of different reagents.

Following on from ceria and ceria-zirconia work, having established that rising temperature does have an effect upon particle size, it would be interesting to be able to investigate what happens at supercritical conditions, and whether there is a sharp change in particle properties at the critical point. At supercritical conditions, there might also be an effect of pressure upon particle size, as the fluid becomes more compressible. Whilst an effect of reactant concentration upon particle size was predicted, no such effect was observed over the range of concentrations tested. It would be interesting to test a much wider range to see whether the prediction, that lower concentrations of precursor lead to larger particles, is correct. Finally, whilst the method of adding acid to the product suspension is very useful for purification of the product, it could be very environmentally damaging, if this process were to be used on a larger scale. Alternative means of causing the suspension to settle, perhaps by using salts instead of acid to increase the ionic concentration of the mixture, might be effective and less harmful.

The iron oxide particles that were made in Chapter 6 have become part of interesting research, performed by Nottingham materials scientists, on the growth of graphitic nanofibres. This showed how different iron-oxide catalyst morphologies led to significantly different forms of fibre growth.

The investigations on the formation of iron oxide never led to a method for making $\gamma$-$Fe_2O_3$. However, it is possible, by degassing the water used in the reaction[1], to form the less-oxidised compound, $Fe_3O_4$ which, it is said[2], can be oxidised to $\gamma$-$Fe_2O_3$, as both possess similar crystal structures. Perhaps a way could be found to make $\gamma$-$Fe_2O_3$ nanoparticles, with reduction occurring either within the flow reactor or in a separate stage afterwards.

In addition to metal oxides, this research has gone a small way to showing that other compounds can be made by this technique. In Chapter 7, using formic acid to produce a reducing species in situ as it decomposes, it was possible to reduce $Ag^+$ to form silver nanoparticles. Whilst this feat turned out to be difficult to repeat, it does show promise for the future.

Further experiments with silver, using different conditions, were not performed. Testing the effect of temperature upon particle size would be interesting as well as potentially useful, as different chemistry is occurring from that used in the ceria and iron oxide work.

The hydrothermal flow synthesis has also been shown, in this Thesis, to have potential for the formation of chalcogenides other than oxygen. Cadmium sulfide was formed using a cadmium salt and a soluble organic sulfur compound but characterisation, and further experiments, were made difficult owing to the high toxicity of the reagents, particularly thiocarbohydrazide. Thiourea could be an effective substitute for thiocarbohydrazide and would be significantly less hazardous. Yellow particles were observed to be formed, with sizes of 100-200 nm. Continuing work in Chemistry and Chemical Engineering at Nottingham has further adapted the reactor design in order to

continue work on cadmium sulfide, by adding an inlet downstream of the mixing point to allow the addition of capping agents to the hot reaction mixture. This may provide better control of particle size than adjusting other reaction variables alone.

It might also be possible to form another semiconductor, cadmium selenide, by reacting a cadmium salt with selenourea, the selenium analogue of thiourea. It would then be possible to experiment with higher reaction temperatures to see whether these had an effect on particle size; as with silver, the chemistry differs from that in the oxide-formation reactions and particle size might be affected differently.

## *New compounds for synthesis*

Whilst the substances that have been synthesised in this Thesis are not new compounds, this does not mean that they are necessarily not new materials. In the field of Materials Chemistry, the chemical formula of a material goes only part of the way towards describing it. Materials with the same chemical formula, but formed by different routes, may possess very different properties.

As an example, we can observe the iron oxide particles that were formed at different temperatures in Chapter 6. The particles formed at high temperatures were rust-red and settled from suspension, whilst those formed at low temperatures remained in a deep-red suspension. Whilst, according to PXD results, both samples consisted of particles of $Fe_2O_3$, TEM revealed that those formed at higher temperatures were much more crystalline and had significantly larger particle size than those made at lower temperatures. Moreover, when the iron oxide particles were used as a catalyst for the

formation of graphitic nanofibres, very different morphologies of nanofibres were observed to have formed.

Several oxides containing a single metal have been made in this Thesis. However, the potential for making mixed-metal oxides has not been fully exploited. These compounds would represent a rich seam of potential future research and there follow some examples of such compounds and their uses.

Doping with zirconium[1] is not the only way to stabilise ceria: other metals can also be used, and could possibly be made using the flow reactor by a similar method, including copper[3] and terbium[4].

Titanium-silicon and titanium-tungsten mixed-oxide compounds can be more effective photocatalysts than titania alone, as they are less likely to agglomerate during use[5, 6]. These might be made using the hydrothermal flow reactor using water-soluble titanium, tungsten and silicon compounds. Soluble titanium compounds are easy to find (e.g. titanium oxynitrate), but it might be rather more difficult to identify suitable water-soluble tungsten and silicon compounds. It might be possible to use tungstates and silicates, perhaps even starting with titanium tungstate or silicate.

Aluminium-magnesium mixed-oxide compounds are useful as catalysts, catalytic supports and adsorbents[7]. As was established by Adschiri et al.[8], aluminium compounds generally form AlOOH and not $Al_2O_3$ in the hydrothermal flow reactor. Therefore a method to make the oxide, as opposed to the oxy-hydroxide would need to be formulated, possibly involving the addition of hydrogen peroxide to the water feed.

Certain mixed-oxide spinel compounds can be used as catalysts, cathode materials and heat-resistant pigments[9], including $CoAl_2O_4$, $CoCr_2O_4$, and $CuCr_2O_4$. It should be possible to make these in a similar way to the metal ferrites and magnetite that were made in the flow reactor before[1]. The degassing of the water and metal-salt feedstocks would be likely to be necessary to prevent the formation of $Co^{3+}$ and $Cu^{3+}$.

As can be seen from this selection, mixed-oxide compounds are many and varied, and will provide many opportunities for future research.

The versatility of hydrothermal flow syntheses means that they have every chance of becoming a well-established, less-polluting, more-efficient synthesis technique for inorganic nanoparticles.

## *References*


[1] A. Cabañas, M. Poliakoff, *J. Mater. Chem.* **2001**, *11*, 1408.

[2] N. N. Greenwood, A. Earnshaw, *Chemistry of the Elements*, 1st ed., Butterworth-Heinemann, Oxford, **1984**.

[3] X. Q. Wang, J. A. Rodriguez, J. C. Hanson, D. Gamarra, A. Martinez-Arias, M. Fernandez-Garcia, *J. Phys. Chem. B* **2005**, *109*, 19595.

[4] X. Q. Wang, J. C. Hanson, G. Liu, J. A. Rodriguez, A. Iglesias-Juez, M. Fernandez-Garcia, *J. Chem. Phys.* **2004**, *121*, 5434.

[5] X. Zhang, F. Zhang, K. Y. Chan, *Appl. Catal. A-Gen.* **2005**, *284*, 193.

[6] M. Fernandez-Garcia, A. Martinez-Arias, A. Fuerte, J. C. Conesa, *J. Phys. Chem. B* **2005**, *109*, 6075.

[7] C. L. Carnes, P. N. Kapoor, K. J. Klabunde, J. Bonevich, *Chem. Mat.* **2002**, *14*, 2922.

[8] T. Adschiri, K. Kanazawa, K. Arai, *J. Am. Ceram. Soc.* **1992**, *75*, 2615.

[9] H. T. Cui, M. Zayat, D. Levy, *J. Sol-Gel Sci. Technol.* **2005**, *35*, 175.